

SURFACE MORPHOLOGY DYNAMICS IN STRAINED-LAYER EPITAXY

by

THOMAS HENRY PINNINGTON

B. Sc. (Engineering Physics) University of Alberta, Edmonton, 1990

M. A. Sc. University of British Columbia, Vancouver, 1992

A THESIS SUBMITTED IN PARTIAL FULFILLMENT OF

THE REQUIREMENTS FOR THE DEGREE OF

DOCTOR OF PHILOSOPHY

in

THE FACULTY OF GRADUATE STUDIES

Department of Physics and Astronomy

We accept this thesis as conforming

to the required standard

THE UNIVERSITY OF BRITISH COLUMBIA

December 1999

© Thomas Henry Pinnington, 1999

In presenting this thesis in partial fulfilment of the requirements for an advanced degree at the University of British Columbia, I agree that the Library shall make it freely available for reference and study. I further agree that permission for extensive copying of this thesis for scholarly purposes may be granted by the head of my department or by his or her representatives. It is understood that copying or publication of this thesis for financial gain shall not be allowed without my written permission.

Department of Physics and Astronomy

The University of British Columbia
Vancouver, Canada

Date 20/12/99

Abstract

The surface of a film grown epitaxially on a crystalline substrate is generally rough, even if the initial growth surface is smooth on the atomic scale. In the case of strained-layer epitaxy, in which the composition of the film is such that it does not share the same lattice constant as the substrate, the roughness often develops in response to strain-relief processes occurring in the film during growth. In this thesis we show that a careful analysis of the time evolution of the surface morphology during strained-layer growth, can reveal quantitative information about both the strain-relief mechanisms acting within the film and the diffusion processes occurring at the surface.

Two complementary measurement techniques, namely atomic force microscopy (AFM) and elastic light scattering, are used to acquire the surface morphology information necessary for the analysis. In this work we demonstrate quantitative agreement between roughness measurements obtained by both techniques. A major advantage of light scattering over AFM is its suitability to real-time monitoring of the surface during growth.

We consider the growth of $\text{In}_{0.18}\text{Ga}_{0.82}\text{As}$ and InAs , on (001)-oriented GaAs substrates, by molecular beam epitaxy (MBE). In both cases the film is compressively strained owing to the 7% lattice mismatch between InAs and GaAs . In the case of $\text{In}_{0.18}\text{Ga}_{0.82}\text{As}$ growth, the strain is relieved plastically as the film thickness increases, through the introduction

of misfit dislocations at the film/substrate interface. A characteristic crosshatch pattern develops at the surface, consisting of ridges aligned along the $\langle 110 \rangle$ crystal directions. We present an analytical model to describe this roughening, in which the ridges arise from surface diffusion in response to the dislocation strain fields. Although it has only three fitting parameters, the model is able to reproduce both the time dependence and the length scale dependence of the surface morphology, as measured by light scattering and AFM.

For the case of InAs growth on GaAs, the strain is relieved elastically through a morphological transition in which nearly identically-sized three-dimensional islands form, known in the literature as quantum dots. For typical growth conditions the islands are too small and closely spaced to be detected using visible wavelengths. An ultraviolet light scattering apparatus is described, which we show can detect the onset of quantum dot formation. The UV scattering signal increases linearly with time after the dots have formed, which we interpret as evidence that the dots are diffusing on the surface. During prolonged annealing we observe the emergence and growth of larger islands that initially consume material from the quantum dots and then compete with each other for material. The *in situ* light scattering measurements reveal that these processes are sensitively dependent on annealing temperature and arsenic overpressure.

Table of Contents

Abstract	ii
List of Tables	viii
List of Figures	xix
Acknowledgements	xx
1 Introduction	1
2 Surface Roughness Measurement	8
2.1 The Power Spectral Density Function	8
2.2 Measuring the PSD	10
2.2.1 Atomic Force Microscopy	10
2.2.2 Elastic Light Scattering	14
2.2.3 One-Dimensional Roughness	17
2.3 Comparison of Light Scattering and AFM	19
2.3.1 Sample Preparation	19
2.3.2 Measurement Technique	21

2.3.3	Isotropic 2D Roughness: Oxide-Desorbed GaAs	23
2.3.4	Anisotropic 2D Roughness: GaAs Buffer Layer	27
2.3.5	1D Roughness: InGaAs on GaAs	31
2.3.6	High Aspect Ratio Roughness: Quantum Dots	36
3	Real-Time Light Scattering Setup	48
3.1	Optical Port Configurations and Detection Technique	48
3.2	Visible Light Scattering	53
3.3	Ultra-Violet Light Scattering	55
3.3.1	Light Source	55
3.3.2	Detectors and Viewports	59
3.3.3	Alignment and Calibration	62
4	Misfit Dislocations and Surface Crosshatch	65
4.1	Strain Relaxation in InGaAs on GaAs	66
4.1.1	Misfit Dislocations	66
4.1.2	Critical Thickness for Dislocation Formation	69
4.1.3	Strain Field from Dislocations	71
4.1.4	Strain and Surface Energy	74
4.2	Continuum Equation for Strained-Layer Growth	76
4.3	Measurement of Surface Crosshatch	82
4.3.1	Sample Growth and Light Scattering	82

4.3.2	Analysis of Light Scattering Data	83
4.4	Comparison of Model and Experiment	86
4.4.1	Time Dependence	86
4.4.2	Spatial-Frequency Dependence	90
4.5	Effect of Growth Conditions on Surface Crosshatch	93
4.5.1	Effect of Crystallographic Anisotropy	94
4.5.2	Effect of Growth Temperature and Lattice Mismatch	98
4.6	Summary	103
5	Coherent Islanding, Quantum Dots, and Ostwald Ripening	105
5.1	Stranski-Krastanow Growth in the InAs/GaAs System	107
5.2	Real-Time Monitoring Experiments	109
5.2.1	Substrate Preparation	109
5.2.2	Quantum Dot Growth	112
5.3	Results	115
5.3.1	Light Scattering	116
5.3.2	AFM	118
5.3.3	Analysis of Light Scattering Data	121
5.4	Discussion	126
5.4.1	Dot Diffusion	128
5.4.2	Island Growth and Ripening	134
5.5	Effect of Growth Conditions on Island Growth	136

5.5.1	Effect of Annealing Temperature	139
5.5.2	Effect of Arsenic Pressure and Indium Coverage	140
5.5.3	Effect of Surface Strain Fields	142
5.6	Summary	144
6	Conclusions	146
	Bibliography	149
A	The Polarization Factor	157

List of Tables

3.1	Spatial frequencies probed at each detector port, for visible and ultraviolet light scattering measurements.	50
3.2	Acceptance angles for detector ports used in visible and ultraviolet light scattering experiments.	54
3.3	Optical path length d from each optical element to the lamp as shown in Fig. 3.2. Also specified are the lens focal lengths f , and the effective diameter D and optical throughput of each element.	57
4.1	Parameter values used for the fits in Figures 4.5, 4.7 and 4.8.	88
4.2	Measured relaxation compared with a $1/z$ law, using critical thicknesses of 52 nm and 55 nm for the $[1\bar{1}0]$ and $[110]$ directions respectively.	90
4.3	Model parameter values and experimental peak intensities at $16 \mu\text{m}^{-1}$ for InGaAs growths at different temperatures. Peak intensities in parentheses obtained at $10.5 \mu\text{m}^{-1}$	99
A.1	Components of Q for unpolarized 250-nm light incident at $\theta_i = 55^\circ$, for the two spatial frequencies, q , accessible in the <i>in situ</i> measurement. . . .	159

List of Figures

- 1.1 Strain relief in heteroepitaxial film growth. (a) Cross-sectional view of a compressively strained epilayer. Also shown are the equilibrium lattice constants, a_e and a_s of the epilayer and the substrate respectively. (b) Misfit dislocation located at the substrate/epilayer interface. The dislocation shown is an edge dislocation. The core of the dislocation is indicated by the circle and extends along a line perpendicular to the page. Note that the strain field varies with position along the surface. (c) Cross-section of an elastically-deformed coherent island. Most of the strain relief occurs at the edges and at the top of the island. 3
- 1.2 Atomic force microscope (AFM) images of the surfaces of strain-relaxed films. (a) 200 nm-thick film of $\text{In}_{0.2}\text{Ga}_{0.8}\text{As}$, for which the equilibrium lattice constant is $\sim 1.4\%$ larger than that of the GaAs substrate. The ridges are aligned along $\langle 110 \rangle$ crystal directions, and arise from the dislocation array which develops to relieve the epilayer strain. (b) Coherent islands (quantum dots) resulting from the deposition of 3 monolayers of InAs on a GaAs substrate. The equilibrium lattice mismatch is 7% 4

2.1	(a) $5 \times 5 \mu\text{m}^2$ AFM image of a GaAs film, showing atomically flat terraces (step height between terraces = 0.28 nm). (b) Corrected representation of the surface as discussed in the text.	12
2.2	Comparison of the isotropic 2D power spectrum calculated from the AFM image in Fig. 2.1(a), and from the corrected image in Fig. 2.1(b). Lines of slope -2 and -3 are shown for reference.	13
2.3	Scattering angles for the case where the plane of incidence is aligned with the x -direction. The specular beam is also shown.	14
2.4	(a) AFM image and (b) two-dimensional power spectrum of a GaAs substrate from which the oxide has been thermally desorbed. The gray scale bar in (a) corresponds to a vertical range of 50 nm. In (b) a logarithmic gray scale is used, which spans 3 decades.	25
2.5	Comparison of light scattering and AFM measurements of the isotropic 2D PSD, for the oxide-desorbed surface in Fig. 2.4.	26
2.6	(a) AFM image (gray scale = 10 nm) and (b) 2D PSD (logarithmic gray scale) of a $1 \mu\text{m}$ thick GaAs buffer layer grown on a substrate from which the oxide has been removed thermally.	29
2.7	Light scattering and AFM measurements of the 2D PSD along the two orthogonal $\langle 110 \rangle$ directions, for the GaAs buffer layer in Fig. 2.6. A line of slope -2 is shown for reference.	30

2.8	AFM image (5 nm vertical gray scale range) and PSD (logarithmic gray scale) before and after distortion correction. The sample consists of a 250 nm thick layer of $\text{In}_{0.18}\text{Ga}_{0.82}\text{As}$ grown on a 1 μm thick GaAs buffer layer.	32
2.9	Light scattering and AFM measurements of the 1D PSD along the $[1\bar{1}0]$ crystal direction, for the relaxed InGaAs film in Fig. 2.8.	34
2.10	(a) $2 \times 2 \mu\text{m}^2$ AFM image of a bare GaAs buffer layer and (b) $1 \times 1 \mu\text{m}^2$ AFM image of a buffer layer on which 3 ML of InAs was deposited and annealed for 2 minutes at 490°C. The gray scale bars in (a) and (b) correspond to a vertical range of 4 nm and 30 nm respectively.	37
2.11	$2 \times 2 \mu\text{m}^2$ AFM image of the film in Fig. 2.10(b), showing the quantum dots and the large islands. The image has been digitally filtered to appear as if illuminated from the right.	38
2.12	(a) Quantum dot height distribution and (b) inferred aspect ratio of the dots based on simulated AFM profiles as shown in Fig. 2.14.	39

2.13	Estimation of the 2D PSD for the film in Fig. 2.11, based on post-growth AFM. (a) Gray diamonds, PSD computed directly from a $10 \times 10 \mu\text{m}^2$ image of the film. (b) Gray circles, PSD of the bare buffer layer in Fig. 2.10(a). The solid line has a slope of -3. (c) Open circles, PSD for a simulated QD distribution, in which each dot in Fig. 2.10(b) was replaced with a cone as discussed in the text. (d) Open diamonds, PSD of the large island distribution obtained by replacing the 37 large islands in the image used to compute curve <i>a</i> with 1:2 aspect ratio cones. (e) Solid black circles, corrected version of the PSD in (a), obtained by adding curves (b), (c) and (d). The three open squares are an independent estimate of the PSD based on <i>in situ</i> light scattering measurements.	41
2.14	Comparison of three simulated AFM scan profiles (solid line) with actual AFM measurements from Fig. 2.10 (open circles), for two QDs having heights of (a) 5.8 nm, (b) 10.3 nm, and one large island of height 24.6 nm (c).	43
3.1	(a) Plan view of MBE growth flange showing optical port configuration, and (b) cross-sectional view in the plane of incidence showing detection geometry for the ultra-violet light scattering measurements.	49
3.2	Schematic of UV light source. The lens focal lengths and distance of each optical element from the arc lamp is shown in Table 3.3.	56
3.3	Schematic of detector arrangement at port <i>G</i>	60

4.1	(a) 60° misfit dislocation aligned along the $[1\bar{1}0]$ direction, showing orientation of the Burgers vector \vec{b} which lies in the (111) slip plane. $\lambda = \beta = 60^\circ$. (b) The same dislocation at the (001) interface plane. Slip in the (111) plane associated with the dislocation produces an atomic-height step at the surface.	67
4.2	(a) Schematic plan view of the (001) interface between a strain-relaxed InGaAs film and a GaAs substrate, showing the $\langle 110 \rangle$ -oriented dislocation lines. (b) Cross section along the $[1\bar{1}0]$ direction showing the interfacial dislocations and the associated slip planes.	68
4.3	Strain field due to a single misfit dislocation located at the origin, for increasing film thickness.	73
4.4	(a) $20 \times 20 \mu\text{m}^2$ AFM image of a 250 nm thick InGaAs film, with a 10 nm vertical gray scale and (b) power spectrum calculated from a $100 \times 100 \mu\text{m}^2$ image of the same film, where the gray scale represents the logarithm of the PSD at each spatial frequency, q . The axes for the PSD are oriented approximately along $\langle 100 \rangle$ directions and span a q range of $\pm 16 \mu\text{m}^{-1}$ ($q = 0$ at origin). The 4 crosses in (b) indicate the spatial frequencies monitored by <i>in situ</i> light scattering.	84

4.5	<i>In situ</i> light scattering measurements (thick lines) of surface roughness at $q = 5.4$ and $10.5 \mu\text{m}^{-1}$ during growth of an $\text{In}_{0.18}\text{Ga}_{0.82}\text{As}$ film at 490°C , and calculated time evolution of the 1D PSD (thin lines) using different combinations of ν and K	87
4.6	<i>Ex situ</i> light scattering data (symbols) and model data (solid and dashed lines) for the 1D PSD along $[1\bar{1}0]$ of three InGaAs films with different thicknesses above the critical thickness.	91
4.7	Light scattering data (thick lines) obtained along the $[110]$ direction during the same InGaAs growth experiment as in Fig. 4.5, and simulation results (thin lines) using $\nu = 1.1 \times 10^{-13} \text{ cm}^2/\text{s}$	95
4.8	Simulations of the roughening along the $[1\bar{1}0]$ direction (a) and the $[110]$ direction (b), obtained using empirical fits to the anisotropic strain relaxation data from X-ray measurements.	96
4.9	Light scattering signal at $16 \mu\text{m}^{-1}$ (thick lines) and simulation (thin lines) for $\text{In}_{0.18}\text{Ga}_{0.82}\text{As}$ growth at different temperatures. Curves <i>a</i> (515°C) and <i>c</i> (452°C) are taken along the $[110]$ direction and curve <i>b</i> (430°C) is along $[1\bar{1}0]$	99
4.10	Scattered light intensity measured along $[1\bar{1}0]$ at $q = 16 \mu\text{m}^{-1}$ during $\text{In}_x\text{Ga}_{1-x}\text{As}$ growth with three different In concentrations as indicated.	101
4.11	Simulated time evolution of the PSD calculated using $\nu = 0.6 \times 10^{-12} \text{ cm}^2/\text{s}$ and three different values of the critical thickness as indicated.	101

5.1	Light scattering signals at 16, 31 and 41 μm^{-1} , monitored simultaneously during thermal oxide desorption and GaAs buffer layer growth, both performed at 600 °C. The buffer layer growth begins and ends at the times indicated by the arrows marked “o” and “x” respectively.	110
5.2	Light scattering signals acquired during 4 separate InAs quantum dot growth experiments, during the same run and sharing the same time-axis as Fig. 5.1. The downward-pointing arrows (<i>a, b, c</i> and <i>d</i>) indicate the times at which 3 ML of InAs was deposited, at different substrate temperatures as discussed in the text. The InAs was evaporated between experiments, at the times indicated by the upward-pointing arrows.	113
5.3	Time evolution of the light scattering signals during a quantum dot growth at 490 °C, corresponding to the AFM image in Fig. 2.11. The indium deposition was terminated at $t = 0$, and the film was quenched at $t = 2$ minutes (indicated by dashed line in the figure). Each scattering signal is normalized to unity at $t = 0$	116
5.4	Light scattering signals (normalized to the initial scattering) corresponding the experiment in Fig. 5.2 (arrow <i>c</i>) in which the dots were grown and annealed at 400 °C	117

5.5	AFM images ($2 \times 2 \mu\text{m}^2$) showing the effect of annealing time on the island distribution. In both cases 3 ML of InAs were deposited at 440°C . (a) Quantum dot distribution after a 3 min anneal at 440°C (30 nm gray scale). (b) Image taken after a 25 min anneal at the same temperature, showing QDs and two large islands. The gray scale range in (b) has been reduced to 10 nm in order to reveal the underlying surface steps, so that the islands appear saturated white.	119
5.6	Large scale ($20 \times 20 \mu\text{m}^2$) AFM image of the film in Fig. 5.5(b), showing the spatial distribution of the QDs, the large islands, and the background texture of the buffer layer. The image is filtered to appear illuminated from the left. The $[1\bar{1}0]$ direction is oriented as in Fig. 5.5(b).	120
5.7	Comparison of the q -dependence of the scattering data in Fig. 5.4 for the 400°C growth and annealing experiment, and a similar experiment performed during the same MBE run at 280°C . The initial background scattering has been subtracted from the signals, which are normalized to coincide at the end of the anneal. The PSD has been calculated from the scattered light intensity based on an absolute calibration of the $41 \mu\text{m}^{-1}$ signal as discussed in the text.	123

- 5.8 Collapse of the two data sets in Fig. 5.7, obtained by rescaling the time axis for each temperature. The times, t^* used to obtain the data collapse were 0.2 min and 1 min respectively for the films annealed at 400 °C and 280 °C. The three linear regions, which correspond to regions of distinct power-law behavior, have slopes of (a) 0.9, (b) 2.0, and (c) 0.75. 126
- 5.9 Evolution of the quantum dots and large islands during annealing. (a) Quantum dots nucleate on the surface. (b) The QDs diffuse randomly as they exchange atoms with the adatom population. (c) Quantum dots collide, nucleating larger defective islands. (d) The larger islands act as a sink for the constant supply of adatoms provided by the QDs. (e) The QD population is depleted. (f) The islands compete with each other for the remaining supply of adatoms, which diminishes with time as the average island size increases (Ostwald ripening). 127
- 5.10 Time-evolution of the PSD at $41 \mu\text{m}^{-1}$ during the early stages of QD growth. Gray circles: PSD calculated from the $41 \mu\text{m}^{-1}$ signal in Fig. 5.3 after subtracting the background, plotted on a log-log scale. The time t_0 is 0.2 minutes. Black circles: Simulation of the PSD, in which the QDs nucleate on a 58 nm pitch square grid and then diffuse on the surface during annealing as discussed in the text. The solid line has a slope of 1. 129

5.11	Temperature dependence of the PSD during annealing. InAs deposition begins at $t = 0$. For each curve, the annealing temperature and time, t_o (discussed in the text), are: (a) 410° C, 1.2 min, (b) 360° C, 1.5 min, (c) 300° C, 5 min, (d) 260° C, 11 min, (e) 280° C, 1 min, and (f) 400° C, 0.2 min. Curves e and f are taken from Fig. 5.7.	137
5.12	Data collapse of the six curves in Fig. 5.11, achieved by rescaling the annealing time in each case by a characteristic time t^* . Regions I, II, and III are fitted with lines of slope 1, 2, and $3/4$ respectively. Inset: Temperature dependence of t^* for curves $a - d$ (black circles and solid line fit) and curves e and f (gray circles).	138
5.13	Effect of arsenic flux on island growth during annealing at 450° C. Linear fits have been made to the data before and after the switch in arsenic flux at $t = 13$ min.	140
5.14	Effect of indium coverage on island growth during annealing at 450° C. .	141
5.15	AFM images of dots grown on strain-relaxed InGaAs films. (a) 6 ML of InAs deposited on a 170 nm thick InGaAs film ($2.5 \times 2.5 \mu\text{m}^2$). (b) 4 ML of InP grown on a 250 nm thick InGaAs layer ($4 \times 4 \mu\text{m}^2$). The gray scale bar corresponds to 150 nm and 50 nm for (a) and (b) respectively.	143

A.1	Polarization factor Q corresponding to two different scattering set-ups, for which $\phi_s = 0$. Dotted curve: Q_{ss} for the case of 632-nm light incident at $\theta_i = 65^\circ$. Solid curves: Q_{ss} and Q_{pp} for 250-nm light incident at 55° . The arrow indicates the angular range used in the <i>ex situ</i> light scattering measurement.	159
-----	--	-----

Acknowledgements

It is a pleasure to acknowledge my supervisor Tom Tiedje, whose infectious optimism has propelled me to the completion of this work, not to mention to the summits of numerous mountains in the Lower Mainland.

I am indebted to Christian Lavoie for the experimental light-scattering data appearing in Chapters 2 and 4. I also wish to thank my other co-workers and collaborators: Jim Mackenzie, Shane Johnson, Steve Patitsas, Mario Beaudoin, Yuval Levy, Martin Adamcyk, Karen Kavanagh, Jeff Hutter, George Soerensen, Anders Ballestad, Christine Nicoll, Diane Goodman, Al Schmalz, Ben Ruck, Jens Schmid, Sebastien Tixier, and the technicians in the electronics shop, machine shop, and shared technical services.

Finally I thank NSERC and the Science Council of BC for their generous financial support.

Chapter 1

Introduction

The problem of why surface roughness develops during thin film growth has been a topic of intense interest in recent years. From a technological standpoint, the issue is important because the interface roughness between active layers in semiconductor heterostructures for example, derives from the surface roughness of epitaxial thin films during growth. Interface roughness can limit the mobility of electrons in field effect transistors, scatter light in optical waveguides and broaden the gain spectrum of quantum well lasers [1, 2, 3]. On a more fundamental level, the study of thin film surface roughness in the continuum limit (lateral length scales much greater than an atomic spacing) provides insight into the underlying atomic-scale growth processes [4].

The starting point of a description of film growth is the case of homoepitaxy, where the composition of the film and the substrate is the same. The surface roughening in this case is driven by random fluctuations in the deposition flux across the film, through a process known as kinetic roughening. Various continuum growth equations and computer simulations have been used to model this process [4, 5, 6]. A general result is that

the surface morphology is self-affine, meaning that the RMS surface roughness scales with surface area according to a power law. Such scaling relations are also observed experimentally in the growth of metal [7] and semiconductor [8] films, however the precise form of the equation that describes growth in any particular system has not yet been established.

Heteroepitaxial growth has also been studied both theoretically [9, 10, 11] and experimentally [12-22] in particular for the case where the deposited film has a larger equilibrium lattice constant than the substrate material. The situation is illustrated in Figure 1.1. For small film thicknesses, the film is compressively strained to accommodate the lattice mismatch while maintaining coherency with the substrate lattice [Fig. 1.1(a)]. Once the growth proceeds beyond a critical film thickness however, structural changes occur in the film to relieve the strain. These structural changes can occur either plastically, through the introduction of dislocations [Fig. 1.1(b)], or elastically, through a coherent transformation of the film geometry in which the crystalline integrity of the film is preserved [Fig. 1.1(c)]. In either case it is the strain-relief process itself that drives the surface roughening. As shown in Figure 1.2, distinct features appear in the surface morphology, which are particular to the strain relief process acting within the film. If the strain relief is achieved through the introduction of dislocations at the film/substrate interface for example, an array of one-dimensional surface ridges often develops, in response to the one-dimensional interfacial dislocation array. This is observed for example in InGaAs/GaAs [14, 15, 23] and SiGe/Si [12, 13] growth on (001)-oriented substrates,

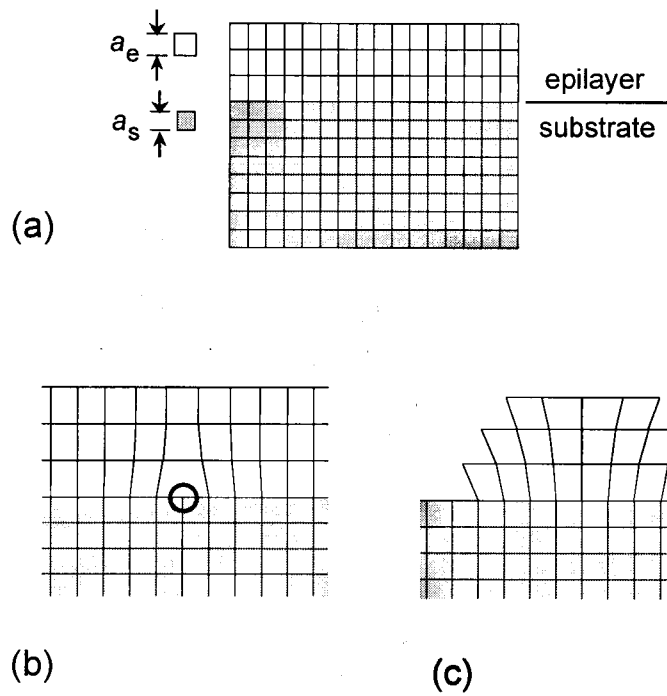


Figure 1.1: Strain relief in heteroepitaxial film growth. (a) Cross-sectional view of a compressively strained epilayer. Also shown are the equilibrium lattice constants, a_e and a_s of the epilayer and the substrate respectively. (b) Misfit dislocation located at the substrate/epilayer interface. The dislocation shown is an edge dislocation. The core of the dislocation is indicated by the circle and extends along a line perpendicular to the page. Note that the strain field varies with position along the surface. (c) Cross-section of an elastically-deformed coherent island. Most of the strain relief occurs at the edges and at the top of the island.

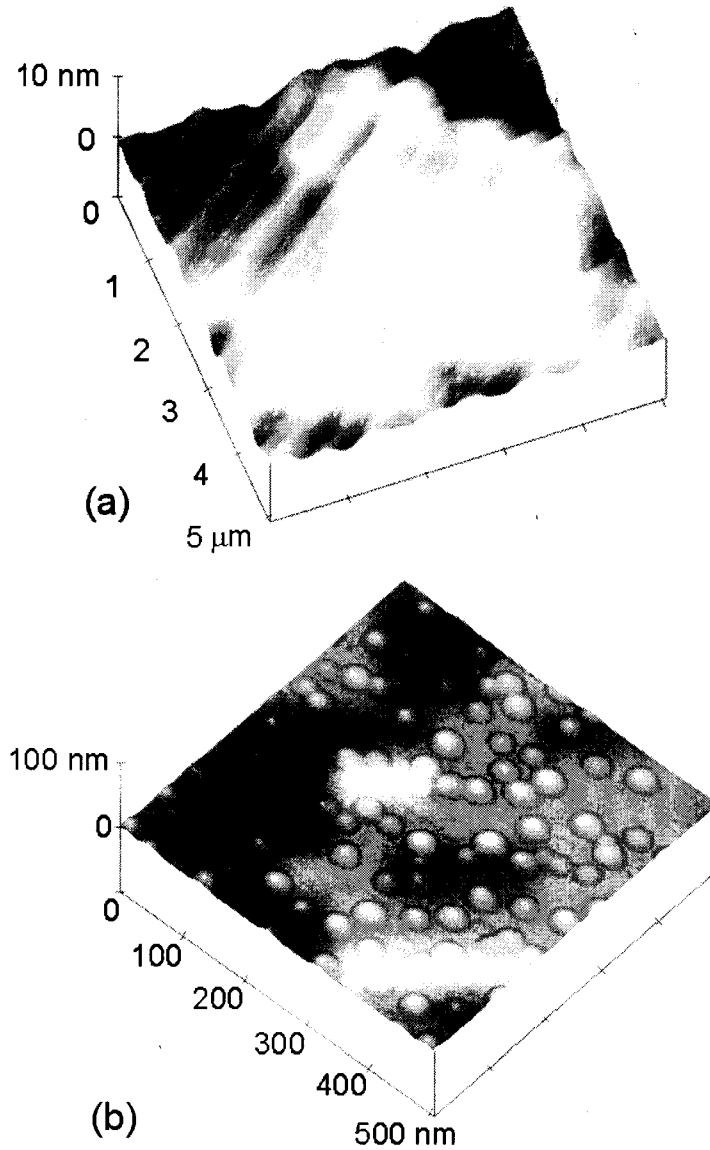


Figure 1.2: Atomic force microscope (AFM) images of the surfaces of strain-relaxed films. (a) 200 nm-thick film of $\text{In}_{0.2}\text{Ga}_{0.8}\text{As}$, for which the equilibrium lattice constant is $\sim 1.4\%$ larger than that of the GaAs substrate. The ridges are aligned along $\langle 110 \rangle$ crystal directions, and arise from the dislocation array which develops to relieve the epilayer strain. (b) Coherent islands (quantum dots) resulting from the deposition of 3 monolayers of InAs on a GaAs substrate. The equilibrium lattice mismatch is 7%.

in which case two orthogonal arrays develop, aligned along the two orthogonal $\langle 110 \rangle$ directions [Fig. 1.2(a)]. Elastic strain relaxation on the other hand can occur through the formation of long-range surface undulations, in which strain is relieved at the crests of the surface wave [9, 16, 17]. A closely related process is coherent islanding [Fig. 1.2(b)], in which discrete, three-dimensional islands form which again relieve strain elastically by virtue of their shape [18-22].

A technique which is especially suited to the real-time study of surface morphology during film growth is elastic light scattering [24, 25]. For the mirror-like substrates used in crystal growth experiments, light scattering can detect atomic-scale changes in the surface height on lateral length scales comparable to an optical wavelength [26]. This is a distinct advantage over electron diffraction techniques, which are not sensitive to the large scale structures of interest in studies of morphology in the continuum limit, due to the short coherence length of the electrons. A potential problem is that light scattering is sensitive to particles and point defects on the surface, which are difficult to distinguish from the scattering due to the surface morphology. One of the objectives of this work is to establish that light scattering measurements on epitaxial thin films can provide detailed surface roughness information, which agrees quantitatively with information obtained from atomic force microscope (AFM) measurements. In particular it is known from theory that in the smooth-surface limit, the scattered light intensity distribution maps the power spectral density (PSD) of the surface roughness [25]. The results presented in this work represent the first absolute comparison between the PSD

measured by light scattering and the PSD calculated from real-space topographic data, obtained in this case from AFM measurements on epitaxial films.

In this thesis light scattering is applied to the investigation of strained-layer film growth by molecular beam epitaxy (MBE). In particular we explore plastic strain relaxation and coherent islanding in the $\text{In}_x\text{Ga}_{1-x}\text{As}/\text{GaAs}$ system. Both of these processes are of technological importance. Coherent islanding of InAs on GaAs for example is currently exploited in the fabrication of quantum dot lasers [27], and the control of roughness resulting from plastic strain relaxation in III-V materials is an important consideration in the production of strain-relaxed buffer layers for metamorphic high electron mobility transistors (MMHEMTs) [3]. The one-dimensional surface roughness associated with dislocation formation in this system also provides a convenient experimental setting for surface growth studies. Specifically, each of the two orthogonal arrays of 1D surface ridges arrays produces an intense 1D scattering line in the scattered light distribution, which is easily distinguished from the diffuse background scattering arising from the substrate roughness, or also potentially from particles. In addition, the surface morphology dynamics in this case can be described using a one-dimensional growth equation that can be solved analytically. In this work we develop a dynamical growth model for the roughening, incorporating also the dynamics of the strain-relief process, in order to explain the real-time light scattering data. Although others have used light scattering to monitor plastic strain relaxation in III-V systems [15, 23], this is the first example of a study in which the predictions of a continuum growth equation have been compared with

both the time and length-scale dependence of the surface morphology of a growing film.

Recent technological and scientific interest in the coherent islanding process has focused on controlling the size, density and spatial positions of the islands (quantum dots). An important factor is the emergence of defective larger islands, which are believed to grow at the expense of the quantum dots [20]. In this work we have developed a novel ultraviolet light scattering apparatus, and used it to obtain the first real-time measurements of quantum dot growth. In conjunction with *ex situ* AFM measurements, we find a straightforward interpretation of the light scattering signal in terms of the size and density of the large islands. Before the large islands emerge, the scattering signal is sensitive to the spatial correlations of the quantum dots, which we conclude diffuse randomly on the substrate.

The method by which the light scattering and AFM data are to be interpreted is developed in Chapter 2 for a variety of MBE-grown films exhibiting different types of surface roughness. In Chapter 3 the experimental setup for the real-time light scattering measurements is described. A model that describes the surface morphology dynamics for the case of a film undergoing plastic strain relaxation, is developed in Chapter 4 and compared with light scattering data acquired during $\text{In}_x\text{Ga}_{1-x}\text{As}$ growth on GaAs. In Chapter 5, real-time light scattering measurements of InAs quantum dot growth are presented, which reveal how the dot distribution evolves during annealing.

Chapter 2

Surface Roughness Measurement

2.1 The Power Spectral Density Function

This thesis is concerned with the surface morphology that develops during epitaxial crystal growth. Because thin film deposition and surface diffusion processes are inherently random, the final surface morphology is also random. By this we mean that the surface is a specific realization of an infinite number of possible surfaces having the same average statistical properties. A particularly convenient measure of the roughness of a randomly rough surface is the power spectral density function (PSD), which is simply the square of the Fourier transform of the surface height distribution. Although it is not possible to reconstruct the surface from the PSD, it can be used to determine a number of important statistical properties, including the root-means-square (RMS) roughness, slope, and curvature of the surface [24].

We denote the two-dimensional PSD as g_{2D} , where

$$g_{2D}(\vec{q}) = \lim_{L \rightarrow \infty} \frac{1}{L^2} \left| \iint h(x, y) e^{i(q_x x + q_y y)} dx dy \right|^2. \quad (2.1)$$

Here $h(x, y)$ is the surface height distribution and the integration is over the projected area L^2 of the surface in the xy plane. The vector $\vec{q} = (q_x, q_y)$ denotes the spatial frequency of the surface height fluctuations, and is related to a length scale l in the plane of the surface by $q = 2\pi/l$. Note that since $h(x, y)$ is real, the PSD is symmetric: $g_{2D}(\vec{q}) = g_{2D}(-\vec{q})$.

The statistic most commonly used to describe the roughness of a surface is its RMS value σ . In terms of the PSD defined above,

$$\sigma^2 = \frac{1}{(2\pi)^2} \iint g_{2D}(\vec{q}) dq_x dq_y \quad (2.2)$$

where the integration extends over positive and negative \vec{q} . For the particular case of isotropic surface roughness, the PSD depends only on the magnitude of \vec{q} and Eq. 2.2 can be rewritten:

$$\sigma^2 = \frac{1}{2\pi} \int_{q_{\min}}^{q_{\max}} g_{2D}(q) q dq, \quad q > 0 \quad (2.3)$$

where we have indicated the limits of integration explicitly. Note that the RMS roughness depends on the limits of integration, which are set by the bandwidth of the instrument used to measure it. On the other hand, the PSD itself is defined independently of instrumental considerations. In this thesis we will use the PSD extensively to quantify surface roughness for the purposes of comparing films grown under different conditions. If we define the square of the RMS roughness as the roughness “power”, then according to Eq. 2.2 the PSD is the spectral distribution of roughness power per unit spatial frequency range.

2.2 Measuring the PSD

2.2.1 Atomic Force Microscopy

Perhaps the most important tool for characterizing thin film surface morphology is the atomic force microscope (AFM). Although it is intrinsically a real-space measurement technique, AFM has lately been used to obtain estimates of the PSD of surfaces following growth [23, 28]. The surface as measured by AFM consists of an $N \times N$ pixel grid (where N is even) of discretely sampled points of $h(x, y)$, which we denote as h_{ij} . For a measurement over an $L \times L$ area of the surface,

$$\sigma^2 = \frac{1}{L^2} \sum_{i=-\frac{N}{2}}^{\frac{N}{2}} \sum_{j=-\frac{N}{2}}^{\frac{N}{2}} g_{ij}, \quad i, j \neq 0, \quad (2.4)$$

where g_{ij} is an estimation of the PSD obtained by squaring the components of the discrete Fourier transform of h_{ij} . Each element of g_{ij} corresponds to the spatial frequency $\vec{q}_{ij} = (i, j)2\pi/L$. Note that g_{ij} does not include the DC component of the PSD ($q = 0$), because the area of the surface sampled by AFM is finite. In terms of the bandwidth limits defined in Eq. 2.3, $q_{\min} = 2\pi/L$ and $q_{\max} = N\pi/L$.

In principle, the quantity g_{ij} in Eq. 2.4 becomes numerically equal to g_{2D} in the limit that the area imaged by AFM becomes large ($L \rightarrow \infty$). The finite image-size of AFM is linked to noise in the measured PSD, as will we discuss later. In addition to this fundamental limitation, AFM is plagued by the same scanning artifacts as other scanned probe techniques, which can severely limit its ability to reproduce the PSD of the surface [28, 29]. We will discuss some of these artifacts in connection with actual AFM images

in the following sections. One class of artifacts arise from nonlinearities in the scanning mechanism (typically a piezoelectric driver), which produce distortion in the AFM image in both the lateral and vertical dimension. To some extent these effects can be minimized by careful calibration procedures.

More problematic are distortion effects associated with the finite radius of the probe tip, which tends to round out sharp features so that the diameter of high aspect ratio surface asperities is exaggerated and that of surface pits is underestimated. Note that the resulting image is not a simple convolution of the tip and surface, since some areas of the surface are inaccessible to the probe tip. The PSD will therefore be affected in ways which are difficult to predict. For example scanning a smoothly undulating surface with a finite radius probe tip can introduce high spatial frequency content into the PSD. Correcting for finite-size tip effects requires knowledge of both the tip geometry and the shape of the surface features present, neither of which is generally known. Except in cases where the tip aspect ratio is higher than that of the surface features, the AFM is not expected to yield a good estimate of the true PSD.

One instance where AFM can provide accurate measurements of the PSD, is when the atomic-height steps corresponding to terraces on the epitaxial growth surface are well resolved by the AFM. An example of such a measurement is shown in Figure 2.1(a). This is a $5 \times 5 \mu\text{m}^2$ image of the (100) growth surface of a GaAs film grown on a GaAs substrate at 590°C . The atomic step height for this system is 0.28 nm. The surface was prepared using a technique in which a flux of indium atoms is supplied to the growth

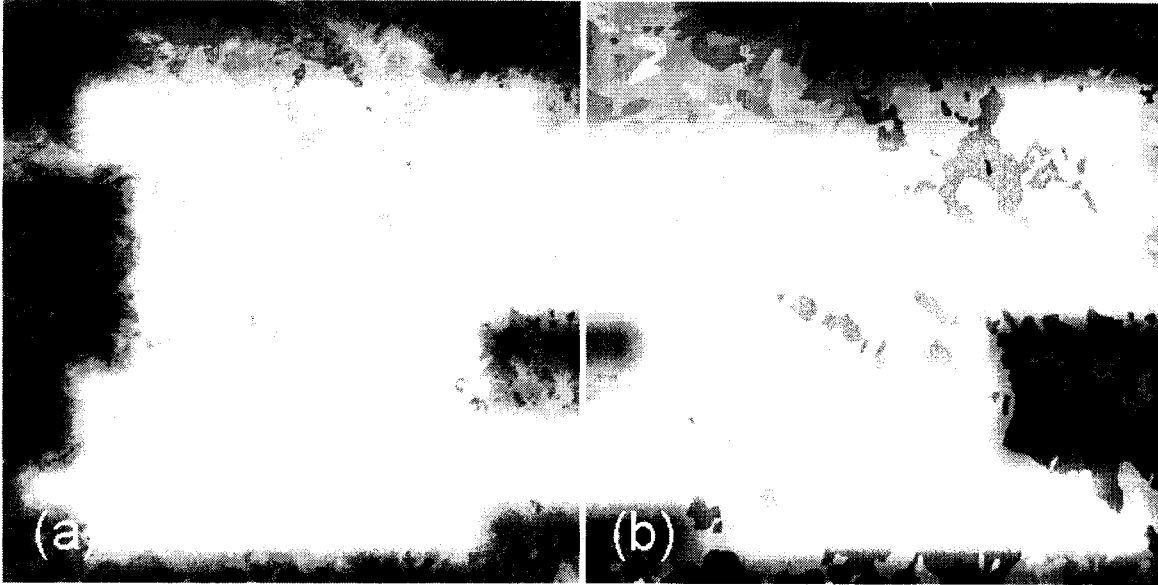


Figure 2.1: (a) $5 \times 5 \mu\text{m}^2$ AFM image of a GaAs film, showing atomically flat terraces (step height between terraces = 0.28 nm). (b) Corrected representation of the surface as discussed in the text.

surface during the GaAs deposition [30]. The In atoms do not incorporate into the film at this temperature, however their presence on the growth surface is believed to enhance the surface migration of the Ga atoms, resulting in a smoother surface. Although the steps are clearly resolved in the AFM image of this film, there is still the potential for distortion arising for example from system noise, instrument nonlinearities and rounding of the steps due to the finite radius of the probe tip. Accordingly we have produced a representation of the “true” surface, in which the terraces in the original image are replaced by perfectly flat terraces terminating in abrupt, 0.28 nm-height steps. This is shown in Fig. 2.1(b). Note that the terrace widths are relatively wide compared to a typical AFM probe tip radius (< 50 nm), so that the corrected image is expected to be an accurate representation

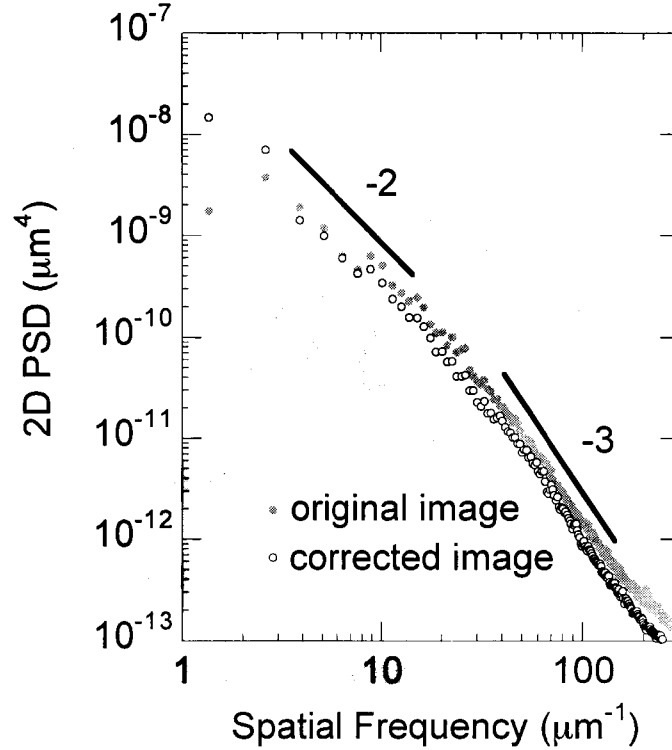


Figure 2.2: Comparison of the isotropic 2D power spectrum calculated from the AFM image in Fig. 2.1(a), and from the corrected image in Fig. 2.1(b). Lines of slope -2 and -3 are shown for reference.

of the actual surface. The 2D PSD (g_{ij}) of this surface, determined from the discrete Fourier transform of the image, was approximately isotropic. In Figure 2.2 we plot the isotropic average of the 2D PSD, obtained from the original image and from the corrected version. The excellent agreement indicates that for relatively flat surfaces in which the atomic-height terraces are well resolved, the AFM gives an accurate representation of the true PSD of the surface.

The PSD of this film displays a power law roll-off with spatial frequency. The power law is approximately -2 for q less than $10 \mu\text{m}^{-1}$ and -3 at higher spatial frequencies. A

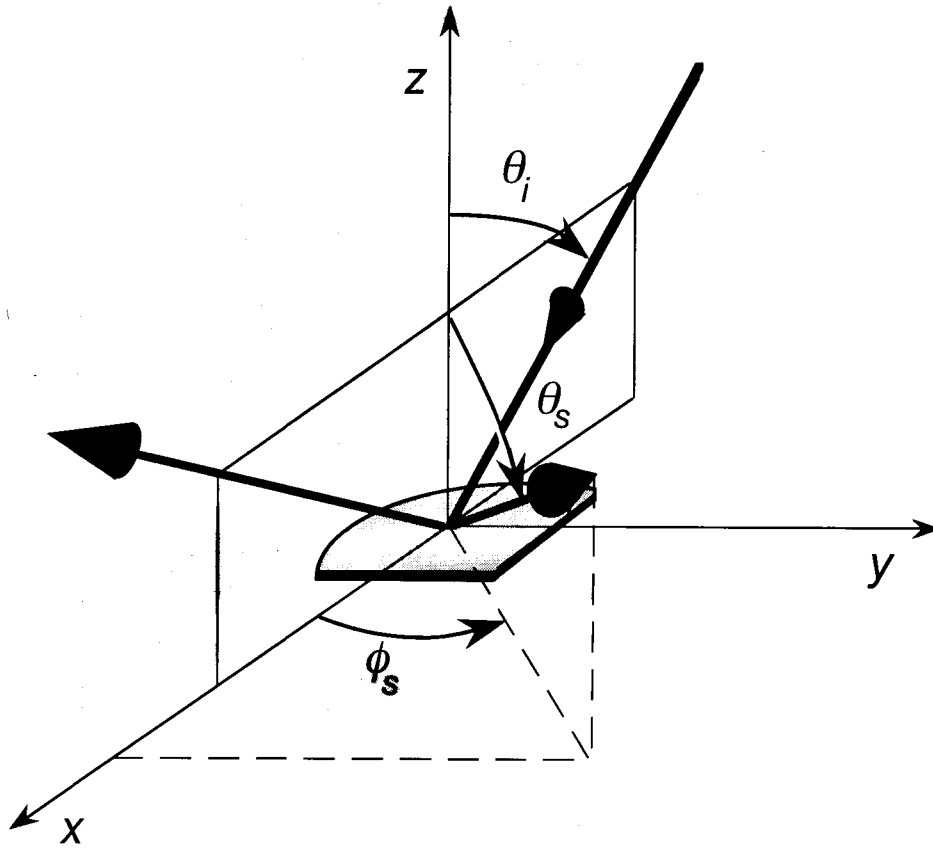


Figure 2.3: Scattering angles for the case where the plane of incidence is aligned with the x -direction. The specular beam is also shown.

transition from a -2 power law at low q to a more rapid roll-off at high q is generally seen in all of our GaAs buffer layers. The origin of this transition has been explained in terms of a continuum model for MBE growth [4], as we discuss further in Section 4.2.

2.2.2 Elastic Light Scattering

Elastic light scattering is an alternative surface morphology probe which has recently been applied to the study of epitaxial film growth [15, 19, 31]. The theoretical and

technical aspects of light scattering are reviewed in a recent book by Stover [24]. In this technique, a beam of light is incident at an angle θ_i from the surface normal, as shown in Fig. 2.3. For the mirror-like surfaces of interest here, most of the light is specularly reflected. We are interested in the small component of the light that is diffusely scattered due to diffraction from features in the surface topography. The angular distribution of the scattered light intensity in the far field maps out the PSD of the surface. Specifically, the differential optical power dP scattered into the solid angle $d\Omega$ is proportional to g_{2D} according to [25]

$$\frac{dP}{P_0 d\Omega} = \frac{16\pi^2}{\lambda^4} \cos \theta_i \cos^2 \theta_s Q(\theta_i, \theta_s, \phi_s) g_{2D}(\vec{q}) \quad (2.5)$$

where P_0 and λ are the incident optical power and wavelength respectively. The factor Q , sometimes called the polarization factor, characterizes the polarization-dependent reflectivity of the surface, and is a function of the complex dielectric constant of the material as well as the incident and scattering angles. Expressions for Q are available in the literature [25], and are given in Appendix A. These reduce to the usual reflectance expressions for the case of scattering in the specular direction. For the *ex situ* light scattering measurements discussed in this chapter, the angular variation of Q is minor compared to that of the angle-dependent prefactors in Eq. 2.5, and the angular variation associated with the spatial frequency dependence of the surface roughness. The spatial frequency of roughness probed is related to the scattering angles θ_s and ϕ_s by

$$\begin{aligned} q_x &= \frac{2\pi}{\lambda} (\sin \theta_i - \sin \theta_s \cos \phi_s) \\ q_y &= -\frac{2\pi}{\lambda} \sin \theta_s \sin \phi_s. \end{aligned} \quad (2.6)$$

The highest q accessible is therefore $4\pi/\lambda$, corresponding to backscattering of grazing incidence ($\theta_i = 90^\circ$) light. Thus light scattering is able to detect roughness on length scales no shorter than $\lambda/2$. In order to detect low- q roughness, it is necessary to measure the scattering in near-specular directions. Although the longest length scale detectable is limited in principle only by the spatial coherence length of the light source, access to these near-specular signals is often limited in practice by stray light, associated with scattering of the specular beam from optical elements near the specular position. Most of the measurements in this thesis were made in the plane of incidence ($\phi_s = 0$). In this case the measurements are sensitive to roughness along one direction only, namely a direction in the surface that is parallel to the plane of incidence.

Elastic light scattering offers a number of advantages over AFM. In contrast to AFM and other real-space techniques, light scattering is directly sensitive to the PSD according to Eq. 2.5, which is often the quantity of most interest. Light scattering is also fundamentally a two-dimensional technique, whereas an AFM image consists of a compilation of hundreds of sequential 1D profiles. This can introduce distortions in the PSD obtained from AFM since spatial correlations in the slow scan direction are lost due to instrument drift during the course of the image acquisition. Surface statistics obtained in a light scattering measurement are also more reliable in the sense that they represent an average over the illuminated area, which is up to 50 mm^2 in these experiments, whereas the AFM scan areas are typically less than 0.01 mm^2 . The most important advantage of light scattering in this work is its suitability to real-time monitoring during thin film

growth, since the roughness information is instantaneously obtained without need for growth interruption.

Eq. 2.5 is expected to hold if the amplitude of the surface roughness is much less than the incident wavelength [24]. For the surfaces of interest here, RMS roughness values are typically < 2 nm over $50 \times 50 \mu\text{m}^2$ areas according to AFM, which is less than 1% of the smallest wavelength used in these experiments. Another restriction is that the film must be free of defects and particles, which produce intense multi-directional scatter [32] that is generally detectable by eye. Care was taken during the light scattering measurements to ensure that no defects or particles were visible within the area of the sample illuminated by the probe beam.

2.2.3 One-Dimensional Roughness

In some cases the roughness of a surface is intrinsically one-dimensional, for example in the case of a 1D diffraction grating. One can then define a one-dimensional PSD. In terms of the continuous and discrete forms g_{1D} and g_i of the 1D PSD,

$$\begin{aligned}\sigma^2 &= \frac{2}{2\pi} \int_{q_{\min}}^{q_{\max}} g_{1D} dq_x \\ &= \frac{2}{L} \sum_{i=1}^{\frac{N}{2}} g_i\end{aligned}\tag{2.7}$$

where the roughness is taken to be along the x -direction, and the same bandwidth limits are assumed for both expressions. We have included a factor of 2 in each expression to account for the negative spatial-frequency component of the PSD. In order to ensure that the two expressions yield the same value for the RMS roughness, it is necessary that the sampled length L of the 1D surface profile be sufficient in each case to obtain reliable

statistics.

The PSD associated with 1D roughness in the x -direction is nonzero only along the line in q -space defined by $q_y = 0$. In terms of the 2D PSD defined by Eq. 2.1, the width Δq_y of this line is zero: $g_{2D} = g_{1D}\delta(q_y)$. For any real measurement of the 2D PSD however, Δq_y depends on the spatial frequency resolution of the instrument. AFM and light scattering measurements of a 1D roughness profile will therefore produce different estimates of the 2D PSD, since the true 1D roughness power is averaged over different resolution functions in each case. In the case of the 2D power spectrum determined from a distortion-free AFM image, the resolution is the width of a single pixel ($\Delta q_y = 2\pi/L$). For a light scattering measurement the resolution is determined by the detector solid angle.

For a light scattering measurement in which the plane of incidence coincides with the 1D roughness profile, the intensity distribution is confined to the plane of incidence. The scattered intensity therefore falls on a line whose width is diffraction limited if the focal point of the illumination source is at the detector. The non-zero width of the scattering line arises from the fact that the illumination of the 1D roughness is not infinite in extent perpendicular to the scattering plane. This is analogous to the case of an AFM measurement of 1D roughness in the x -direction: Δq_y is inversely related to the width of the image in the y -direction. The angular variation of the scattering intensity within the plane of incidence is given by [25]

$$\frac{dP}{P_0 d\theta_s} = \frac{16\pi^2}{\lambda^3} \cos \theta_i \cos^2 \theta_s Q(\theta_i, \theta_s) g_{1D}(q_x) \quad (2.8)$$

This expression can be compared with Eq. 2.5 for 2D scattering to determine the appropriate correction factor for converting the measured 2D spectrum to the true 1D value. A similar conversion factor can be found for the case of the discrete PSD measured by AFM, for example by comparing the final expression in Eq. 2.7 with Eq. 2.4, and noting that for 1D roughness g_{ij} is zero for all $j \neq \pm 1$. These considerations imply the following relationships between the measured 2D PSD determined from light scattering and AFM respectively, and the true 1D PSD of a surface with 1D roughness:

$$g_{1D} \leftarrow \frac{\pi r}{2\lambda d} g_{2D}, \quad g_i \leftarrow \frac{1}{L} g_{ij} \quad (2.9)$$

where r is the radius of the detector used to collect the scattered light and d is its distance from the sample. These relationships will be used in Section 2.3.5 to compare AFM and light scattering measurements of a sample containing 1D roughness.

2.3 Comparison of Light Scattering and AFM

In this section we apply the results from Section 2.2 to compare measurements of the PSD obtained by light scattering and AFM, for surfaces exhibiting different types of roughness.

2.3.1 Sample Preparation

All of the growth experiments presented in this thesis were performed on undoped (001)-oriented ($\pm 0.5^\circ$) single-crystal GaAs substrates. The substrates consist of circular wafers that are 50 mm in diameter and nominally 500 μm thick. The manufacturer specifies

that the substrates are epi-ready, so that no chemical treatments are required to clean the growth surface. In order to minimize particulate contamination of the substrates, all pre-growth sample preparation steps were carried out under a laminar flow hood, and the number of steps was kept to a minimum. Each wafer was removed from its clean-room sealed container and cleaved along the $\langle 110 \rangle$ directions into four quarter circles. Due to the high crystalline perfection of the substrate material, the cleaving procedure can be accomplished without significant generation of particulates. The wafer was cleaved with the growth surface oriented upwards to avoid contact of the growth surface with the working surfaces in the laminar flow hood. Each quarter wafer segment was then individually mounted onto a molybdenum sample holder with spring-loaded molybdenum clips [33]. After mounting the wafer, each holder was always oriented such that the growth surface was oriented downwards. The wafer holders were sequentially inserted into a UV-ozone reactor for 10 minutes. This increases the native oxide thickness and in so doing moves residual surface contamination away from the oxide/GaAs interface [34]. The holders were then loaded, growth surface downwards, into a carrier rack which was then transferred to the load lock of the MBE growth system and evacuated to UHV. Recently a laminar flow hood has been installed above the load lock and an air-tight transfer container has been used, in order to minimize contamination from air-borne particulates during transfer of the carrier rack to the load lock.

The growth experiments were carried out in a VG-V80H MBE deposition system, equipped with solid-source effusion cells for both the group III and group V elements

[35]. A typical base pressure in the MBE growth chamber, obtained with the combined pumping of an ion pump, a liquid helium cryopump and a liquid nitrogen cryoshroud, is 5×10^{-10} mbar. This pressure is mainly associated with hydrogen according to a residual gas analyzer located in the growth chamber. Reflection high-energy electron-diffraction (RHEED) was used during the growth experiments to monitor changes in short-range surface structure associated with the oxide desorption and quantum dot formation to be discussed in the next section. The substrate temperature was monitored throughout growth using a diffuse reflectance spectroscopy (DRS) apparatus [36], which has an absolute accuracy of $\sim 10^\circ\text{C}$ and a relative precision between runs of $\pm 2^\circ\text{C}$.

2.3.2 Measurement Technique

Various *in situ* light scattering setups were implemented in order to study different aspects of the surface morphology evolution during growth. These will be described in Section 3. The results of the real-time light scattering measurements form the basis of much of this thesis, and will be discussed in detail in the following chapters. Here we focus on the comparison of light scattering and AFM measurements both performed *ex situ* on the same samples. Unlike the *in situ* measurements, in which only a few discrete scattering angles are accessible for any given setup, the *ex situ* light scattering measurements are performed over a continuous range of scattering angles, so that the PSD is measured over a continuous spatial frequency range. In order to preserve the surface morphology for the *ex situ* measurements, the substrate heater power was turned

off immediately after growth. Using this procedure, the substrate temperature drops below 300 °C within 5 minutes by radiative cooling to the liquid nitrogen cryoshroud. With the notable exception of quenches performed during the early stages of quantum dot growth (Chapter 5), the *in situ* light scattering signals are found to remain stable during the quench.

For the *ex situ* light scattering measurements [34] *s*-polarized light from a HeNe laser ($\lambda = 632.8$ nm) was incident at 65° from the sample normal, and scattering was detected in the plane of incidence using a silicon diode detector equipped with an optical bandpass filter ($\Delta\lambda = 10$ nm). The laser beam was chopped at 400 Hz and lock-in detection electronics were used in order to detect the diffusely scattered optical power, which is typically 10 orders of magnitude lower than that of the specular beam. The light was focused to a ~ 0.5 mm diameter spot at the specular position in the detection plane using a long focal length lens between the laser and the sample, so that the spot diameter on the sample was about 3 mm. The radius r of the detector was 1.3 mm and its distance d from the sample was 235 mm. The 2D PSD was calculated from the angular dependence of the detected optical power using Eq. 2.5. The angular dependence of the factor Q for this setup is plotted in Appendix A. The angular range accessible in these *ex situ* measurements corresponds to a spatial frequency range of 0.2 to 16 μm^{-1} .

The AFM measurements presented in this thesis were obtained using several different instruments, however results obtained on the same samples were found to be consistent between instruments. In the case of samples measured by *ex situ* light scattering, the

AFM measurements were made more than one year after the growth experiments and *ex situ* light scattering measurements, by which time the samples had been exposed to significant particulate contamination. Since the AFM scan areas are much smaller than the area probed by the incident light beam in the scattering measurements, it was generally possible to choose areas on the sample that were free of visible particles, but still within a few millimetres of the region probed by light scattering.

It is worth noting that for the *ex situ* roughness measurements, the surfaces will have oxidized. The native oxide for these GaAs samples is expected to be up to 1 nm thick [37]. This implies for example that the terraces in Fig. 2.1 are likely to be completely oxidized. The fact that the atomic steps are still well defined, with a step height equal to that of an unoxidized GaAs step, indicates that the oxidized surface measured by AFM is a close approximation to the initial, unoxidized surface. In the case of light scattering, we note that the oxide thickness is much less than an optical wavelength so that the effect of oxidation on the reflectivity is negligible.

2.3.3 Isotropic 2D Roughness: Oxide-Desorbed GaAs

The final processing step prior to growth is to remove the oxide from the GaAs substrate. For the growth experiments discussed in this thesis, the oxide removal is achieved by heating the substrate to over 600 °C in the MBE growth chamber. This temperature is near the congruent sublimation point of GaAs (640 °C) above which the arsenic vapor pressure exceeds that of gallium [35]. An overpressure of arsenic is therefore supplied to

inhibit decomposition of the surface into gallium droplets. Prior to oxide desorption, a hazy, featureless RHEED pattern is obtained from the substrate, due to the disordered structure of the oxide. As the oxide evaporates during heating, diffraction spots appear in the RHEED pattern, reflecting the crystalline structure of the exposed GaAs surface [35].

A $20 \times 20 \mu\text{m}^2$ AFM image of a GaAs substrate obtained following thermal desorption of the oxide is shown in Figure 2.4(a). The vertical dimension is represented by a linear gray scale, which is shown for reference in the inset. The oxide desorption process results in the formation of large pits as shown in the image. These pits are also observed in measurements of similar samples using scanning electron microscopy and scanning tunneling microscopy [38].

The two-dimensional power spectrum of the surface roughness, obtained from the Fast Fourier Transform (FFT) of a $50 \times 50 \mu\text{m}^2$ image of the same sample in Fig. 2.4(a), is shown in Figure 2.4(b). This is a semilog plot in which the axes shown span a spatial frequency range in each direction of $\pm 17 \mu\text{m}^{-1}$ on a linear scale, and a logarithmic gray scale has been used to represent the magnitude of the PSD at each spatial frequency. In this case the gray scale, which spans a dynamic range of approximately 3 decades, is inverted so that higher power densities appear as darker pixels. The spatial frequency axes coincide with the real-space axes in the AFM image, and are oriented approximately along the $\langle 100 \rangle$ crystal directions. The DC component of the PSD is at the origin ($q = 0$). The PSD is seen to be isotropic, with a broad ring of high power density which peaks

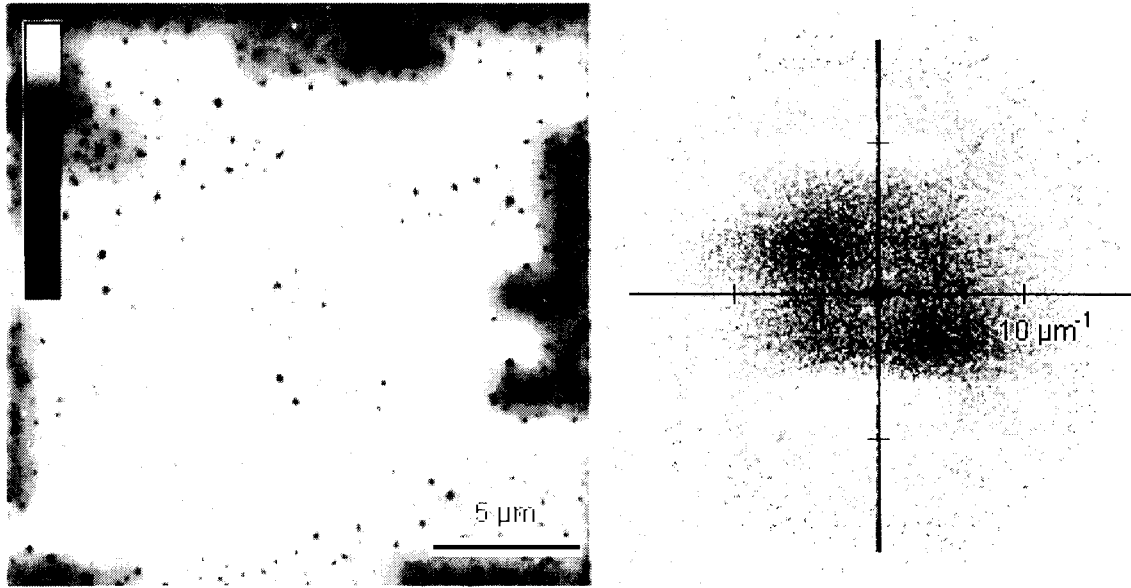


Figure 2.4: (a) AFM image and (b) two-dimensional power spectrum of a GaAs substrate from which the oxide has been thermally desorbed. The gray scale bar in (a) corresponds to a vertical range of 50 nm. In (b) a logarithmic gray scale is used, which spans 3 decades.

at approximately $4 \mu\text{m}^{-1}$. The ring in the PSD is due to roughness associated with the large pits, which are spaced on a length scale of between 1 and $2 \mu\text{m}$ in the AFM image.

The power spectrum computed from the AFM data is characterized by high-contrast variations on small spatial-frequency scales. This gives the data in Fig. 2.4(b) a noisy appearance, which is inherent to power spectral estimation techniques based on finite-sized samples of random processes [39]. This effect is closely related to the speckle noise that one observes in the intensity distribution of coherent light which scatters from a randomly rough surface. In both cases the fine-structure variations are specific to the details of the surface structure within the particular area measured. The larger-scale variations on the other hand are due to the overall statistical properties of the

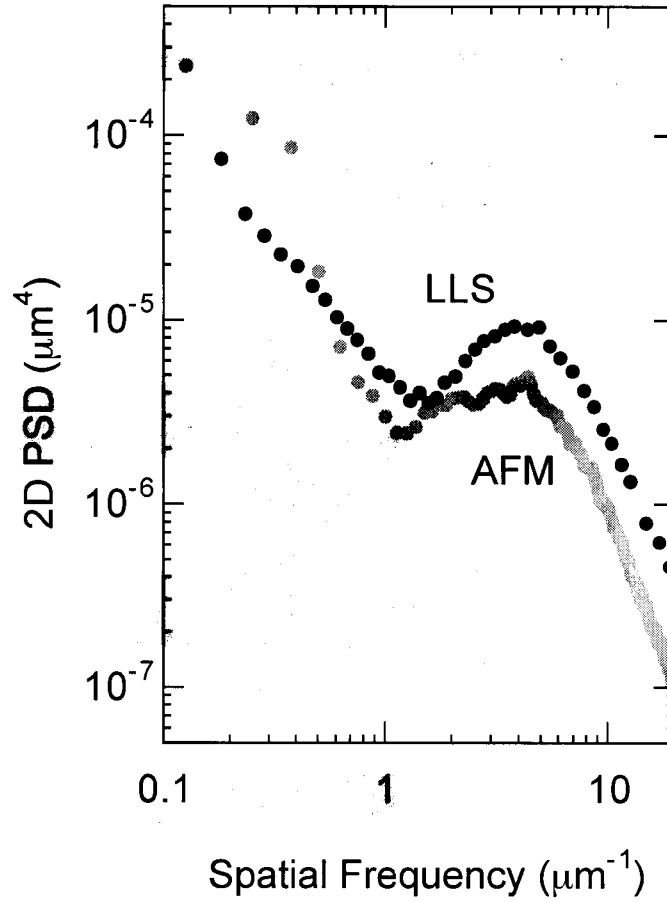


Figure 2.5: Comparison of light scattering and AFM measurements of the isotropic 2D PSD, for the oxide-desorbed surface in Fig. 2.4.

surface, which is what we are most interested in here. In the case of the light scattering measurements, the speckle noise is averaged over by the solid angle of the detector. For the purposes of comparing the AFM and light scattering measurements, which are necessarily obtained over different areas, it is therefore appropriate to average the noise in the PSD obtained from the AFM data. Since the PSD is isotropic in the present case, this can be achieved by averaging the PSD over all directions.

The isotropic 2D PSD obtained by averaging the data in Fig. 2.4(b) over all directions, is compared with light scattering measurements obtained from the same sample in Figure 2.5. In order to minimize artifacts associated with the scanning process of the AFM, the directions that coincide with the axes in Fig. 2.4(b) were omitted in the average. In the case of the light scattering measurements [34] the plane of incidence was chosen to coincide with a $\langle 100 \rangle$ crystal direction, and the 2D PSD was calculated using Eq. 2.5. The agreement between the AFM and light scattering data is remarkable, given that they were obtained by such different techniques. Note that both AFM and light scattering give an absolute measurement of the PSD. No scaling of the data sets has been performed to obtain the curves in Fig. 2.5. Both techniques reveal a peak in the PSD at a spatial frequency of $\sim 4 \mu\text{m}^{-1}$. The magnitude of the peak in the light scattering data is higher by a factor of about two. This is not surprising since the roughness is mainly in the form of pits. Due to the finite radius of the AFM probe tip, the AFM will always underestimate the volume of a pit, resulting in an underestimate of the PSD. In the present case the discrepancy is relatively minor considering that the measured dynamic range of the PSD is more than two decades.

2.3.4 Anisotropic 2D Roughness: GaAs Buffer Layer

A GaAs buffer layer is typically grown following evaporation of the oxide, in order to smooth the roughness associated with the desorption pits. During the buffer layer growth the diffraction spots in the RHEED pattern elongate into streaks, which are oriented

along the direction perpendicular to the substrate. The transition from a spotty RHEED pattern to a streaky pattern reflects the transition from a 3D growth front associated with the rough, oxide-desorbed surface, to a 2D growth front associated with the smoother surface of the buffer layer [35].

For the growth experiments in this thesis, the buffer layers were grown at a substrate temperature of between 580 and 600 °C, at a rate of $\sim 1 \mu\text{m/hr}$. A $20 \times 20 \mu\text{m}^2$ AFM image of the surface morphology following growth of a $1 \mu\text{m}$ thick GaAs buffer layer at 590 °C is shown in Figure 2.6, together with the PSD calculated from a $50 \times 50 \mu\text{m}^2$ image of the same sample. The crystallographic orientation of the AFM image and the PSD is the same, and is indicated in the figure. The overall roughness has been reduced dramatically compared to that of the initial thermally cleaned substrate. The RMS roughness in this image is an order of magnitude smaller than that in Fig. 2.4. In contrast to the isotropic roughness resulting from the oxide desorption process, the surface morphology associated with the GaAs buffer layer growth is anisotropic. In particular, the roughness consists of mounds elongated along the $[1\bar{1}0]$ crystal direction. This anisotropy is attributed to differences in the surface diffusion along the two $\langle 110 \rangle$ directions, which we study further in Chapter 4. The elongation of the mounds produces a corresponding elongation in the 2D power spectrum, which reflects the greater amount of high spatial frequency roughness along $[110]$ relative to $[1\bar{1}0]$.

The 2D PSD from Fig. 2.6(b) determined from AFM is compared with light scattering measurements on the same sample in Figure 2.7. In this case, the PSD determined from

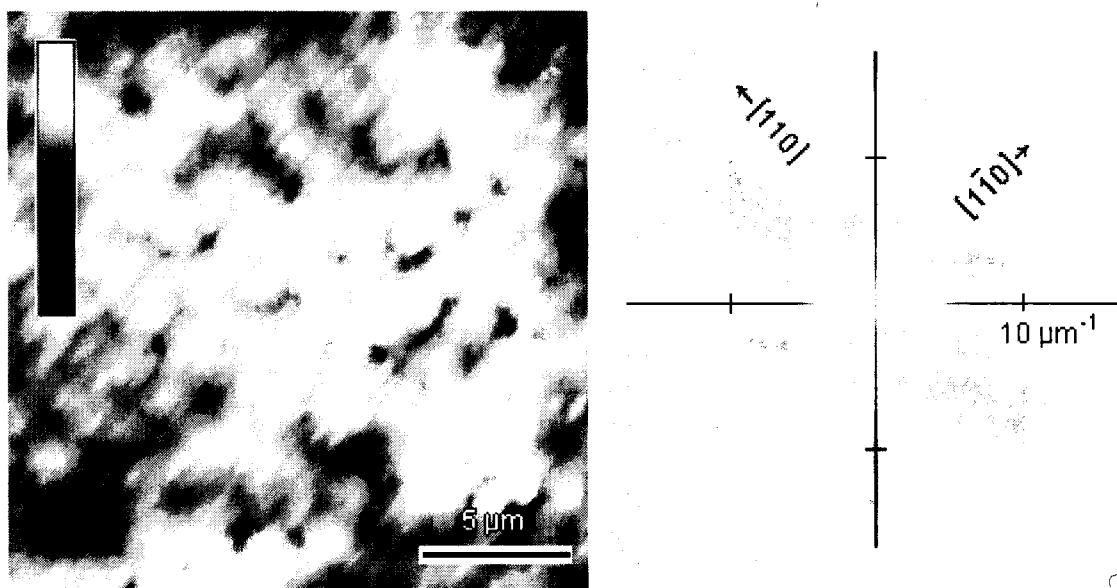


Figure 2.6: (a) AFM image (gray scale = 10 nm) and (b) 2D PSD (logarithmic gray scale) of a $1\ \mu\text{m}$ thick GaAs buffer layer grown on a substrate from which the oxide has been removed thermally.

AFM was averaged over an angular range of 16° about each $\langle 110 \rangle$ direction to obtain an estimate of the PSD in each direction. Light scattering measurements were obtained along each $\langle 110 \rangle$ direction as indicated. Again the AFM and light scattering data agree within a factor of two, over the spatial frequency range of 1 to $6\ \mu\text{m}^{-1}$. Both techniques detect the same crystallographic anisotropy in the surface roughness, and display the same shoulder in the PSD at $\sim 3\ \mu\text{m}^{-1}$. In order to remove bow in the AFM image caused by nonlinearities in the scanning mechanism, a third order polynomial was subtracted from each scan line in this data. This procedure also removes the low-spatial frequency roughness in the image, which explains the discrepancy between the AFM and LLS data below $1\ \mu\text{m}^{-1}$. The light scattering data diverge from the AFM data when the PSD drops

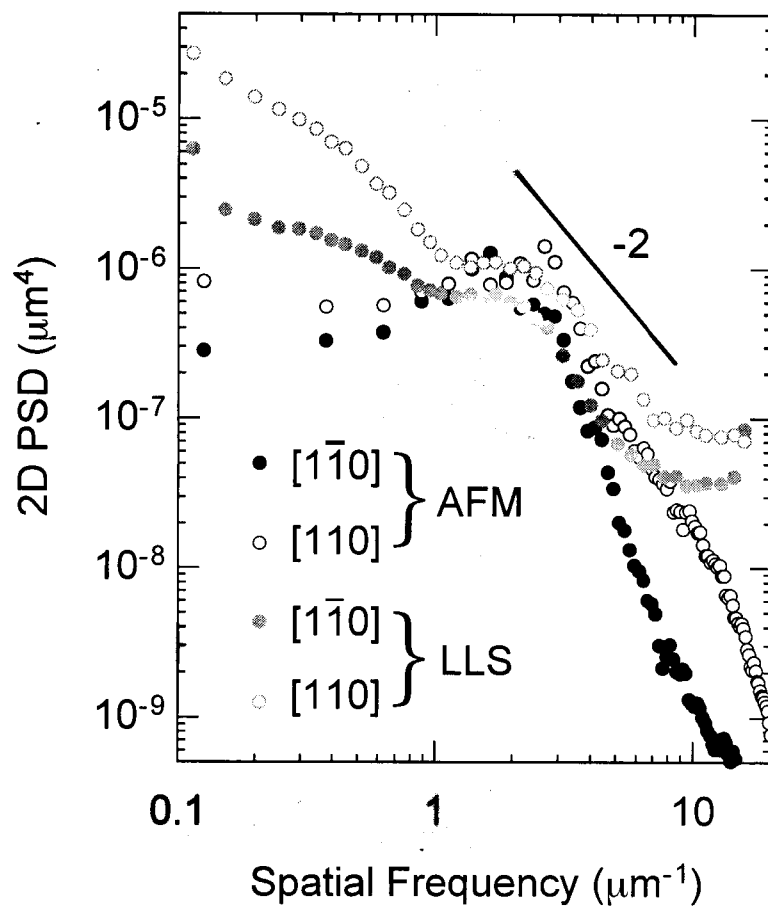


Figure 2.7: Light scattering and AFM measurements of the 2D PSD along the two orthogonal $\langle 110 \rangle$ directions, for the GaAs buffer layer in Fig. 2.6. A line of slope -2 is shown for reference.

below $\sim 10^{-7} \mu\text{m}^4$. This could be because the scattered light intensity is low enough that background scattering or scattering from defects and particles is becoming important.

2.3.5 1D Roughness: InGaAs on GaAs

The growth of $\text{In}_x\text{Ga}_{1-x}\text{As}$ on GaAs will be discussed in Chapter 4. Owing to the compressive lattice mismatch of the InGaAs epilayer relative to the GaAs substrate, dislocations form at the substrate/epilayer interface during growth to relieve the mismatch strain. This process results in a distinctive crosshatch pattern in the surface morphology of the film, which is shown in the AFM image in Figure 2.8. In this case a 250 nm thick film of $\text{In}_{0.18}\text{Ga}_{0.82}\text{As}$ was deposited immediately following growth of a GaAs buffer layer. The elongated mounds associated with the buffer layer growth persist during the InGaAs growth, and are clearly visible in the image. Also visible are the criss-crossing lines arising from the strain relief process.

The large scale AFM image (approximately $50 \times 50 \mu\text{m}^2$) in Fig. 2.8(a) is distorted due to nonlinearities in the scanning mechanism. In particular the crosshatch pattern is known to consist of two orthogonal arrays of ridges aligned precisely along the $\langle 110 \rangle$ crystal directions [15, 31]. The roughness associated with each of these orthogonal arrays is therefore one-dimensional. For example, light incident normal to the surface will be scattered primarily in two orthogonal planes that coincide with the $\langle 110 \rangle$ directions in the crystal surface [34]. By analogy, the power spectrum associated with the crosshatch must also consist of two orthogonal lines oriented along the $\langle 110 \rangle$ directions. The distortion

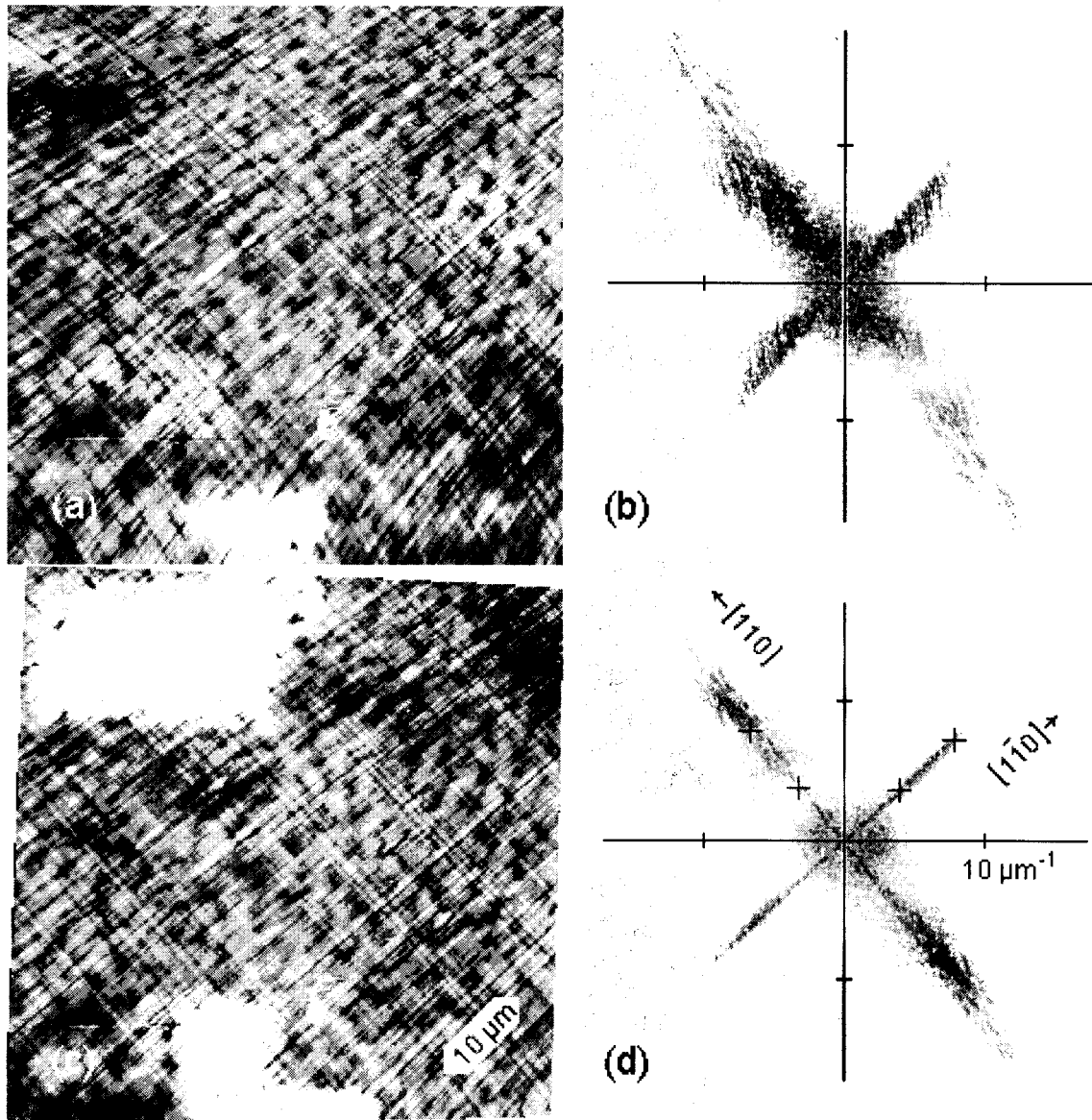


Figure 2.8: AFM image (5 nm vertical gray scale range) and PSD (logarithmic gray scale) before and after distortion correction. The sample consists of a 250 nm thick layer of $\text{In}_{0.18}\text{Ga}_{0.82}\text{As}$ grown on a 1 μm thick GaAs buffer layer.

in the AFM scan results in an angular spread in the PSD shown in Fig. 2.8(b), causing the expected 1D cross pattern to be blurred into a fan shape.

In order to facilitate comparison of the AFM measurements with light scattering data, an image processing package [40] was used to correct for the instrumental distortion of the AFM. Using the same instrument settings as used during acquisition of the image in Fig. 2.8(a), a scan was made of a two-dimensional grating calibration standard, which had a known pitch of $1\text{ }\mu\text{m}$. Grating coordinates in the resulting image were then manually mapped onto a $1\text{ }\mu\text{m}$ pitch square grid, and this information was used by the software to obtain a two-dimensional third-order polynomial mapping function. This mapping function was applied to the image in Fig. 2.8(a) to generate the distortion-corrected image shown in Fig. 2.8(c). The same mapping function was used to correct other large scale images obtained with this AFM, including the image used in calculating the PSD in Fig. 2.6(b), however most of the AFM measurements discussed in this thesis were acquired using instruments in which lateral distortion effects were compensated by the image acquisition software.

The 2D PSD calculated from a $50 \times 50\text{ }\mu\text{m}^2$ section of the corrected AFM image is shown in Fig. 2.8(d). The four crosses indicate the four spatial frequencies monitored by *in situ* light scattering during the growth of the InGaAs sample discussed in Section 4.5.1. The 1D and 2D roughness can easily be distinguished in this plot. There is a broad ellipse elongated along $[110]$ associated with the GaAs buffer layer mounds discussed in Section 2.3.4. This roughness is two-dimensional in character and results in

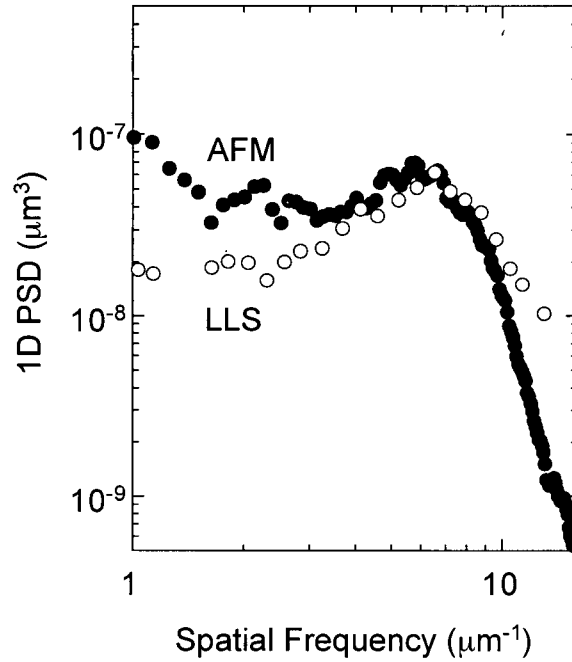


Figure 2.9: Light scattering and AFM measurements of the 1D PSD along the $[1\bar{1}0]$ crystal direction, for the relaxed InGaAs film in Fig. 2.8.

a diffuse background intensity in the scattered light distribution. Superimposed on the 2D background is a cross pattern aligned with the $\langle 110 \rangle$ directions, associated with the $\langle 110 \rangle$ -oriented crosshatch pattern in the relaxed InGaAs film. This roughness is fundamentally one-dimensional as discussed above, and produces a sharp cross in the scattered light distribution whose width is limited by the divergence of the light source.

There is still an angular spread in the cross pattern in Fig. 2.8(d) due to residual distortion in the AFM image. In other words the contributions to the 1D PSD in each $\langle 110 \rangle$ direction are artificially spread out over the azimuthal dimension. In order to extract the true 1D PSD from this data, it is therefore necessary to project these contributions back

onto a 1D vector that depends only on the magnitude of q . Accordingly, an angular sum was performed in which contributions to the PSD at a given magnitude of q , and within an angular deviation of $\pm 10^\circ$ from the $[1\bar{1}0]$ direction were added together. Note that this procedure also projects the 2D background roughness present within this angular range onto the same 1D vector. We approximate this diffuse background contribution as the average of two similar projections, performed along the directions adjacent to the $[1\bar{1}0]$ projection. This average background is then subtracted from the $[1\bar{1}0]$ projection to obtain the net contribution to the 2D PSD along $[1\bar{1}0]$ from the 1D crosshatch. The final result is multiplied by $1/L$ (see Eq. 2.9) to obtain an estimate of the true 1D PSD, and is plotted in Figure 2.9.

A procedure analogous to the one used for the AFM data was also used to determine the 1D PSD from the light scattering measurements. In this case the contribution to the scattering along $[1\bar{1}0]$ from the buffer layer roughness was approximated by the scattering measured along a $\langle 100 \rangle$ direction. The scattering along $[1\bar{1}0]$ arising from the crosshatch, approximated by the difference in the scattering along the $[1\bar{1}0]$ and $\langle 100 \rangle$ directions, was multiplied by the factor in Eq. 2.9 to obtain the curve in Fig. 2.9. Again the agreement with the AFM measurement is quite remarkable given the complexity of the data analysis procedure required to obtain the 1D PSD in both cases. The absolute magnitudes agree within a factor of two over the spectral range of 2 to $16 \mu\text{m}^{-1}$. Both measurements display a peak in the 1D PSD along $[1\bar{1}0]$ at $\sim 6 \mu\text{m}^{-1}$, of $1.3 \times 10^{-7} \mu\text{m}^3$. The physical origin of the peak in the PSD of the crosshatch pattern is the subject of Chapter 4. In

principle the same analysis can be performed on the 1D roughness in the $[110]$ direction, however owing to the anisotropy in the buffer layer roughness, the $\langle 100 \rangle$ scattering is not expected to be a reliable estimate of the 2D background in this direction.

2.3.6 High Aspect Ratio Roughness: Quantum Dots

The growth of InAs quantum dots on GaAs will be discussed in Chapter 5. The InAs/GaAs system is characterized by a 7% lattice mismatch such that an InAs film grown on GaAs is compressively strained. If a thickness of InAs exceeding the critical thickness (about 1.6 monolayers) is deposited, the strain energy associated with the lattice mismatch drives a morphological transition in which the InAs film spontaneously orders into small, three-dimensional islands. This transition is signaled in the RHEED measurement, which reverts from a streaky 2D pattern to a spotty 3D pattern. The final processing step in quantum dot formation involves the growth of a GaAs capping layer to bury the islands. Since we will be interested in the evolution of the island distribution prior to capping, the islands studied here are uncapped.

Figure 2.10(b) is a $1 \times 1 \mu\text{m}^2$ AFM image of a film in which 3 monolayers of InAs were deposited on a GaAs buffer layer, and annealed for 2 minutes at 490°C . The small, nearly identically-sized structures in this image are coherently strained islands, referred to in the literature as quantum dots (QDs). A $2 \times 2 \mu\text{m}^2$ image of the same film is shown in Fig. 2.11. For the purposes of presentation this image has been digitally filtered to have the appearance of illumination from the right. This sacrifices the gray scale information

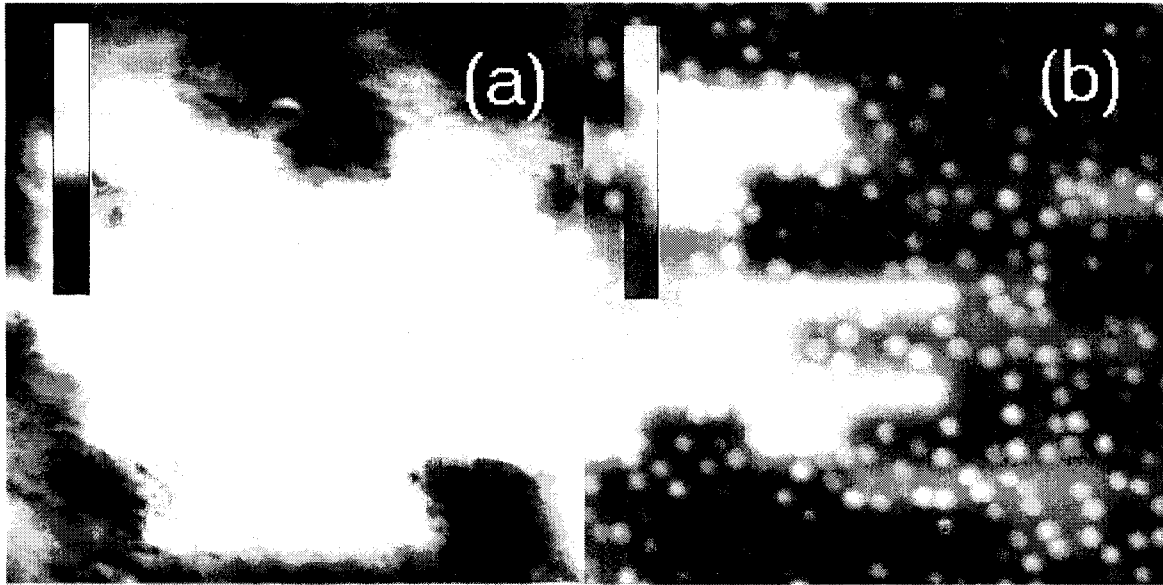


Figure 2.10: (a) $2 \times 2 \mu\text{m}^2$ AFM image of a bare GaAs buffer layer and (b) $1 \times 1 \mu\text{m}^2$ AFM image of a buffer layer on which 3 ML of InAs was deposited and annealed for 2 minutes at 490°C . The gray scale bars in (a) and (b) correspond to a vertical range of 4 nm and 30 nm respectively.

in the image but enhances the sensitivity to fine detail. This larger scale image reveals two distinct populations of islands. The heights of the smaller islands (QDs), which have a density of $3.0 \times 10^2 \mu\text{m}^{-2}$, are distributed as shown in Figure 2.12(a), based on a sample size of 308 dots. The mean and standard deviation of the height of the dots are 7.5 ± 0.1 nm and 1.6 nm, respectively. There are also seven slightly larger islands present in the image. An analysis of 37 of these larger islands, based on more extensive AFM measurements, yielded a mean height, standard deviation and density of 19.5 ± 0.5 nm, 3 nm and $0.3 \mu\text{m}^{-2}$. Bimodal size distributions are commonly found in this and other strained-island systems [20, 18, 41]. The QDs are believed to be self-limiting in size

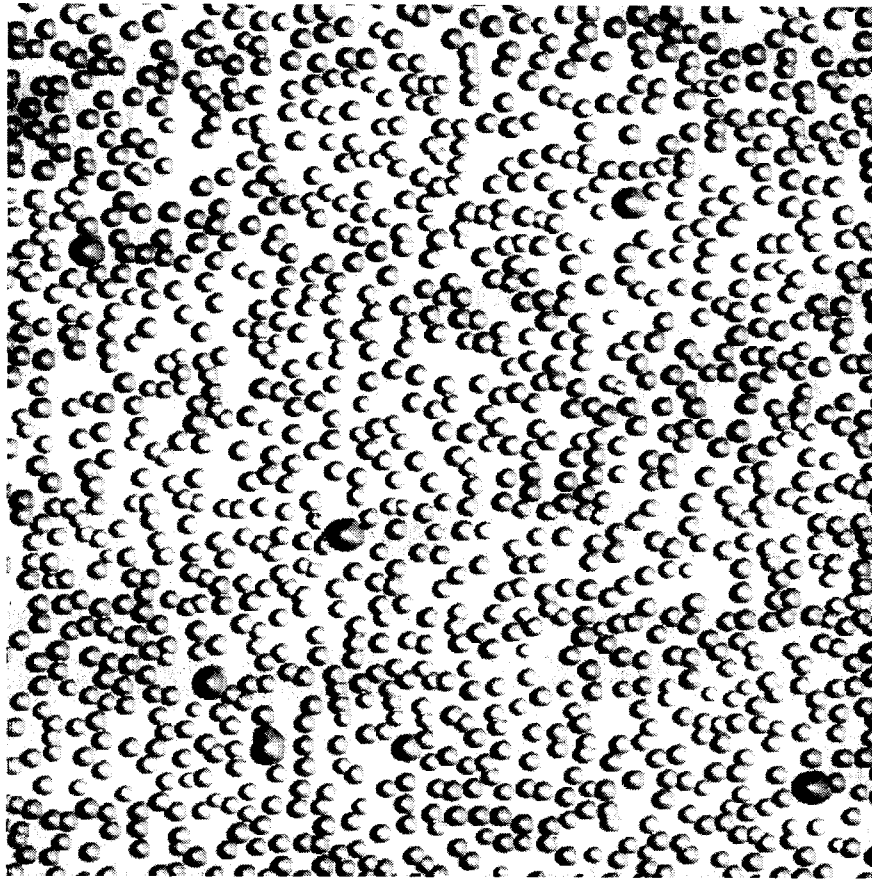


Figure 2.11: $2 \times 2 \mu\text{m}^2$ AFM image of the film in Fig. 2.10(b), showing the quantum dots and the large islands. The image has been digitally filtered to appear as if illuminated from the right.

whereas the larger islands are found to grow during prolonged annealing, possibly due to the incorporation of a defect such as a dislocation, which removes the self-limiting constraint [20].

The 2D isotropic power spectrum obtained from the Fourier transform of a $10 \times 10 \mu\text{m}^2$ image of the film in Fig. 2.11, is plotted in Figure 2.13 (curve *a*). For comparison purposes we also show the PSD of a GaAs buffer layer [Fig. 2.13, curve *b*]. This was obtained

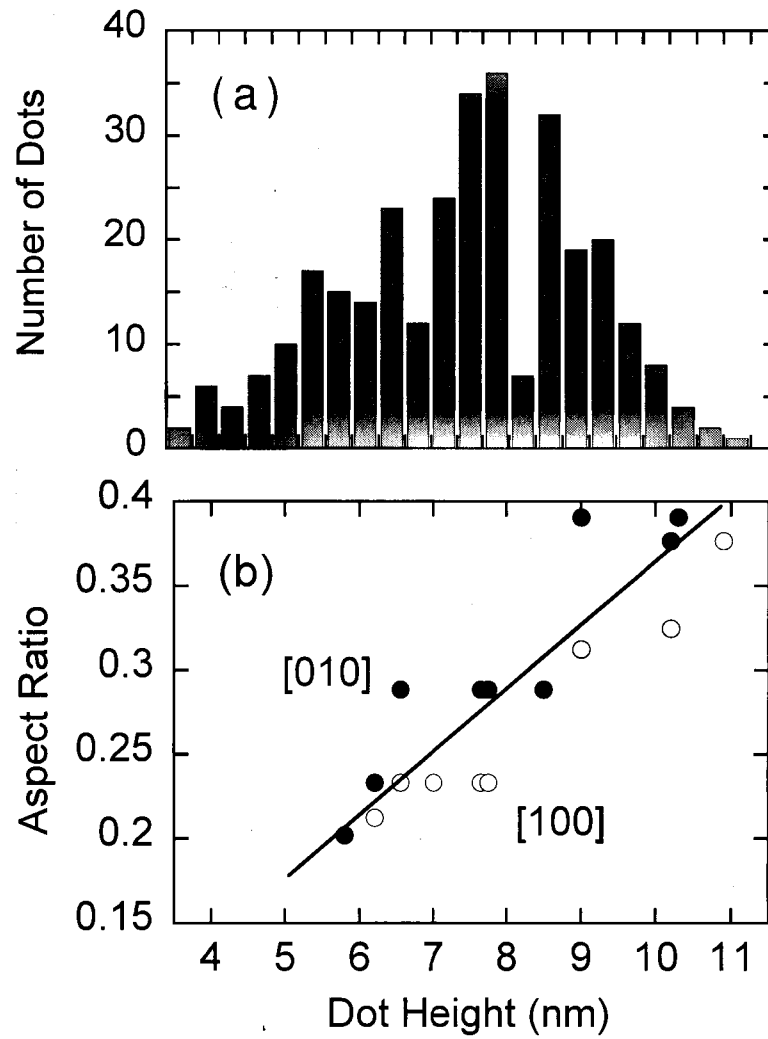


Figure 2.12: (a) Quantum dot height distribution and (b) inferred aspect ratio of the dots based on simulated AFM profiles as shown in Fig. 2.14.

by performing an isotropic average of the 2D PSD calculated from the AFM image in Fig. 2.10(a). The substrate preparation and growth conditions for this buffer layer were the same as those used for the buffer layers in the quantum dot growth experiments. We note that the atomic steps are well resolved in the image so that the PSD determined by AFM is expected to be accurate. The PSD of the GaAs buffer exhibits a power-law dependence on spatial frequency of approximately -3 . This is consistent with the q -dependence over the same spatial frequency range, of the PSD in Fig. 2.2 obtained from AFM measurements of another GaAs film in which the steps were resolved.

Due to the finite radius of the probe tip, AFM will not yield an accurate representation of the true PSD of surfaces that contain small, high aspect ratio features such as quantum dots. Specifically the AFM can resolve the height of the dots, but not their lateral dimension. In addition to reducing the roll-off frequency associated with the dot diameter, the AFM also exaggerates the dot volumes, which increases the magnitude of the PSD associated with the dots. Compared to capped dot structures, which are amenable to TEM and cross-sectional STM analysis, the shape of uncapped InAs quantum dots is normally inferred from AFM and RHEED measurements, and remains an outstanding issue in the literature [42, 43, 44].

Accordingly we have undertaken a study of the AFM images in order to estimate the true size of the dots in these films. The results of this analysis for two representative QDs and one large island, all from the film in Fig. 2.11, are illustrated in Figure 2.14, where we show AFM dot profiles acquired along the slow scan axis, approximately parallel with

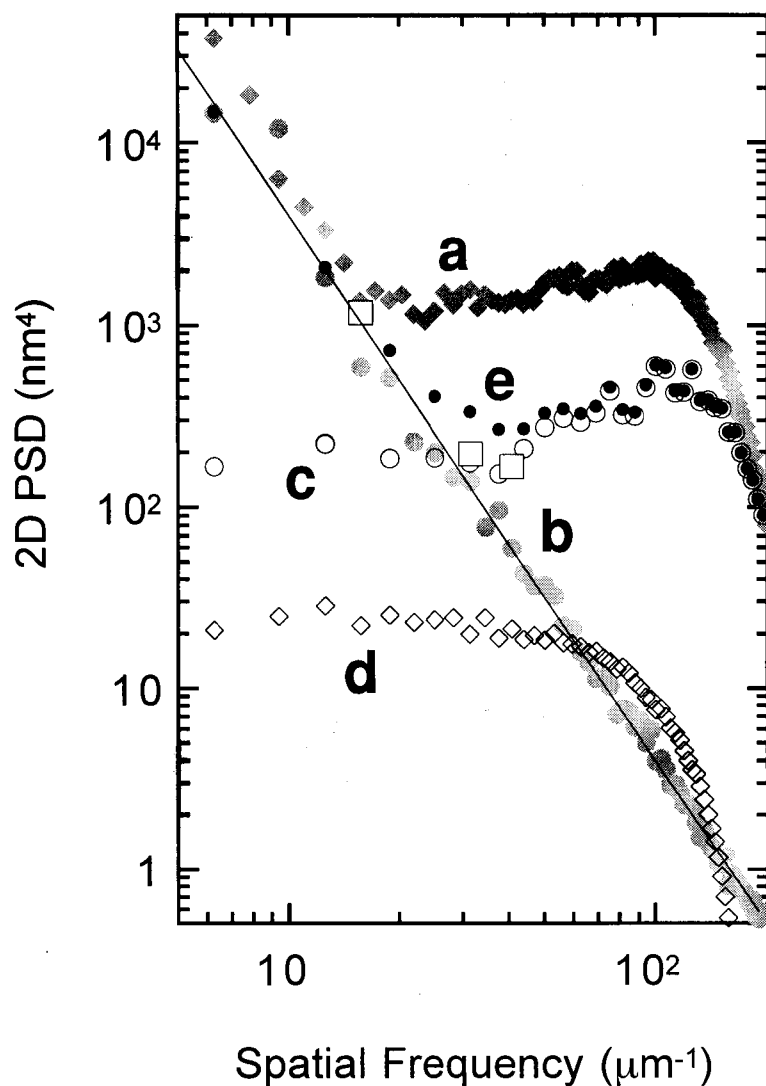


Figure 2.13: Estimation of the 2D PSD for the film in Fig. 2.11, based on post-growth AFM. (a) Gray diamonds, PSD computed directly from a $10 \times 10 \mu\text{m}^2$ image of the film. (b) Gray circles, PSD of the bare buffer layer in Fig. 2.10(a). The solid line has a slope of -3. (c) Open circles, PSD for a simulated QD distribution, in which each dot in Fig. 2.10(b) was replaced with a cone as discussed in the text. (d) Open diamonds, PSD of the large island distribution obtained by replacing the 37 large islands in the image used to compute curve *a* with 1:2 aspect ratio cones. (e) Solid black circles, corrected version of the PSD in (a), obtained by adding curves (b), (c) and (d). The three open squares are an independent estimate of the PSD based on *in situ* light scattering measurements.

the [010] crystal direction. Consistent with the observation from AFM that the dots are isotropic, we have modeled each dot as a cone, whose cross-section is shown in Fig. 2.14. The radius of the AFM probe tip (assumed to be spherical) and the aspect ratio of each dot were fitting parameters. The simulated profile produced with a 30 nm radius probe tip (solid line) is found to be in excellent agreement with the actual AFM profile (open circles) in all three cases. Although it was necessary to truncate some of the cones slightly in order to optimize the fits, the effect of the truncation on the inferred dot volume was found to be small (less than 6% larger than the corresponding non-truncated cone). We regard these fits as a reliable indicator of the actual tip radius. The manufacturer does not specify a typical tip radius, but indicates it is larger than 10 nm.

These results and the results of similarly good fits obtained for QD profiles along [100], with the same 30 nm tip radius, are summarized in Figure 2.12(b). We note that the QD aspect ratio increases with dot height, which is consistent with a recent AFM study of InAs dots [43]. The smallest dots had aspect ratios corresponding to a $\sim 22^\circ$ side inclination as shown in Fig. 7(a), which is close to the facet angle (25°) of the $\langle 100 \rangle$ profiles of a $\{316\}$ faceted pyramid. The presence of these facets has been proposed to explain chevrons observed in RHEED patterns from InAs dots [42], which we have also observed in our own QD growth experiments. Thus it is likely that the low aspect ratio dots include $\{316\}$ facets. There is a systematic difference in the aspect ratios along the two orthogonal $\langle 100 \rangle$ directions in Fig. 2.12(b), which may reflect a real anisotropy in the dot shape, or it could be an artifact of the scanning process. We

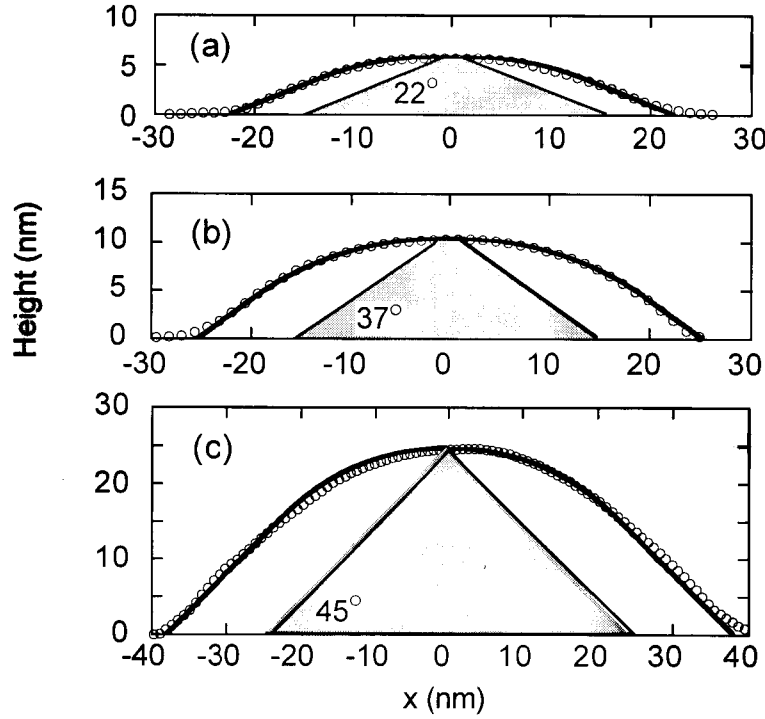


Figure 2.14: Comparison of three simulated AFM scan profiles (solid line) with actual AFM measurements from Fig. 2.10 (open circles), for two QDs having heights of (a) 5.8 nm, (b) 10.3 nm, and one large island of height 24.6 nm (c).

did not investigate this effect further. The true QD shape is almost certainly a faceted structure, with an aspect ratio that changes in discrete steps, as different facets become energetically favored. However, for the purposes of determining the dot volumes, each dot was assumed to be a symmetrical cone with an effective aspect ratio given by the linear fit in Fig. 2.12(b). We have also examined six of the large islands, and find that the aspect ratio is approximately 0.5 in all cases [Fig. 2.14(c)]. In Chapter 5 it is shown that these islands continue to grow during prolonged annealing, however the aspect ratio remains approximately constant. This indicates that the side inclination limits at 45° ,

which would correspond to a pyramidal structure incorporating $\{110\}$ facets.

In accordance with the above results, we have calculated a corrected PSD for the distribution of QDs in Fig. 2.10(b), obtained after each dot has been replaced by a symmetrical cone whose aspect ratio is determined from the linear fit in Fig. 2.12(b). To estimate the effect of the large islands, we performed the same procedure for the large island distribution in the AFM image used to calculate curve *a* in Fig. 2.13, after first removing the QDs. Consistent with the discussion above the aspect ratio was taken to be 0.5 for all the large islands. In order to correct for the difference between the density of large islands ($0.37 \mu\text{m}^{-2}$) in the AFM image and the average density ($0.3 \mu\text{m}^{-2}$) determined from many images, the PSD was multiplied by a factor $3/3.7 = 0.81$. This is justified if the spatial distribution of the large islands is approximately random, as discussed below.

Based on the analysis above, the PSD of the QD distribution and the large island distribution are given by curves *c* and *d* respectively in Fig. 2.13. The high-*q* roll-off in both cases is due to the finite island diameters. The large island PSD is approximately an order of magnitude or more lower than that of the QD distribution, over the spatial-frequency range accessible to the AFM measurement. Thus the total island PSD (not shown) is essentially indistinguishable from curve *c* in this plot. The total island PSD can be estimated by adding curves *c* and *d* together, if correlations between the spatial distributions of the two populations are not important, which we feel is the case based on inspection of the AFM images. This sum is added to the PSD of the buffer layer (curve

b) to obtain an estimate of the PSD of the total surface (curve *e*), which again neglects any correlations. One source of correlation between the substrate structure and the dot location is dot alignment along step edges, however AFM images show that this is not an important effect in our films.

Although *ex situ* light scattering measurements are not available for the film in Fig. 2.11, we can make an independent estimate of the PSD using the *in situ* light scattering data obtained during the growth of this film. These measurements are discussed in Chapter 5 and the results for three spatial frequencies (16, 31, and $41 \mu\text{m}^{-1}$) are presented in Figure 5.3, normalized in each case to the initial scattering from the buffer layer. The scattering geometry for the *in situ* measurements was such that the measurements are sensitive to roughness aligned approximately along a $\langle 100 \rangle$ direction. This is midway between the $\langle 110 \rangle$ directions associated with the slight buffer layer anisotropy. We therefore take the isotropic average of the PSD of the GaAs buffer to be a reasonable approximation to the PSD of the starting surface along the direction monitored by light scattering. The final scattering signal in Fig. 5.3 at each spatial frequency is multiplied by the corresponding value of the buffer layer PSD in Fig. 2.13 (straight line fit to curve b) to obtain an estimate of the final PSD. The results (open squares) agree reasonably well with the corrected PSD obtained from the AFM analysis (curve *e*), indicating that the correction procedure is valid. By contrast the agreement with the uncorrected AFM data is poor. The fact that the normalized light scattering signals need only be multiplied by the PSD of the GaAs buffer to obtain the correct magnitude of the final PSD, further

suggests that background scattering in the chamber was below the level of the scattering signal from the wafer.

The results above can be understood by considering that the Fourier transform of a distribution of identical islands is the product of the transforms of the individual island shape, and an array of unit-volume δ -functions that maps the island distribution. At spatial frequencies below the roll-off frequency associated with the island diameter, the magnitude of the island shape transform approaches the island volume, V . Thus the PSD at the spatial frequencies of interest is proportional to the square of the island volume. Furthermore the PSD of an array of unit-volume δ -functions whose spatial distribution is random, is simply equal to the areal density n of the δ -functions. The 2D PSD for a spatially random distribution of islands may then be written as

$$g_{2D}(n, V) = n\langle V^2 \rangle \quad (2.10)$$

where the angular brackets $\langle \rangle$ denote an average over the island size distribution. By a spatially random distribution of islands we mean that the positions of the islands are uncorrelated, so that the PSD is independent of q in accordance with Eq. 2.10, for spatial frequencies below the roll-off frequency associated with the island diameter.

Assuming conical islands (aspect ratio = 0.5) the PSD of the large island distribution should be 25 nm^4 (for any q below the roll-off due to the island shape) based on Eq. 2.10 and the measured height distributions from AFM. This is in excellent agreement with the PSD obtained from the measured spatial distribution of the large islands (curve d in Fig. 2.13). The PSD is independent of q (below the high q roll-off) consistent with the

fact that the large islands appear to be randomly distributed. By comparison the PSD for the QDs (curve *c* of Fig. 2.13) has a slight q -dependence which reflects the fact that the quantum dot positions are not completely uncorrelated, as they would be in the case of a truly random distribution. The PSD obtained using Eq. 2.10 for the QD distribution is 734 nm^4 , which agrees reasonably well with the measured PSD for spatial frequencies near $q \sim 100 \mu\text{m}^{-1}$. This spatial frequency corresponds to a length scale of $\sim 63 \text{ nm}$ which is close to the average dot spacing, $L_{avg} = n^{-1/2} = 58 \text{ nm}$.

Chapter 3

Real-Time Light Scattering Setup

The results of Chapter 2 demonstrate that light scattering can be used to obtain quantitative surface morphology information that is consistent with AFM. A major advantage of light scattering compared to AFM is its straightforward implementation for real-time monitoring. In this chapter we discuss the experimental setups used to obtain the *in situ* light scattering data presented in Chapters 4 and 5.

3.1 Optical Port Configurations and Detection Technique

The real-time light scattering experiments were performed in the VG-V80H MBE deposition system described earlier. Optical access to the sample is achieved through windows positioned at vacant ports on the MBE growth chamber. The port geometry is shown schematically in Figure 3.1. The centre port *C* (an optical pyrometer port), the surrounding effusion cell ports (e.g. port *G*), and the mass spectrometer shutter port *H* all have line-of-sight access to the sample. The effusion cell shutter ports (e.g. port *F*) do not face the sample, and in this case optical access is achieved with mirrors as shown in

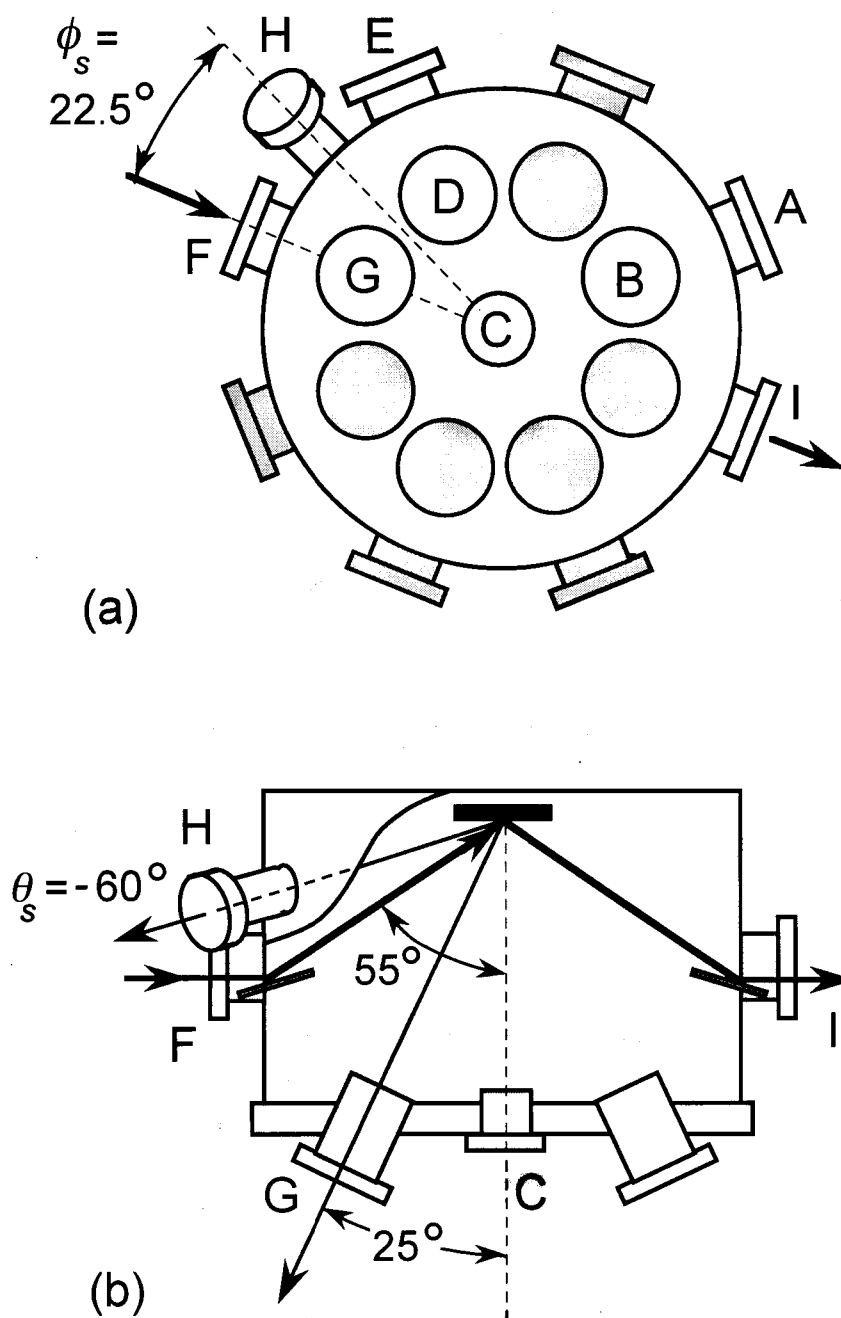


Figure 3.1: (a) Plan view of MBE growth flange showing optical port configuration, and (b) cross-sectional view in the plane of incidence showing detection geometry for the ultra-violet light scattering measurements.

λ (nm)	input port	θ_i ($^\circ$)	output port	θ_s ($^\circ$)	ϕ_s ($^\circ$)	q_x (μm^{-1})	q_y (μm^{-1})	$ q $ (μm^{-1})
488	C	0	B	-25	0	5.4	0	5.4
			D	-25	0	0	5.4	5.4
			A	-55	0	10.5	0	10.5
			E	-55	0	0	10.5	10.5
250	F	55	G	-25	0	31	0	31
			H	-65	22.5	40	8.2	41

Table 3.1: Spatial frequencies probed at each detector port, for visible and ultraviolet light scattering measurements.

Fig. 3.1(b). The geometry is such that the normal of each mirror makes an angle of 74° with respect to the optical axis of the light beam.

Two different port configurations were used to obtain the *in situ* scattering results presented in this thesis. The port designations and spatial frequencies accessible for each configuration are listed in Table 3.1. In one geometry, visible laser light ($\lambda = 488$ nm) is incident normal to the sample through the center port *C*, and detected simultaneously in two orthogonal planes, at ports *A*, *B*, *D* and *E*. This arrangement was used to study the anisotropic 1D roughness that develops during InGaAs growth on GaAs (Chapter 4). In another configuration ultraviolet light from a mercury lamp ($\lambda = 250$ nm) is incident through port *F* and backscattered light is detected at ports *G* and *H*. This setup is designed to optimize access to high spatial frequency roughness, and was used to monitor the formation of InAs quantum dots (Chapter 5). Details of the visible and ultraviolet light scattering setups will be discussed separately, however a number of technical aspects are common to both setups as we now describe.

The surfaces in the MBE chamber become coated with arsenic during the deposition process, mainly due to reflection of the arsenic flux from the surface of the heated substrate. Windows with direct line of sight to the substrate are therefore particularly susceptible to coating. In the case of the visible light scattering experiments, optical access at ports *C*, *D* and *B* is obtained via 45° angle mirrors in the vacuum chamber (not shown in Fig. 3.1) so that there is no direct line of sight from the substrate to the window. The mirrors consist of 50 mm diameter GaAs wafers. The reduction in optical throughput associated with the coating of the mirrors is comparatively minor. Gradual coating of the mirrors and windows over the course of many growths is a problem, which is solved by periodically removing and cleaning these optical elements. In the case of the ultraviolet light scattering setup shown in Fig. 3.1(b), the input port *F* and the two detection ports *H* and *G* are all fitted with heatable viewports, which allow the arsenic deposit to be removed periodically by heating to over 500 °C, or which can be maintained at ~ 300 °C during growth to prevent coating from occurring.

In terms of surface finish, the films of interest in this work are comparable to high quality optical mirrors, exhibiting typically 1 nm RMS roughness over $10 \times 10 \mu\text{m}^2$ areas according to AFM. By contrast the other surfaces in the MBE growth chamber are coated with arsenic oxide, and scatter light very effectively. The oxide develops during venting of the growth chamber when the arsenic-coated surfaces are exposed to air. The sample when viewed at a non-specular angle is therefore by far the blackest object in the growth chamber. The goal of the *in situ* measurements is to monitor changes in the non-specular

scattering intensity from this nearly specular surface during growth. The ability of light scattering to detect this level of roughness has been established in Chapter 2. The main experimental problem is therefore not detecting the scattered light from the sample, but rather minimizing the stray background light that scatters into the solid angle of the detector.

In these experiments, the illumination area of the probe beam is positioned approximately at the center of the quarter wafer sample inside the growth chamber. In order to minimize background arising from scattering of the specular beam from the chamber walls, the specularly reflected light is diverted out of the growth chamber through a viewport at the specular position. Each detector is equipped with an optical line filter matched to the incident beam wavelength, to reduce background from ambient light in the chamber associated with ion gauges and the DRS temperature measurement. Since these sources also emit optical power within the 10 nm filter pass band, the input beam is mechanically chopped at ~ 400 Hz, and phase-locked detection electronics are used. The signal is maximized using a lens to collect the light that scatters into the solid angle of the output window. This also has the effect of averaging out the speckle noise in the scattered light distribution. The collected light is focused onto the detector and a mask in the focal plane of the lens ensures that only light scattered from the central part of the substrate reaches the detector.

3.2 Visible Light Scattering

The *in situ* measurements presented in Chapter 4 were obtained using an air-cooled argon ion laser tuned to the 488 nm line with an output power of 15 mW [34, 45]. The light was incident normal to the surface of the substrate through port *C*, and the diffusely scattered light was detected simultaneously in two orthogonal planes as described above. As discussed in Section 2.3.5, scattering associated with the surface crosshatch pattern in strain-relaxed InGaAs films is confined to two orthogonal planes aligned with the $\langle 110 \rangle$ crystal directions. In order to detect this scattering during growth, the sample was carefully aligned at the beginning of the experiment so that the two orthogonal detection planes coincided with the planes containing the $[110]$ and $[1\bar{1}0]$ directions of the sample. This was done using the cleaved edges of the quarter-wafer substrates as direction references. In this way roughening in both $\langle 110 \rangle$ crystal directions can be simultaneously detected at spatial frequencies q of $5.4 \mu\text{m}^{-1}$ and $10.5 \mu\text{m}^{-1}$, corresponding to lateral length scales of $1.2 \mu\text{m}$ and 600 nm respectively.

The spot size of the laser on the surface of the wafer was about 2 mm in diameter. The location of the beam spot on the substrate was selected to avoid visible surface defects but was not subsequently moved during film growth. The diffusely scattered light was collected with a 60 mm diameter lens, passed through a laser line filter and detected with a silicon pin diode and lock-in detection system.

In Chapter 4 the relative magnitudes of the scattering signals detected at different optical ports will be compared. In order to simplify the comparison of signals in the

detector port	d (mm)	r (mm)	γ ($^\circ$)	$\Delta\Omega$ (str $\times 10^{-3}$)	$\Delta\theta_s$ (rad)
A, E	240	25	74	9.4	0.18
B, D	600	25	45	3.9	0.19
G	295	10	90	3.6	0.21
H	407	10	90	1.9	0.15

Table 3.2: Acceptance angles for detector ports used in visible and ultraviolet light scattering experiments.

orthogonal detection planes, the polarization of the incident light was oriented at 45° relative to the $\langle 110 \rangle$ scattering directions. This ensures that the polarization-dependent factor Q in Eq. 2.5 is the same for detection in both planes. In order to compare the magnitudes of signals obtained at different ports it will be useful to know the acceptance angle in the plane of incidence, $\Delta\theta_s$ and solid angle $\Delta\Omega$ associated with each port. These are given by $\pi r^2 \cos \gamma / d^2$ and $2\pi r \cos \gamma / d$ respectively, where r is the radius of the limiting aperture and d is its distance from the sample. The limiting aperture for these measurements is the output mirror, which makes an angle γ with the output beam. The acceptance angles for each port are shown in Table 3.2.

Some of the measurements in Chapter 4 were made at a spatial frequency of $16 \mu\text{m}^{-1}$, corresponding to a lateral length scale of 393 nm. These measurements were made using a modified geometry in which the light is incident through port B and backscattered light is detected at port A . Roughening in only one direction can be monitored in this way, however access to higher spatial frequency information is achieved.

3.3 Ultra-Violet Light Scattering

The analysis in Section 2.3.6 indicates that the PSD associated with an array of InAs quantum dots does not rise above that of the buffer layer for spatial frequencies less than $\sim 25 \mu\text{m}^{-1}$. This makes the real-time observation of quantum dot formation in this materials system impractical using visible light sources of reasonable intensity. Accordingly an ultra-violet light scattering (UVLS) apparatus has been designed, which uses the 250 nm line of a Hg arc lamp as the light source.

3.3.1 Light Source

A schematic of the UVLS light source is shown in Figure 3.2. The objective of this design is to deliver an intense beam of single-wavelength ultraviolet radiation to a spot contained entirely within the area of the sample. The sample consists of a 25 mm radius quarter circle wafer oriented with its surface normal at 55° to the incident beam, as shown in Fig. 3.1(b). The optical path length from the input window F to the sample is 353 mm. The choice of wavelengths is restricted largely by the availability of UV-transmitting viewports that can withstand the 200°C bake-out procedure needed to recover UHV conditions after a system vent. The only commercially available viewports meeting this specification use sapphire windows, for which the transmissivity rolls off sharply below 200 nm. Another consideration is the reflectivity of the GaAs substrate material which peaks at approximately 250 nm [46]. An inexpensive source of intense radiation at this wavelength is the 250 nm line of a mercury arc lamp.

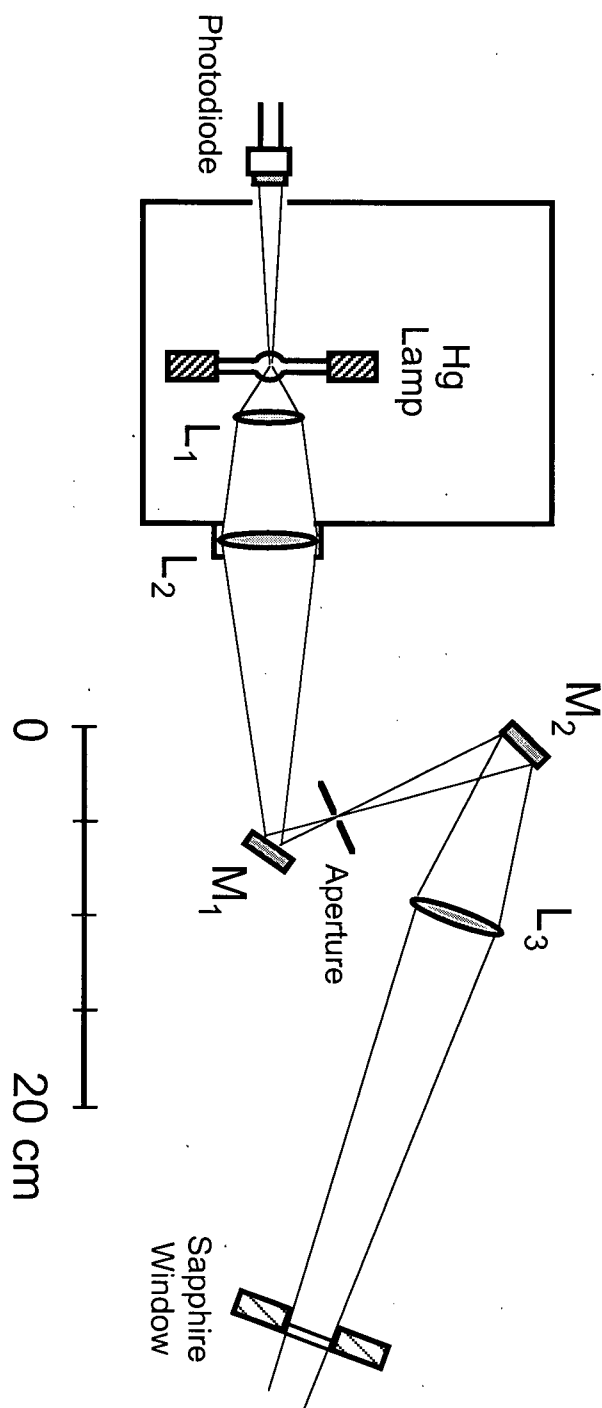


Figure 3.2: Schematic of UV light source. The lens focal lengths and distance of each optical element from the arc lamp is shown in Table 3.3.

optical element	f (mm)	D (mm)	d (mm)	throughput
L_1	50	32	26	0.9
L_2	100	46	91	0.9
M_1	-	25	261	0.9
aperture	-	2	276	1
M_2	-	25	396	0.9
L_3	150	50	486	0.9
window	-	25	716	0.7

Table 3.3: Optical path length d from each optical element to the lamp as shown in Fig. 3.2. Also specified are the lens focal lengths f , and the effective diameter D and optical throughput of each element.

In contrast to a collimated laser beam, light from an arc lamp is non-directional. UV optics are therefore used to collect this light and focus it onto the sample. The three lenses shown in Fig. 3.2 are UV grade quartz. The distance of each lens from the arc lamp is given in Table 3.3 along with its visible focal length (the focal lengths at 250 nm will be somewhat shorter). The two mirrors are 25 mm in diameter and have 90% reflectance at 250 nm. A commercially available 100 W Hg arc lamp was chosen for which the arc size is $\sim 0.3 \times 0.3 \text{ mm}^2$. The small arc size is necessary to compensate for the image magnification associated with the long focal distance to the sample. Due to shadowing effects from the electrodes, output from the arc is emitted mainly within an angular range of $\pm 45^\circ$ with respect to the horizontal plane normal to the lamp axis. Accounting for this, the first lens L_1 captures approximately 13% of the total lamp output. All of the 250 nm component of this light is focused by L_2 onto the aperture A . This aperture is positioned so that only the image of the arc itself is transmitted. The light from this

aperture falls completely within the solid angle of lens L_3 , which is positioned such that a clean $\sim 50 \text{ mm}^2$ image of the illuminated aperture is formed on the sample.

Although the optical output of this light source has not been measured, we can obtain a rough estimate as follows. Based on the spectral irradiance data of the Hg lamp, the total optical power at 250 nm within the 10 nm passband of the detection system is approximately 1 W. Multiplying this by the collection efficiency (limited by the solid angle of the first lens) and allowing for a 10% power reduction at each UV optical element in the system (3 lenses and 2 mirrors), we estimate that the 250 nm output of this source is about 70 mW. This is about 50% larger than the output specified for a commercially available source [47] using the same arc lamp and a lens system of similar f number, however we have neglected losses associated with imperfect optical alignment and aberrations from the spherical lenses. In addition to the sapphire window, the heatable viewport used to couple the light into the growth chamber contains a quartz heating element. The transmission of each of these is roughly 0.7. Allowing a 50% loss on reflection from the GaAs mirror inside the chamber, we estimate that up to 18 mW of 250 nm radiation is incident on the sample. The actual power might be 2 or 3 times lower, depending on alignment and the operating conditions of the lamp.

The output power from the arc lamp drops during operation as the temperature within the air-cooled lamp housing increases. The drift in output power, which is typically a factor of about two during an MBE run, is monitored using a silicon photodiode detector with a 250 nm line filter and positioned behind the lamp as shown in Fig. 3.2. The

light scattering data obtained with this lamp have all been normalized to the monitored output power.

The UV lamp housing and the optical components that make up the light source are all mounted on an optical breadboard. The breadboard is bolted to another plate to form an L-shaped bracket. This plate is secured directly to the input port of the growth chamber using 1/4 inch stainless steel bolts, such that the axis of the Hg arc lamp is oriented vertically.

3.3.2 Detectors and Viewports

The detection geometry is shown in Fig. 3.1. This configuration is sensitive to roughness at spatial frequencies of $31 \mu\text{m}^{-1}$ and $41 \mu\text{m}^{-1}$ as shown in Table 3.1. Note that one of the two detection ports (port H) is positioned 22.5° out of the plane of incidence, so that the spatial frequency detected at this port will have a small y -component according to Eq. 2.6. This setup was used to monitor the growth of quantum dots, for which the roughness is isotropic. In this case only the magnitude of q is important. To ensure consistency between runs, the sample was always oriented so that the plane of incidence coincided with a $\langle 100 \rangle$ direction in the surface.

In addition to the UV light, 10 mW of s -polarized 488 nm light from the Ar ion laser beam was coupled into the chamber through the same viewport as the Hg arc lamp beam. This was achieved by placing a small mirror between the lens L_3 shown in Fig. 3.2 and the input window. The mirror was positioned near the edge of the light cone associated with

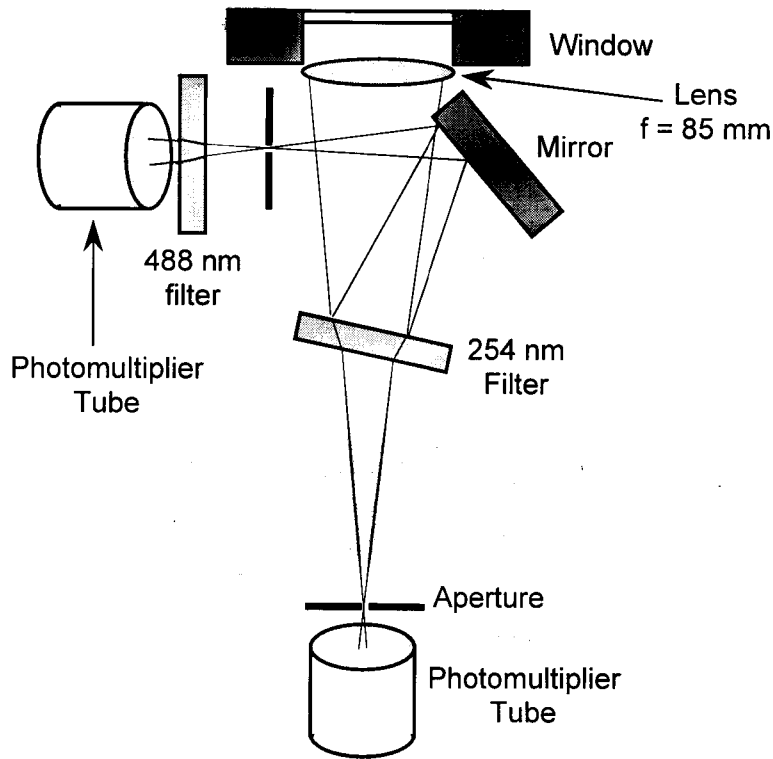


Figure 3.3: Schematic of detector arrangement at port *G*.

the focused UV light, so that reduction of the 250 nm throughput was negligible. The scattered 488 nm light was detected with another photomultiplier tube positioned at port *G*, thus permitting access to $16 \mu\text{m}^{-1}$ roughness. The detector arrangement at this port is shown in Fig. 3.3. Here the filter for the UV detector was oriented at an angle of 12° from the optical axis to divert the 488 nm radiation into the second detector. The 12° rotation shifts the center frequency of the filter by about 1%. A 254 nm filter was used, rather than 250 nm, which compensates for this effect. Since the UV interference filter is an excellent reflector at 488 nm ($R > 0.9$), this setup permits the simultaneous measurement of both wavelengths without sacrificing the intensity of either signal. Including the UV

scattering signal measured at port *I*, three different spatial frequencies corresponding to roughness on length scales of 154 nm (port *I*), 205 nm (port *G*), and 393 nm (port *G*) could be monitored simultaneously throughout the growth experiments.

As mentioned above, optical access to the sample at the center of the MBE growth chamber was through heatable viewports with 25 mm diameter sapphire windows. These viewports contain an internal UV-grade quartz window, which could be cleaned by heating to 500 °C after each MBE run. Arsenic deposits that accumulated on the windows at the detector positions during a single growth were invisible to the eye and generally had no significant effect on the scattering signal, although during extended MBE runs coating of port *G* was noticeable for the UV light. Coating of the input window by contrast was dramatically enhanced over the input beam area. This window was therefore kept heated to 300 °C throughout growth, which prevented any deposits from forming. Although we do not know the precise mechanism for the light-assisted window coating, *ex situ* AFM analysis of the substrates did not show any significant effect of the light on the film growth. We note also that adlayer photolysis has been observed using 248 nm laser light during growth of InAs quantum dots [48], however much higher intensities (45 W/cm²) were used.

The solid angle associated with each detector port is given in Table 3.2. The small solid angle for port *H* is due to the much smaller window area of the heatable viewports as compared to the 60 mm windows used for the visible light scattering setup discussed in Section 3.2. In the case of port *G*, this is compensated by the closer proximity of

the window to the sample made possible by the elimination of the 45° angle internal mirror required in the previous setup. A 25 mm diameter UV quartz lens was used to collect the light at each detector port, and this was spatially filtered to minimize the detection of light scattered from the edges of the sample. In this case it was not possible to move the illumination spot of the UV light on the sample to avoid particles, however growth experiments were not performed on wafers that contained particulate contamination within the area illuminated by the probe beam.

3.3.3 Alignment and Calibration

The initial optical alignment was accomplished using the visible broad band output that accompanies the atomic emission lines of the Hg lamp. The intense visible output was then blocked with a 250 nm line filter so that alignment for the UV light could be optimized. Although the 250 nm light is not visible, its path through the optical system is easily traced by observing the fluorescence it produces on a slip of paper. In order to observe the focused spot at the sample position, an empty sample holder was loaded into the growth chamber. The holders are fitted with pyrolytic boron nitride (PBN) diffuser plates, which are positioned behind the sample in order produce more uniform heating of the radiatively heated substrates [33]. The PBN material also produces visible fluorescence under illumination of UV light. The empty sample holder was rotated into the growth position, so that the 488 nm laser beam was incident at the center of the holder. Once the UV spot had been carefully focused, it was repositioned on the PBN

to coincide with the visible laser spot, using the mirror M_2 . At this stage the detectors at the two output ports could also be aligned using the strong scattering signal from the PBN. In the case of the UV detectors the alignment was accomplished by monitoring the scattering signal displayed on an illuminated digital read-out. The sample could then be loaded into the growth chamber and positioned with reference to the laser beam spot so that the detector alignment was preserved. The alignment could be checked during the growth experiment by noting the magnitude of the peak intensity associated with the oxide desorption, which normally varied by less than a factor of three between runs. In cases where realignment was required, this was done using the strong scattering signal from the oxide-desorbed surface.

In order to obtain an estimate of the absolute roughness of the growth surface in real-time, and not just changes in its relative value during growth, an absolute calibration of the optical throughput of the system was performed. This was achieved by replacing the sample with a Lambertian scattering surface consisting of a BaSO_4 -coated aluminum plate, and measuring the UV scattering signals (normalized to the monitored lamp power) at both detector positions. For a perfectly reflecting Lambertian scatterer, the intensity of light scattered at an angle θ_s into the differential solid angle $d\Omega$ is proportional to $\cos \theta_s$. In terms of the quantities in Eq. 2.5,

$$P d\Omega = \frac{\pi}{\cos \theta_s} dP. \quad (3.1)$$

This equation can therefore be used to replace the unknown quantity $P d\Omega$ in Eq. 2.5, with the scattering signal dP measured for the Lambertian surface. Note that as long

as the same detector and lamp power settings are used during subsequent growths, only the relative value of dP is important. It is therefore not necessary to know the absolute sensitivity of the detectors or the optical throughput of the system in order to calculate the PSD from the detected scattering signal. The quantity Q in Eq. 2.5 relevant to this scattering geometry is calculated in Appendix A.

Based on this absolute calibration, the sensitivity of the scattering signal at $41\ \mu\text{m}^{-1}$ was found to be $\sim 1\ \text{nm}^4$. Using Eq. 2.10, we find this is sufficient for example to detect quantum dot densities as low as $1\ \mu\text{m}^{-2}$, for 8 nm high dots.

Chapter 4

Misfit Dislocations and Surface Crosshatch

In this chapter we develop an analytical model for the surface roughening that can occur during film growth when a small lattice mismatch, or misfit, exists between the epilayer and the substrate, such that the epilayer is in compression (see Fig. 1.1). When the film thickness is small, the compressive stress is accommodated by elastic deformation of the epilayer lattice, while preserving the coherent registry of the epilayer with the substrate across the interface [Fig. 1.1(a)]. As growth proceeds however, a critical thickness is exceeded and it becomes energetically favorable to relax a portion of the strain inelastically, through the introduction of misfit dislocations at the substrate/epilayer interface [Fig. 1.1(b)]. In addition to reducing the misfit strain, the dislocations also produce a nonuniform strain distribution in the film, resulting in a nonuniform chemical potential at the surface. Continued growth results in surface roughening as adatoms diffuse in response to the chemical potential gradients set up by the interfacial dislocations

[Fig. 1.2(a)]. In particular we will show that this effect can account for the emergence of the surface crosshatch pattern during growth of strained InGaAs on GaAs.

The theoretical basis for this model is similar to that of a model proposed recently by Jondottir and Freund [10]. In that work, a numerical simulation was performed to obtain the equilibrium surface profile of a strained film of fixed thickness, assuming a pre-existing, static dislocation array. No transient effects were studied, and no comparison with experimental results were made. By contrast, the present calculation provides an analytical solution to the time-dependence of the surface morphology, for the more relevant case of a growing film that relaxes continuously during growth. We demonstrate quantitative agreement of this model with experimental measurements of the surface roughness during growth of strained InGaAs films.

4.1 Strain Relaxation in InGaAs on GaAs

4.1.1 Misfit Dislocations

A dislocation is characterized by a dislocation line and a Burgers vector [49]. An edge dislocation, which provides the most efficient relief of misfit strain, has its Burgers vector \vec{b} oriented perpendicular to the dislocation line. A dislocation in which \vec{b} and the dislocation line are parallel is called a screw dislocation, and cannot relieve misfit strain. The important dislocations in III-V semiconductor film relaxation are mixed dislocations that have both a screw and an edge component. An example of such a dislocation is shown in Figure 4.1. The ability of a mixed dislocation to relieve misfit strain is determined by

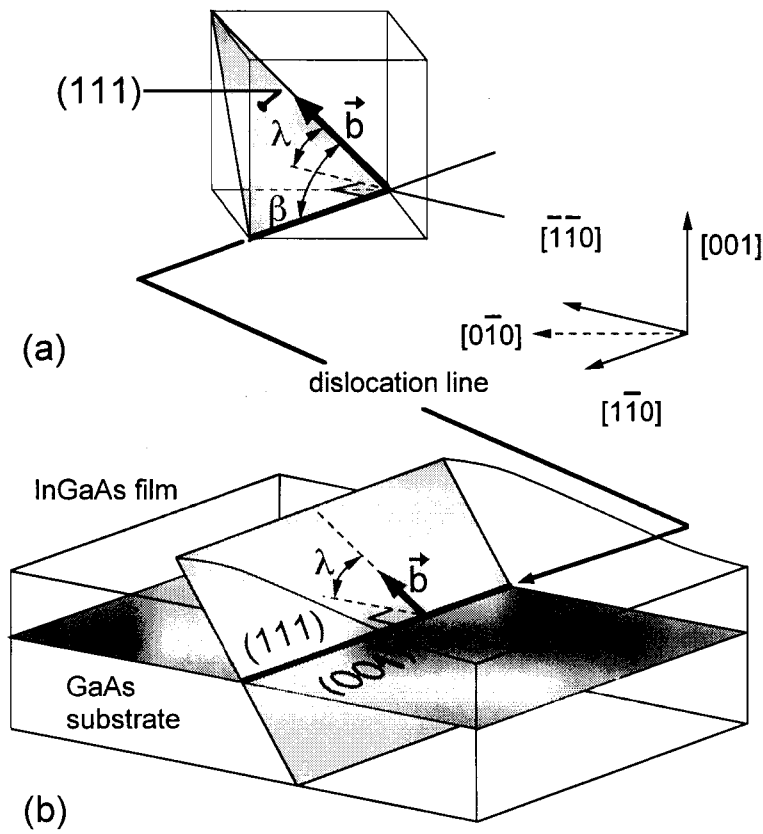


Figure 4.1: (a) 60° misfit dislocation aligned along the $[1\bar{1}0]$ direction, showing orientation of the Burgers vector \vec{b} which lies in the (111) slip plane. $\lambda = \beta = 60^\circ$. (b) The same dislocation at the (001) interface plane. Slip in the (111) plane associated with the dislocation produces an atomic-height step at the surface.

the magnitude of the edge component of \vec{b} within the plane of the interface, given by

$$b_{\text{edge},||} \equiv b \cos \lambda, \quad (4.1)$$

where λ is the angle between \vec{b} and the direction in the interface plane perpendicular to the dislocation line, as shown in Fig. 4.1(a).

If the dislocation is not already at the interface, it must be able to move there in order to be effective. Dislocation motion, or glide, normally occurs only in a plane containing

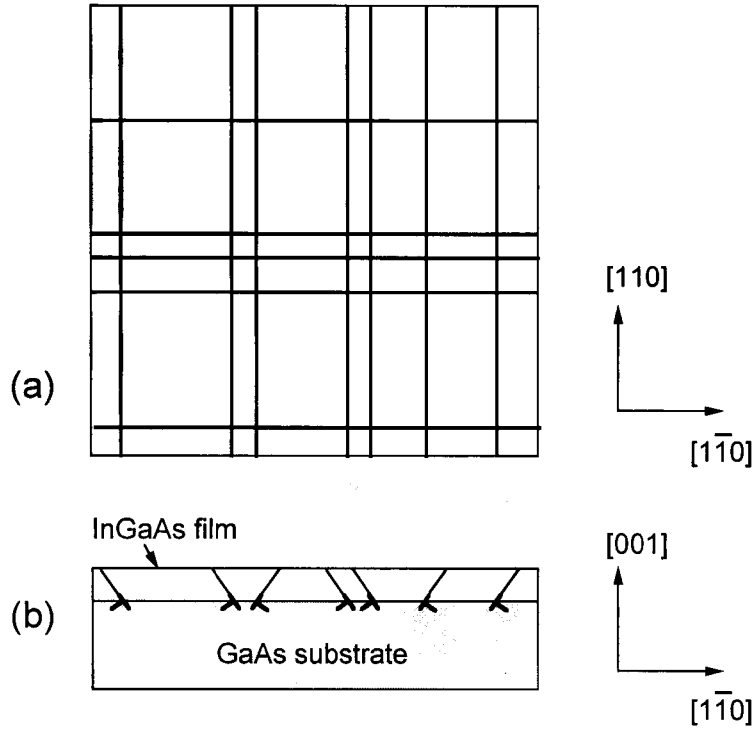


Figure 4.2: (a) Schematic plan view of the (001) interface between a strain-relaxed InGaAs film and a GaAs substrate, showing the $\langle 110 \rangle$ -oriented dislocation lines. (b) Cross section along the $[110]$ direction showing the interfacial dislocations and the associated slip planes.

both the dislocation line and the Burgers vector $[50]$. In particular, although it is efficient at relieving misfit strain, a pure edge dislocation with \vec{b} parallel to the interface cannot move easily to the interface. Glide occurs most readily within planes of high atomic density, known as slip planes. The slip planes in III-V semiconductor crystals are the $\{111\}$ planes, which are the close-packed planes of an fcc lattice.

The dislocations responsible for plastic strain relaxation in the $\text{In}_x\text{Ga}_{1-x}\text{As}/\text{GaAs}$ system, are mixed screw-edge dislocations known as 60° misfit dislocations [10]. The geometry of a 60° dislocation is shown in Figure 4.1. These dislocations have a Burgers

vector given by: $\vec{b} = a/2\langle 101 \rangle$, corresponding to a magnitude: $b = a/\sqrt{2}$, where a is the lattice constant. For films grown on (001)-oriented substrates, the dislocation lines lie along either the $[110]$ or $[1\bar{1}0]$ directions, corresponding to the intersection of the (001) interface plane with the $\{111\}$ slip planes. A cross-hatched dislocation array therefore develops during strain relaxation in this system, as illustrated schematically in Figure 4.2. The Burgers vector of the misfit dislocation associated with each dislocation line, lies in the $\{111\}$ plane and makes an angle β of 60° with the dislocation line, as shown in Fig. 4.1(a). For these dislocations, $\lambda = 60^\circ$, so according to Eq. 4.1, $b_{\text{edge},\parallel} = b/2$.

4.1.2 Critical Thickness for Dislocation Formation

The lattice mismatch f between an epilayer with equilibrium lattice constant a_{epi} and a substrate having a lattice constant a_{sub} is

$$f \equiv \frac{a_{\text{epi}} - a_{\text{sub}}}{a_{\text{sub}}}. \quad (4.2)$$

Before dislocations form, this mismatch is accommodated entirely by the elastic strain of the epilayer, which for positive mismatch is in compression. The introduction of a linear density ρ of interfacial misfit dislocations will reduce the average in-plane misfit strain, $\bar{\epsilon}_{\parallel}$ in the epilayer according to

$$\bar{\epsilon}_{\parallel} = f - \rho b_{\text{edge},\parallel} = f - \rho \frac{b}{2}, \quad (4.3)$$

where f is the initial misfit strain in the absence of dislocations, and the final expression applies to a 60° misfit dislocation. For the case of a crystal surface aligned with a cubic

symmetry direction, the corresponding strain $\bar{\epsilon}_\perp$ perpendicular to the interface is related to $\bar{\epsilon}_\parallel$ through Poisson's ratio ν ,

$$\bar{\epsilon}_\perp = \frac{-2\nu}{1-\nu} \bar{\epsilon}_\parallel. \quad (4.4)$$

Plastic strain relaxation can only proceed if the resulting reduction in elastic strain energy exceeds the energy cost of dislocation formation. The strain energy released for a given dislocation density is proportional to the thickness of the epilayer, whereas the energy required to add a dislocation to the interface increases only logarithmically with film thickness [50]. Hence a critical thickness exists beyond which dislocation formation is favored. This critical thickness z_c has been calculated by Matthews and Blakeslee [51, 52]:

$$z_c = \frac{b}{8\pi f \cos \lambda} \left(\frac{1 - \nu \cos^2 \beta}{1 + \nu} \right) \left[\ln \left(\frac{4z_c}{b} \right) + 1 \right]. \quad (4.5)$$

Once the critical thickness for the initial lattice mismatch f has been exceeded, dislocations will form reducing the in-plane strain in the epilayer according to Eq. 4.3. Thus a new effective mismatch exists, equal to $\bar{\epsilon}_\parallel$. If the film is in mechanical equilibrium, it will always be at the critical thickness corresponding to the residual strain in the epilayer. Neglecting the logarithmic dependence in Eq. 4.5, the residual strain for thicknesses z above the initial critical thickness z_c will then be given by

$$\bar{\epsilon}_\parallel(z) = \frac{f z_c}{z}, \quad z > z_c. \quad (4.6)$$

Equation 4.6 indicates that the strain in the film will vary inversely with film thickness above z_c . This behavior has been observed experimentally [53, 54], however the observed

critical thickness is considerably higher than the value given by Eq. 4.5. This has been attributed to the lack of dislocation sources present in the film, owing to the high crystalline perfection of the substrate. Dislocation multiplication mechanisms, which are expected to act at film thicknesses on the order of four times the Matthews-Blakeslee critical thickness [55], are necessary so that substantial film relaxation can occur. Furthermore, kinetic constraints on the formation of dislocations will cause the residual strain in the growing film to be higher than the equilibrium strain. These effects are discussed further below.

4.1.3 Strain Field from Dislocations

In contrast to the initial mismatch strain, the strain distribution in the epilayer due to the interfacial dislocations is spatially nonuniform. During growth of InGaAs on GaAs, two orthogonal dislocation arrays develop at the interface during strain relaxation, consisting of 60° misfits aligned along the two $\langle 110 \rangle$ directions. We treat the two dislocation arrays independently.

Freund and Jonsdottir [10] give an expression for the strain field at the surface arising from an array of parallel misfit dislocations spaced periodically at the interface. According to transmission electron microscopy (TEM) measurements, the dislocations in the films considered here are not periodic but are approximately randomly spaced. Using Eq. 4.3, the density of these dislocations is consistent with the film relaxation inferred from x-ray diffraction, to within a factor of 2 [26, 56]. To handle the case of randomly

spaced dislocations, it will be useful to know the strain field arising from a single dislocation. Taking the limit of large dislocation spacing, the result of reference [10] reduces to

$$\epsilon_1(x) = -\frac{bz}{\pi} \frac{(x^2 - \sqrt{2}xz)}{(x^2 + z^2)^2}, \quad (4.7)$$

which is the extensional strain field ϵ_{xx} at the surface due to a *single* 60° interfacial misfit dislocation. This expression corresponds to a dislocation in which the dislocation line runs parallel to the y -axis and is located at the interface at $x = 0$. Here z is equal to the film thickness, and x is the in-plane $\langle 110 \rangle$ direction perpendicular to the dislocation array. There is also an in-plane shear strain ϵ_{xy} associated with the screw component of these dislocations [10], however as we show in the next section this component is expected to have a negligible effect on the surface roughening.

The thickness dependence of the surface strain given by Eq. 4.7 is shown in Figure 4.3, for the dislocation represented in Fig. 4.1. A value of 0.4 nm is used for the Burgers vector, appropriate to the InGaAs/GaAs system. The lateral variation in the surface strain arises from the singularity in the lattice deformation field, which is localized along the dislocation line at $x = 0$. Thus the local perturbation in the surface strain field is centered directly above the dislocation line.

As shown in the Fig. 4.1, slip along the (111) plane associated with the dislocation creates a surface step. During subsequent film growth, adatoms will attach to this step so that it will migrate away from its initial location. Thus the atomic-height steps arising from the dislocation formation process are not expected to contribute directly

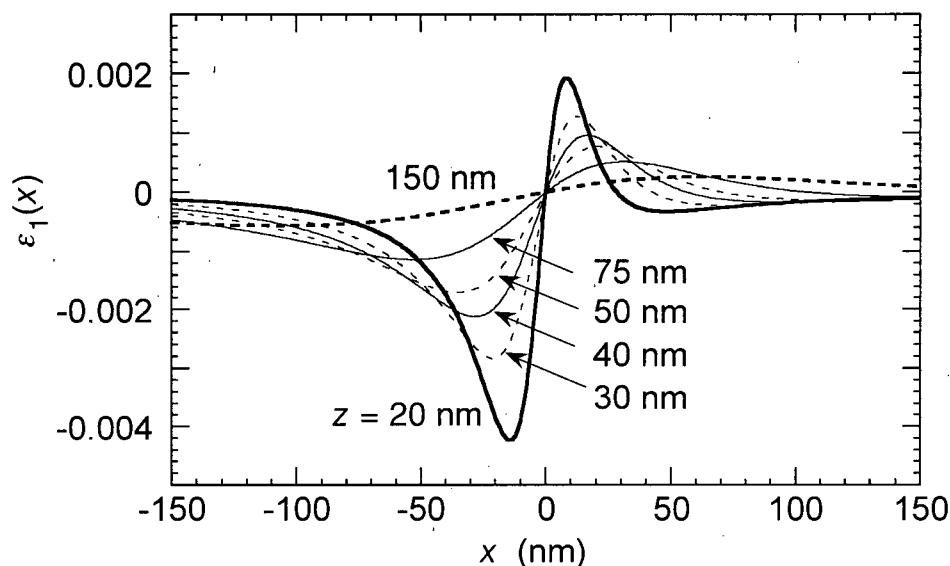


Figure 4.3: Strain field due to a single misfit dislocation located at the origin, for increasing film thickness.

to the formation of surface ridges. On the other hand, the position of the strain-field perturbation (Fig. 4.3) is fixed by the position of the dislocation line. In Section 4.2 we will show that the migration of adatoms in response to the strain-field pattern associated with the dislocations, can account for the observed surface crosshatch. To accomplish this, we will first need to relate the local surface strain to the chemical potential of an adatom on the surface.

4.1.4 Strain and Surface Energy

The free energy F per unit volume, associated with elastic strain in a crystal having cubic symmetry is [49]

$$F = \frac{1}{2}c_{11}(\epsilon_{xx}^2 + \epsilon_{yy}^2 + \epsilon_{zz}^2) + c_{12}(\epsilon_{xx}\epsilon_{yy} + \epsilon_{xx}\epsilon_{zz} + \epsilon_{yy}\epsilon_{zz}) + 2c_{44}(\epsilon_{xy}^2 + \epsilon_{xz}^2 + \epsilon_{yz}^2), \quad (4.8)$$

where c_{11} , c_{12} and c_{44} are the three independent components of the elastic stiffness tensor, and ϵ_{ij} are the extensional ($i = j$) and shear ($i \neq j$) strains. We take the surface normal to be aligned with the z direction. The strains are related to the applied stresses σ_{ij} , by Hooke's law for a cubic crystal:

$$\begin{pmatrix} \sigma_{xx} \\ \sigma_{yy} \\ \sigma_{zz} \\ \sigma_{xy} \\ \sigma_{xz} \\ \sigma_{yz} \end{pmatrix} = \begin{pmatrix} c_{11} & c_{12} & c_{12} & 0 & 0 & 0 \\ c_{12} & c_{11} & c_{12} & 0 & 0 & 0 \\ c_{12} & c_{12} & c_{11} & 0 & 0 & 0 \\ 0 & 0 & 0 & c_{44} & 0 & 0 \\ 0 & 0 & 0 & 0 & c_{44} & 0 \\ 0 & 0 & 0 & 0 & 0 & c_{44} \end{pmatrix} \begin{pmatrix} \epsilon_{xx} \\ \epsilon_{yy} \\ \epsilon_{zz} \\ \epsilon_{xy} \\ \epsilon_{xz} \\ \epsilon_{yz} \end{pmatrix}. \quad (4.9)$$

Since the film has a free surface parallel to the xy plane, the z -components of stress must vanish. Thus from Equation 4.9 we obtain,

$$\epsilon_{zz} = -\frac{c_{12}}{c_{11}}(\epsilon_{xx} + \epsilon_{yy}), \quad \epsilon_{xz} = 0, \quad \epsilon_{yz} = 0. \quad (4.10)$$

With these substitutions Eq. 4.8 becomes,

$$F = \frac{1}{2}c_{11} \left[1 - \left(\frac{c_{12}}{c_{11}} \right)^2 \right] (\epsilon_{xx}^2 + \epsilon_{yy}^2) + c_{12} \left(1 - \frac{c_{12}}{c_{11}} \right) \epsilon_{xx}\epsilon_{yy} + 2c_{44}\epsilon_{xy}^2. \quad (4.11)$$

Equation 4.11 is quadratic in the strains. In what follows, we will be interested in the local *fluctuations* in F at the surface, due to the misfit dislocation strain fields. To simplify the calculation, we obtain a linear approximation to the fluctuation in F , valid for small deviations in the strain field from its mean value. As we will see later, for an initial mismatch of $f = 0.013$, the critical thickness is approximately 40 nm. Therefore at thicknesses above the critical thickness, the local deviations in the strain due to the dislocations are typically small compared to the average strain, according to Fig. 4.3.

First we note that since the initial misfit strain is a pure compression of the epilayer lattice in the xy plane, there is no initial in-plane shear component ϵ_{xy} . Thus the final term in Eq. 4.11 is second order in the dislocation shear strain field, and is neglected. We denote the residual x -component of the extensional strain field, averaged over the film, as $\bar{\epsilon}_{xx}$. This is linearly related to the density of misfit dislocations by Eq. 4.3. Taking the local deviations in the surface strain from $\bar{\epsilon}_{xx}$ to be small we find,

$$\epsilon_{xx}^2(x) = \bar{\epsilon}_{xx}^2 + 2\bar{\epsilon}_{xx}(\epsilon_{xx} - \bar{\epsilon}_{xx}) + \dots \approx 2\bar{\epsilon}_{xx}f - \bar{\epsilon}_{xx}^2 + 2\bar{\epsilon}_{xx}\Delta\epsilon_{xx}(x) \quad (4.12)$$

where $\Delta\epsilon_{xx}(x)$ is the sum of the contributions to the surface strain at x from all dislocations present at the interface. In obtaining Equation 4.12 we have used the relation $\epsilon_{xx} \equiv f + \Delta\epsilon_{xx}$. Only the final term of Eq. 4.12, which contains all of the x dependence, is of further interest. An analogous expression applies for ϵ_{yy}^2 . An expansion of the cross term, $\epsilon_{xx}\epsilon_{yy}$ yields,

$$\epsilon_{xx}\epsilon_{yy}(x, y) = (\bar{\epsilon}_{xx} + \bar{\epsilon}_{yy})f - \bar{\epsilon}_{xx}\bar{\epsilon}_{yy} + \bar{\epsilon}_{yy}\Delta\epsilon_{xx}(x) + \bar{\epsilon}_{xx}\Delta\epsilon_{yy}(y), \quad (4.13)$$

where only the last two terms contribute to lateral variations in F .

Combining Eqs. 4.11, 4.12 and 4.13, the x -dependent fluctuation in the surface strain energy $\tilde{F}_{\text{surf}}(x)$ may be written,

$$\tilde{F}_{\text{surf}}(x) = \left\{ c_{11} \left[1 - \left(\frac{c_{12}}{c_{11}} \right)^2 \right] \bar{\epsilon}_{xx} + c_{12} \left(1 - \frac{c_{12}}{c_{11}} \right) \bar{\epsilon}_{yy} \right\} \Delta\epsilon_{xx}(x). \quad (4.14)$$

Similarly for the variation in the y direction,

$$\tilde{F}_{\text{surf}}(y) = \left\{ c_{11} \left[1 - \left(\frac{c_{12}}{c_{11}} \right)^2 \right] \bar{\epsilon}_{yy} + c_{12} \left(1 - \frac{c_{12}}{c_{11}} \right) \bar{\epsilon}_{xx} \right\} \Delta\epsilon_{yy}(y). \quad (4.15)$$

According to Eq. 4.7, the set of dislocations that contributes to $\Delta\epsilon_{xx}(x)$ is orthogonal to the set that contributes to $\Delta\epsilon_{yy}(y)$. Thus $\tilde{F}_{\text{surf}}(x)$ and $\tilde{F}_{\text{surf}}(y)$ are coupled only through the average strains in both directions, weighted by the elastic constants. For GaAs, these constants are given by $c_{11} = 1.18$ dynes/cm² and $c_{12} = 0.54$ dynes/cm² [57].

4.2 Continuum Equation for Strained-Layer Growth

In using a continuum equation to model surface growth, it is assumed that the film can be considered to be built up of identical units that diffuse on the surface in response to local conditions. For III-V MBE growth, the surface morphology evolution is controlled by the diffusion of group III atoms, since the group V element is supplied in excess. Hence we refer to the identical units as atoms. For the case of an alloy, this unit reflects the average alloy composition. The volume Ω of an “atom” of $\text{In}_x\text{Ga}_{1-x}\text{As}$ is given by:

$$\Omega = \frac{a_0^3}{4} \quad (4.16)$$

where

$$a_0 = a_{\text{GaAs}}(1 - x) + a_{\text{InAs}}x \quad (4.17)$$

is the equilibrium lattice constant of the alloy. The lattice constants a_{GaAs} and a_{InAs} for the constituent binary materials, are equal to 5.65 Å and 6.06 Å respectively [58]. The continuum approach neglects the possibility that the film will order into regions of differing composition, however due to the associated entropy decrease this effect is only expected to be important at significantly lower temperatures than considered here [50].

We consider contributions to the chemical potential $\mu(x, t)$ of an atom diffusing on the surface of a strained film, arising from both the surface curvature and the strain field at position x and time t . The energy per unit area of an unstrained film is approximated by $\gamma/(1 + 2a\kappa)$, where γ is the surface tension of a planar film, a is the lattice constant, and κ is the local curvature [59]. Thus for a strained film,

$$\mu(x, t) = -2\Omega\gamma\nabla^2 h(x, t) + \Omega F(x, t) + \mu_0(t). \quad (4.18)$$

where $h(x, t)$ is the local height of the surface and $\mu_0(t)$ is the chemical potential of the unstressed flat surface. In writing Eq. 4.18 we have used the identity: $\kappa \equiv \nabla^2 h$.

The lateral flux of atoms on the surface $\vec{j}(x, t)$ is

$$\vec{j}(x, t) = -\frac{Dn_0}{kT}\vec{\nabla}\mu(x, t) - \frac{\nu}{\Omega}\vec{\nabla}h(x, t). \quad (4.19)$$

where D is the surface diffusion constant, n_0 is the adatom surface coverage, and T is the substrate temperature. The first term in Equation 4.19 is proportional to the adatom concentration gradient. The second term is a “diffusion bias” proportional to the local surface slope, and arises from the activation barrier, called a Schwoebel barrier, associated with diffusion over an atomic step [5]. The parameter ν has the units of a diffusion constant, and is discussed further at the end of this section.

Applying the continuity equation to Eq. 4.19,

$$\frac{\partial h(x, t)}{\partial t} = -\Omega \vec{\nabla} \cdot \vec{j} = \nu \nabla^2 h - K \nabla^4 h + \alpha c_{11} \bar{\epsilon}_{\text{eff}}(t) \nabla^2 [\Delta \epsilon_{xx}(x, t)], \quad (4.20)$$

where

$$K = 2\alpha\gamma, \quad \alpha = \frac{\Omega^2 D n_0}{kT} \quad (4.21)$$

and

$$\bar{\epsilon}_{\text{eff}}(t) = \left[1 - \left(\frac{c_{12}}{c_{11}} \right)^2 \right] \bar{\epsilon}_{xx}(t) + \frac{c_{12}}{c_{11}} \left(1 - \frac{c_{12}}{c_{11}} \right) \bar{\epsilon}_{yy}(t) \approx \frac{3}{4} \bar{\epsilon}_{xx}(t) + \frac{1}{4} \bar{\epsilon}_{yy}(t). \quad (4.22)$$

We have used Eq. 4.14 for the final term of Equation 4.20, and we have omitted a constant term associated with the constant growth rate of the film. This equation is equivalent to the linear MBE equation [4], with the exception that the effect of surface strain has been included, and a noise term due to the random nature of the deposition flux has been neglected. The final approximation in Equation 4.22 applies to $\text{In}_x\text{Ga}_{1-x}\text{As}$ films: $c_{12}/c_{11} \approx 1/2$. As shown below (Equation 4.29), $\bar{\epsilon}_{\text{eff}}$ can be treated as the effective extensional strain in the x direction.

Taking the spatial Fourier transform of Eq. 4.20 we obtain,

$$\frac{\partial \hat{h}(q_x, t)}{\partial t} + \nu q_x^2 \hat{h}(q_x, t) + K q_x^4 \hat{h}(q_x, t) = -\alpha c_{11} q_x^2 \bar{\epsilon}_{\text{eff}}(t) \widehat{\Delta \epsilon_{xx}}(q_x, t). \quad (4.23)$$

As discussed following Eq. 4.15, only the set of dislocations aligned along the y direction contributes to $\Delta \epsilon_{xx}$. Consistent with the TEM measurements on these films, we take these dislocations to be randomly spaced in the x direction, with average linear density $\rho_x(t)$. In this case,

$$\widehat{\Delta \epsilon_{xx}}(q_x, t) = \sqrt{\rho_x(t)} \hat{\epsilon}_1(q_x, z_t), \quad (4.24)$$

where the film thickness z_t is linearly related to the growth time t through the growth rate g : $z_t = gt$. Here $\hat{\epsilon}_1(q_x, z)$ is the Fourier transform of the strain field from a single dislocation, and is obtained by Fourier transforming Eq. 4.7 with respect to x :

$$\hat{\epsilon}_1(q_x, z) = \frac{b}{2} e^{-z|q|} (z|q| - 1 + i\sqrt{2}z|q|). \quad (4.25)$$

Note that this expression describes the strain field variation along an initially planar surface, immediately after a dislocation has formed. During subsequent film growth, ridges develop on the surface so that the geometry of the epilayer changes. According to AFM [see for example Fig. 1.2(a)], these ridges have a very low aspect ratio (typically less than 1:100), and a height on the order of 1% of the film thickness, so that they represent a relatively minor perturbation in the overall film geometry. We therefore consider Eq. 4.25 to apply equally well to the description of the strain field in the presence of the surface ridges.

For film thicknesses above the critical thickness, the solution of Eq. 4.23 is given by,

$$\hat{h}(q_x, z_t) = -Aq_x^2 e^{-(\nu q_x^2 + Kq_x^4)(z_t - z_c^x)/g} \int_{z_c^x}^{z_t} e^{(\nu q_x^2 + Kq_x^4)(z - z_c^x)/g} \bar{\epsilon}_{\text{eff}}(z) \rho_x^{1/2}(z) \hat{\epsilon}_1(q_x, z) dz, \quad (4.26)$$

where

$$A = \frac{\Omega^2 D n_0 c_{11}}{gkT}. \quad (4.27)$$

In Equation 4.26 z_t is the film thickness at time t , and z_c^x is the critical thickness for strain relaxation in the x direction. Using Eqs. 4.3 and 4.6,

$$\bar{\epsilon}_{xx}(z) = \begin{cases} f, & z < z_c^x \\ f z_c^x / z, & z > z_c^x \end{cases}, \quad \bar{\epsilon}_{yy}(z) = \begin{cases} f, & z < z_c^y \\ f z_c^y / z, & z > z_c^y \end{cases}, \quad \rho_x(z) = \frac{2}{b} (f - \bar{\epsilon}_{xx}) \quad (4.28)$$

where we have allowed for a different critical thickness z_c^y in the y direction.

The residual strains $\bar{\epsilon}_{xx}$ and $\bar{\epsilon}_{yy}$ are linearly related according to Eq. 4.28, once the critical thickness has been exceeded in both directions. Experimentally we find that $z_c^x \approx z_c^y$. To a good approximation we can therefore simplify Eq. 4.26 with the following substitutions:

$$\bar{\epsilon}_{\text{eff}}(z) \leftarrow \bar{\epsilon}_{xx}(z), \quad A \leftarrow \left[1 - \left(\frac{c_{12}}{c_{11}} \right)^2 + \frac{c_{12}z_c^y}{c_{11}z_c^x} \left(1 - \frac{c_{12}}{c_{11}} \right) \right] A \quad (4.29)$$

Since $c_{12}/c_{11} \approx 1/2$ for these films, the quantity in square brackets is very nearly unity.

We find that use of the substitutions in Eq. 4.29 changes the resulting PSD at any given film thickness by less than 5%, when z_c^x and z_c^y differ by a factor of 1.5. Thus the time dependence of the roughening in the x direction, depends only on the strain fields associated with the dislocations aligned along the y direction. The relaxation in the y direction effectively rescales the prefactor A by a factor close to unity. An analogous expression to Eq. 4.26 describes the roughening in the y -direction due to the dislocations aligned along the x direction. In what follows we will use the substitutions in Eq. 4.29, and treat the roughening in the two $\langle 110 \rangle$ directions independently.

Equation 4.20 has the property that unless ν is zero, the $\nu \nabla^2 h$ term will dominate the surface evolution above a crossover length scale, given by [4]

$$L_1 = \sqrt{\frac{K}{\nu}}. \quad (4.30)$$

The form of Eq. 4.20 in which K is zero and ν is nonzero, is known as the Edwards-Wilkinson (EW) equation, and is the simplest non-trivial growth equation with the required symmetry. As we will see, the EW form describes the experimental data very

well, implying that the length scales accessible to light scattering are above L_1 . The dominance of the EW term on long length scales leads to a characteristic -2 power law in the 2D PSD at low spatial frequencies. This is consistent with the PSD measurements for GaAs buffer layers presented in Chapter 2.

We can obtain an approximate expression for ν if we consider an adatom deposited on a surface having a local slope of magnitude: $|\vec{\nabla}h| = a/W$, where W is the terrace width along the x -direction and a is the lattice constant, which is the height of the step at the edge of each terrace. On average the atom will diffuse for a time $t_D \approx W^2/D$ before it reaches either the up-step or the down-step of the terrace. We define a “bias factor” β , which is the difference in success rate for an adatom attempting to go over the down-step, or to attach to the up-step (positive if the first probability is higher). The net one-dimensional flux associated with this diffusion bias is then given by: $j_{\text{bias}} = W\beta n_0/t_D$. Equating this with the second term in Eq. 4.19 we obtain,

$$\nu = \beta a^2 D n_0. \quad (4.31)$$

Another mechanism that can produce a $\nabla^2 h$ term in the growth equation is desorption of adatoms, which results in non-conservative growth [4]. In this case a curvature-dependent term, representing the difference in chemical potential between a condensed adatom and its vapor, is added directly to the continuity equation. This mechanism is not expected to be relevant in our case since desorption is not significant at the growth temperatures used here.

The model developed in this section will be compared to experimental data obtained

in real time using laser light scattering, during growth of $\text{In}_x\text{Ga}_{1-x}\text{As}$ films on GaAs. As pointed out above the scattered light intensity is proportional to the power spectral density of the surface. The one-dimensional scattering that results from the surface crosshatch is therefore proportional to $|\widehat{h(q,t)}|^2$. This can be obtained by integrating Eq. 4.26 numerically. The mismatch f and the growth rate g are known experimentally. Since we will usually take K to be zero, there are only three fitting parameters: the prefactor A , the critical thickness in the direction of interest, and the constant ν from the EW equation.

4.3 Measurement of Surface Crosshatch

4.3.1 Sample Growth and Light Scattering

The substrate preparation procedures used in these experiments are described in Section 2.3. Following the thermal oxide desorption, a $1\text{ }\mu\text{m}$ thick GaAs buffer layer was grown at 590°C at a growth rate of $1\text{ }\mu\text{m/hr}$. Before termination of the buffer layer growth the substrate temperature was ramped down to the required temperature for the $\text{In}_x\text{Ga}_{1-x}\text{As}$ growth. Except for the growths in Section 4.5 where the effect of growth temperature was explored, the substrate was held at 490°C for the InGaAs growth. The As_2 to Ga flux ratio was 3.5:1, as measured with an ion gauge placed at the sample position, and these fluxes were held constant throughout growth of the GaAs and InGaAs layers.[34]

In Fig. 4.4(a) we show a $20 \times 20\text{ }\mu\text{m}^2$ AFM image of a 250 nm thick $\text{In}_x\text{Ga}_{1-x}\text{As}$ film.

This image shows the well-known $\langle 110 \rangle$ crosshatch pattern which is observed in relaxed InGaAs films. We note that the ridges which make up the crosshatch pattern are 1 to 3 nm high, which is considerably higher than the atomic-size steps one would expect from the slip along $\{111\}$ planes associated with individual misfit dislocations. As discussed in Section 4.2, these ridges are believed to be caused by surface diffusion in response to the inhomogeneous strain associated with the misfit dislocations. The 2D power spectrum obtained by Fourier transforming a $100 \times 100 \mu\text{m}^2$ AFM image of the same sample is shown in Fig. 4.4(b). This large scale image was acquired with an AFM for which the lateral nonlinearity over the scan range was less than 5% [60]. We note that there is very little angular spread in the $\langle 110 \rangle$ cross pattern in the PSD in this case. The corresponding scattering lines are one-dimensional, with a width determined by the divergence of the laser beam. As discussed in Section 3.2, it is therefore critical to align the scattering planes accurately along the $\langle 110 \rangle$ directions in the substrate at the beginning of the experiment. In Sections 4.4.1 and 4.5.1 we will present light scattering measurements of the time-dependence of the PSD during growth, monitored simultaneously along both $\langle 110 \rangle$ directions, at scattering angles corresponding to spatial frequencies of $5.4 \mu\text{m}^{-1}$ and $10.5 \mu\text{m}^{-1}$. These spatial frequencies are indicated by the 4 crosses in Fig. 4.4(b).

4.3.2 Analysis of Light Scattering Data

The model describes the time evolution of the 1D roughness associated with the crosshatch pattern that develops during strained layer growth. Experimentally, a diffuse background

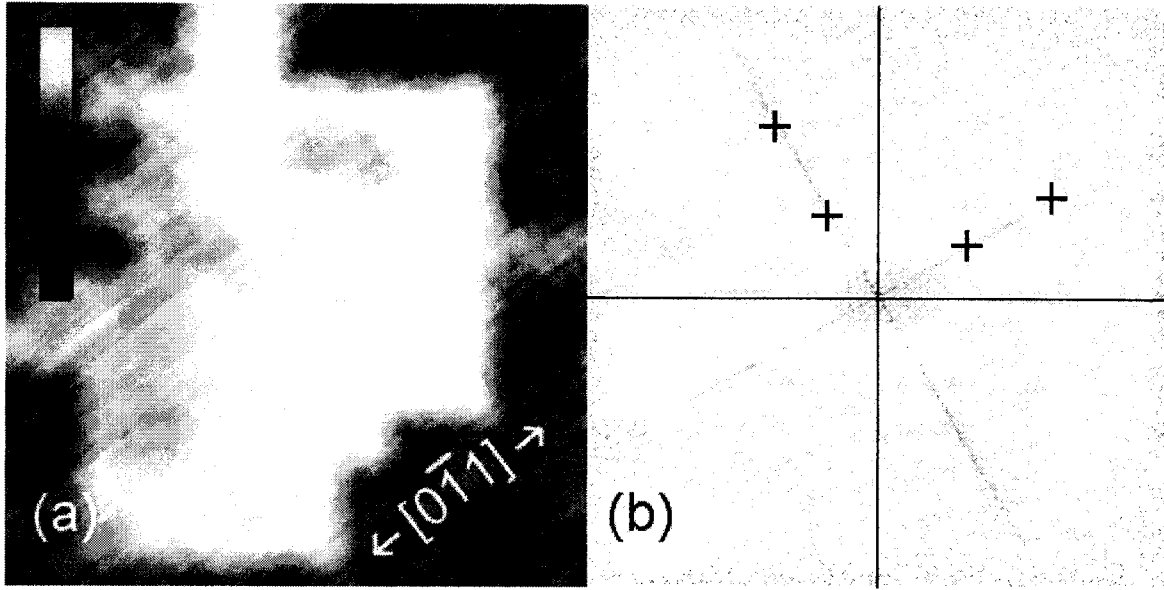


Figure 4.4: (a) $20 \times 20 \mu\text{m}^2$ AFM image of a 250 nm thick InGaAs film, with a 10 nm vertical gray scale and (b) power spectrum calculated from a $100 \times 100 \mu\text{m}^2$ image of the same film, where the gray scale represents the logarithm of the PSD at each spatial frequency, q . The axes for the PSD are oriented approximately along $\langle 100 \rangle$ directions and span a q range of $\pm 16 \mu\text{m}^{-1}$ ($q = 0$ at origin). The 4 crosses in (b) indicate the spatial frequencies monitored by *in situ* light scattering.

signal is collected by the detector lens along with the sharp scattering line associated with the strain relaxation. This background intensity is the sum of the 2D scattering from the GaAs buffer layer roughness, and any stray scattered light that falls within the detection solid angle. In contrast to the intense 1D scattering from the surface crosshatch, the diffuse background scattering from the buffer layer is approximately isotropic and remains nearly constant throughout the subsequent InGaAs growth, as verified by *ex situ* light scattering analysis of films grown to different thicknesses [34]. The 1D scattering of interest can therefore be isolated by subtracting the diffuse background signal, as

approximated by the signal intensity immediately following the buffer layer growth.

In order to compare the relative intensities of signals measured at different ports or during different growth experiments, the *in situ* light scattering measurements presented here have all been normalized to the 2D background intensity immediately following the buffer layer growth, prior to background subtraction. According to Eq. 2.5, the magnitude of the background intensity will depend on the detector solid angle $\Delta\Omega$ and the magnitude $g_{2D}(q)$ of the 2D PSD associated with the buffer layer roughness at the spatial frequency of interest. On the other hand, the 1D scattering signal measured during growth of the strain-relaxed InGaAs layer, will depend on the detector acceptance angle $\Delta\theta$ in the plane of incidence, and the 1D PSD, $g_{1D}(q)$ of the surface crosshatch, according to Eq. 2.8. Comparing Eqs. 2.5 and 2.8, we find that the normalized 1D scattering intensity $I_{q,\text{norm}}$ at a spatial frequency q is given by,

$$I_{q,\text{norm}} = \lambda \frac{\Delta\theta}{\Delta\Omega} \frac{g_{1D}(q)}{g_{2D}(q)}. \quad (4.32)$$

The ratio of the normalized 1D intensities measured at two different optical ports, corresponding to two different spatial frequencies q_1 and q_2 , is therefore related to the ratio of the corresponding 1D power spectral densities by

$$\frac{I_{q_1,\text{norm}}}{I_{q_2,\text{norm}}} = \left(\frac{q_1}{q_2}\right)^m \frac{\Delta\Omega_{q_2} \Delta\theta_{q_1} g_{1D}(q_1)}{\Delta\Omega_{q_1} \Delta\theta_{q_2} g_{1D}(q_2)}, \quad (4.33)$$

where $\Delta\Omega_{q_i}$ and $\Delta\theta_{q_i}$ are the acceptance angles of the detectors associated with spatial frequency q_i , and are given in Table 3.2. Equation 4.33 accounts for a q^{-m} roll-off of the buffer layer roughness. In the analysis that follows we will take m equal to 2 over the spatial frequency range of 5 to 10.5 μm^{-1} . This is consistent with the *ex situ*

light scattering results in Section 2.3.4, which were obtained from a GaAs buffer layer grown at the time of the InGaAs strained-layer growth experiments considered here. This buffer layer was grown specifically to determine the starting film roughness in these experiments, so that special care was taken to ensure that the substrate preparation and growth conditions were the same [34]. Considering variabilites in optical alignment for the real-time measurements, and run-to-run variations in the q -dependence of the buffer layer roughness, we expect Eq. 4.33 to hold to within a factor of 4 or 5. This assumes that the contribution of stray scattered light to the background signal is negligible.

4.4 Comparison of Model and Experiment

4.4.1 Time Dependence

The time-evolution of the scattered light intensity during growth of a strained $\text{In}_{0.18}\text{Ga}_{0.82}\text{As}$ film is shown in Figure 4.5 (heavy lines). The detected light signals probe lateral length scales of $1.2\ \mu\text{m}$ and $0.6\ \mu\text{m}$, along the $[1\bar{1}0]$ direction in the crystal surface. Each signal has been normalized to the initial scattering signal from the buffer layer, and a constant factor equal to unity has been subtracted from each normalized curve as described in Section 4.3.2. There is a sharp increase in scattering when the film is about 50 nm thick. *Ex situ* structural analyses on these films showed that the surface roughening coincides with the formation of misfit dislocations [26, 56].

The PSD obtained by integrating Eq. 4.26 numerically for the appropriate value of

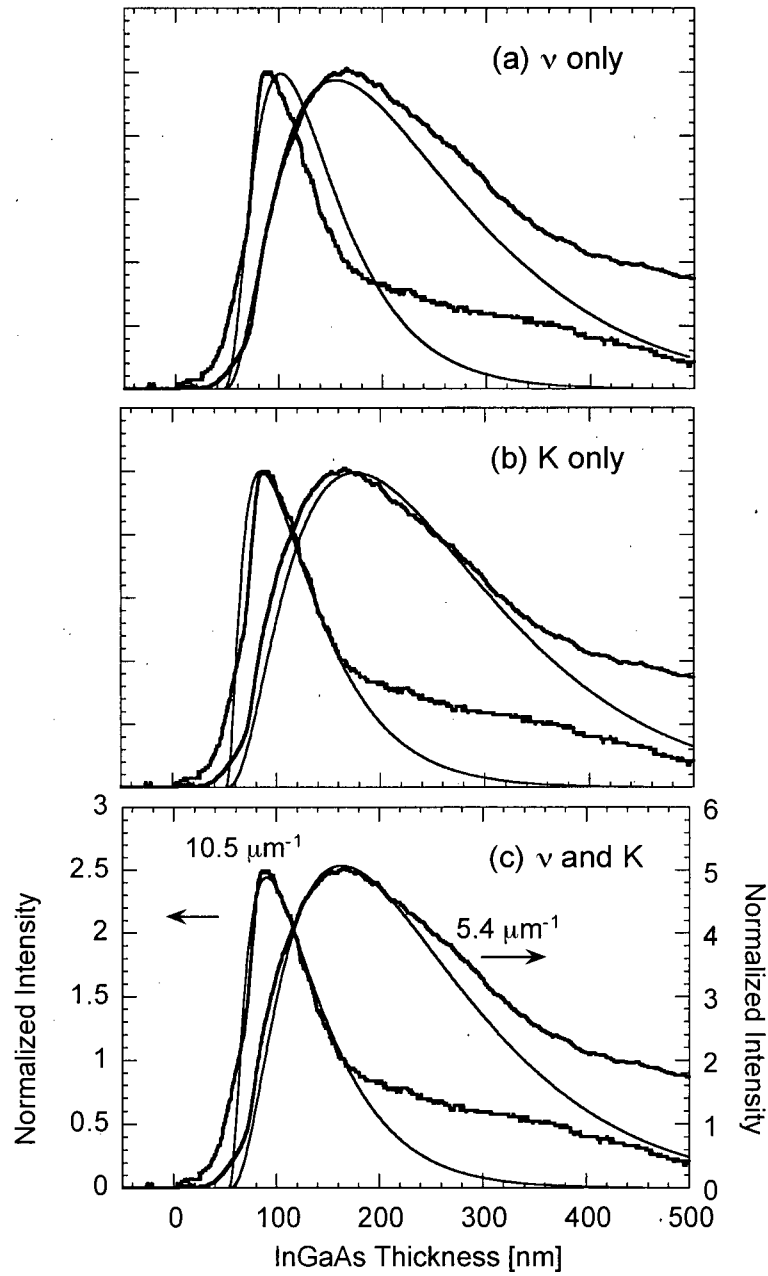


Figure 4.5: *In situ* light scattering measurements (thick lines) of surface roughness at $q = 5.4$ and $10.5 \mu\text{m}^{-1}$ during growth of an $\text{In}_{0.18}\text{Ga}_{0.82}\text{As}$ film at 490°C , and calculated time evolution of the 1D PSD (thin lines) using different combinations of ν and K .

	Direction	ν ($\times 10^{-12}$ cm ² /s)	K ($\times 10^{-22}$ cm ⁴ /s)	z_c (nm)	R
Fig. 4.5a	[1 $\bar{1}$ 0]	1.25	0	45	7.3
b		0	3.9	50	0.9
c		0.67	2.7	52	2.2
Fig. 4.8a		2.8	0	49	4.4
Fig. 4.7	[110]	0.11	0	55	11.5
Fig. 4.8b		0.28	0	56	5.3

Table 4.1: Parameter values used for the fits in Figures 4.5, 4.7 and 4.8.

q , is fitted to the time-dependent light scattering data in Figures 4.5(a-c), using the experimental growth rate ($g = 1$ $\mu\text{m/hr}$) and lattice mismatch ($f = 0.013$). The results of three simulations are shown (thin lines), which use different combinations of the parameters ν , K and z_c . The same parameter values are used to fit the signals at both spatial frequencies in each case, however the prefactor A has been scaled independently to match the experimental peak intensities. The ratio $g_{1D}(q = 10.5 \mu\text{m}^{-1})/g_{1D}(q = 5.4 \mu\text{m}^{-1})$ of the two measured spatial-frequency components of the 1D PSD can be estimated from the normalized scattering data using Eq. 4.33. Accounting for experimental uncertainty, this ratio should agree within a factor of 5 with the corresponding ratio predicted by the model when A is the same for both spatial frequencies. In order to compare the different model fits, we define a scale factor R , which is the amount by which the signal at $10.5 \mu\text{m}^{-1}$ must be scaled relative to the signal at $5.4 \mu\text{m}^{-1}$, so that the ratio of these signal intensities agrees with the model. The results of these fits are summarized in Table 4.1.

The film thickness for maximum roughness and the widths of the peaks at different spatial frequencies calculated from the model approximately match the *in situ* measurements in Fig. 4.5. In addition the relative peak intensities generally agree with the model within experimental uncertainty. According to Eq. 4.26 the effect of ν and K on the time-dependence is contained in the quantity $\nu + Kq^2$, so it is not possible to determine the relative weights of these parameters based on a measurement at a single spatial frequency. The overall fit is improved when both parameters are included [Fig. 4.5(c)], which permits the quantity $\nu + Kq^2$ to be fit independently for each q . The model predicts that the roughness goes to zero faster for thick films than is observed experimentally. This may be due to complicated dislocation structures not considered in the model, such as pile-ups, which are believed to act in the later stages of relaxation [53]. Consistent with the discussion in Section 4.1.2, the fitted z_c is approximately five times the Matthews-Blakeslee critical thickness. The small continuous increase in roughening below z_c in the experiment may be due to preexisting threading dislocations from the substrate bending over into the plane of the interface. Substantial strain relaxation does not occur until the film thickness exceeds the equilibrium critical thickness sufficiently to cause nucleation of large numbers of dislocations.

As discussed above, a $1/z$ law is used to approximate the film relaxation above the critical thickness. In Table 4.2 we compare the $1/z$ dependence to experimental values of the relaxation obtained by X-ray diffraction. X-ray measurements [34] were performed on three films grown to different thicknesses under nominally the same growth conditions

Film Thickness (nm)	Percentage Relaxation			
	[1 $\bar{1}$ 0]		[110]	
	X-ray	1/z	X-ray	1/z
33	< 0.5	0	< 0.5	0
58	11	10.3	7	5
83	31	37	22	33

Table 4.2: Measured relaxation compared with a $1/z$ law, using critical thicknesses of 52 nm and 55 nm for the [1 $\bar{1}$ 0] and [110] directions respectively.

as the one in Fig. 4.5. The measured values for relaxation in the [1 $\bar{1}$ 0] direction are in reasonable agreement with the $1/z$ law for a critical thickness of 52 nm, consistent with the fit in Fig. 4.5(c). The effect of deviations in the strain relaxation rate from the $1/z$ law will be treated in Section 4.5.1. In particular, it will be found that this can account for the slightly large value of R associated with the fit in Fig. 4.5(a).

4.4.2 Spatial-Frequency Dependence

The [1 $\bar{1}$ 0] 1D power spectra determined from *ex situ* light scattering are shown in Figure 4.6. The experimental details of the light scattering measurement are described in Chapter 2, as well as the procedure used to extract the 1D PSD from the scattered light distribution. As demonstrated in Section 2.3.5 the 1D PSD obtained in this way agrees quantitatively with that determined from Fourier transforms of AFM data. The three sets of data (solid symbols in Fig. 4.6) were taken from films grown to different thicknesses under nominally the same conditions as the film in Fig. 4.5.

The results of model simulations, using a critical thickness of 52 nm consistent with

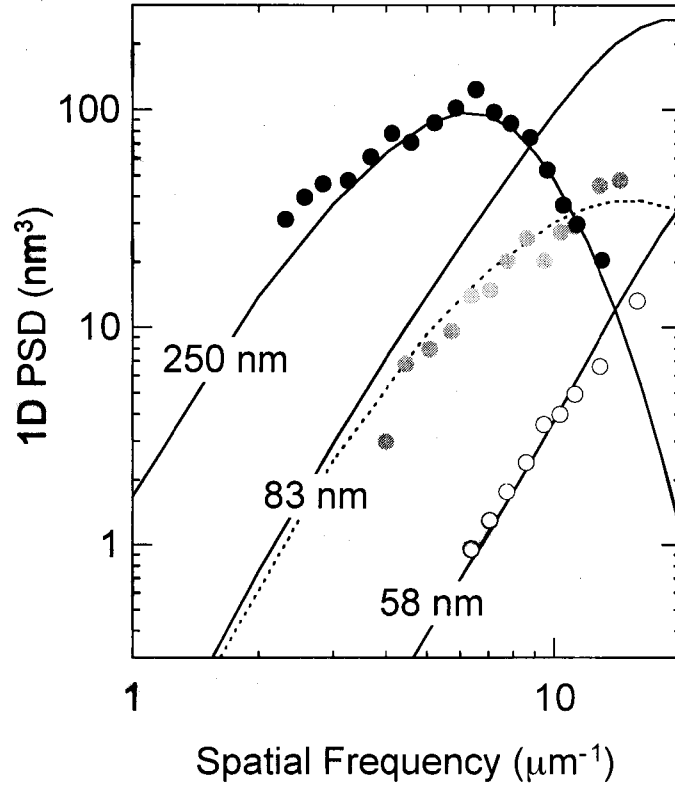


Figure 4.6: *Ex situ* light scattering data (symbols) and model data (solid and dashed lines) for the 1D PSD along $[1\bar{1}0]$ of three InGaAs films with different thicknesses above the critical thickness.

the X-ray measurements, are plotted along with the light scattering data in Fig. 4.6 (solid curves). In obtaining these fits, K was taken to be zero and a value of ν of 1.0×10^{-12} cm²/s was used, which is very close to the value used to fit the time-dependent *in situ* data in Fig. 4.5(a). The prefactor A is the same for the fits at all three thicknesses. The calculated q dependence of the surface roughness agrees remarkably well with the q -dependent light scattering data. The model shows the same trends with thickness as the experiment, with the same rising slope and a peak in the PSD at

$\sim 6 \mu\text{m}^{-1}$ for the thickest film. The roughness develops first at high spatial frequencies. This is expected because the surface topography will develop more rapidly at short length scales where a smaller amount of material needs to be transported a shorter distance to create the same amplitude on the surface. The high frequency roughness decreases at large thicknesses because the high frequency content of the surface strain field drops as the distance from the interface increases, as is apparent from Fig. 4.3.

Although the fits to the 250 nm and 58 nm thick film are excellent, the q dependence of the simulation at 83 nm deviates from the experimental data at higher spatial frequencies, by a factor of 3 at $10 \mu\text{m}^{-1}$. This can be attributed to run-to-run variations in growth conditions. For example, the dashed curve in Fig. 4.6 was obtained using a value of ν of $2.8 \times 10^{-12} \text{ cm}^2/\text{s}$, which is within a factor of 3 of that used to obtain the other fits. The other fitting parameters were unchanged. This variation in ν is not surprising, given the sensitivity of the model parameters to substrate temperature and film composition described in Section 4.5.

Simulations were also performed in which K was taken to be nonzero, however this additional fitting parameter did not result in an improvement to the fits of the q dependence. In contrast to the excellent agreement obtained using the EW form of Eq. 4.26, calculations in which ν was taken to be zero could not reproduce the q -dependence of the thickest film in Fig. 4.6. This suggests that the crossover length scale L_1 (Eq. 4.30) is smaller than the length scales accessible in these measurements.

The absolute magnitude of the 1D PSD for the thickest film in Fig. 4.6 is believed to

be correct to within a factor of 3, based on the agreement between the AFM and *ex situ* light scattering measurements on this sample in Section 2.3.5. Using Eq. 4.27 for A , we find that in order for the calculated PSD to match the experimental PSD at the peak ($q \sim 6 \mu\text{m}^{-1}$), the quantity Dn_0 must be equal to $4.5 \times 10^5 \text{ s}^{-1}$. The surface diffusion constant D and the adatom density n_0 depend sensitively on growth conditions and are not known for this system, however an activation energy for surface diffusion of 0.6 eV, and a value for D of $2 \times 10^{-6} \text{ cm}^2/\text{s}$ has been reported for GaAs (001) homoepitaxy at 530°C [61, 62]. This activation energy is consistent with our own measurements of diffusion during InAs quantum dot growth in Chapter 5. Using these values, n_0 must be about $3 \times 10^{11} \text{ cm}^{-2}$ at 490°C , corresponding to a coverage Θ_{ad} of adatoms of 0.0004 ML. This can be compared to a value of 0.001 ML for (001) GaAs at this temperature, based on recent measurements for which an activation energy to adatom coverage of 2.7 eV is found, and Θ_{ad} is 0.07 ML at 580°C [63]. We therefore conclude that in addition to predicting the correct time- and length scale-dependence of the surface roughening during InGaAs growth, this model can also account for the magnitude of the roughness, using reasonable values for the parameters D and n_0 .

4.5 Effect of Growth Conditions on Surface Crosshatch

In this section we use the model developed in Section 4.2 to interpret measurements of the crystallographic anisotropy of the surface roughening during strained InGaAs growth, and to examine the effect of growth temperature and indium content on the morphology

dynamics. Consistent with the result that the q dependence of the surface morphology is best described by the EW form of Eq. 4.26, we will take K to be zero in the simulations.

4.5.1 Effect of Crystallographic Anisotropy

Orthogonal directions in III-V semiconductor crystals are not equivalent. This results in anisotropies in surface diffusion on the (001) GaAs surface for example, and differences in the activation barriers for dislocation motion associated with strain relaxation in the two $\langle 110 \rangle$ directions [53, 61, 64].

In order to study the crystallographic anisotropy in the strain relaxation and surface diffusion processes during strained-layer growth, light scattering measurements were made during $\text{In}_{0.18}\text{Ga}_{0.82}\text{As}$ growth using the configuration where the light is incident normal to the substrate. The results obtained along the $[1\bar{1}0]$ direction during this growth were presented in Fig. 4.5. We use the same normalization and curve-fitting procedure to analyze the light scattering measurements obtained simultaneously in the $[110]$ direction, which are presented in Figure 4.7. The weak oscillation in the scattered intensity at the beginning of the growth of the InGaAs, is a thin film interference oscillation due to the different index of refraction of the InGaAs compared with the GaAs substrate. The results of the model simulation are given in Table 4.1.

Although the fits in Fig. 4.7 are fair, the model cannot reproduce the difference in the onset of roughening at the two different spatial frequencies. It is likely that the thickness dependence of the misfit strain is not adequately accounted for by the simple

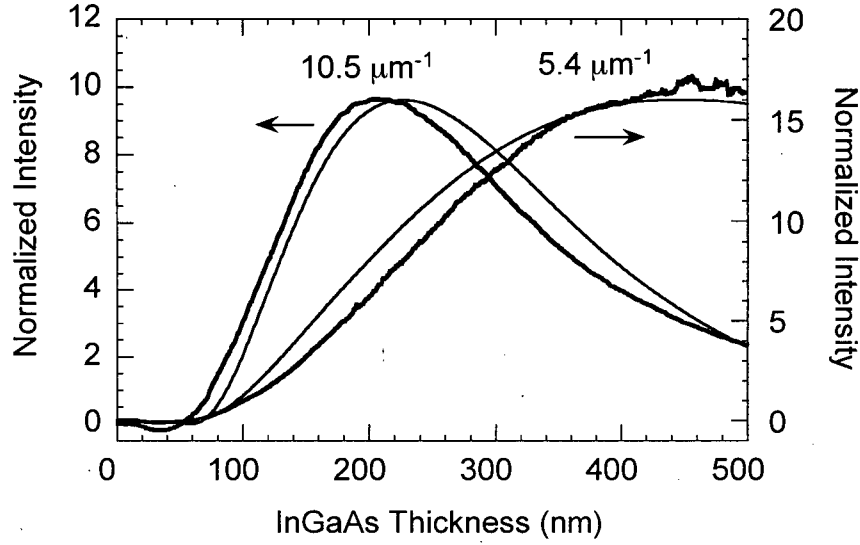


Figure 4.7: Light scattering data (thick lines) obtained along the $[110]$ direction during the same InGaAs growth experiment as in Fig. 4.5, and simulation results (thin lines) using $\nu = 1.1 \times 10^{-13} \text{ cm}^2/\text{s}$.

$1/z$ law used in the model. As shown in Table 4.2 this law is reasonably consistent with the relaxation in the $[1\bar{1}0]$ direction, but not for the $[110]$ direction. In order to obtain a better approximation to the initial strain relaxation rate, the X-ray data in Table 4.2 are fit to a power law of the form: $\bar{\epsilon} = (z_c/z)^p$. The resulting values for z_c and p are 49 nm and 0.7 for relaxation in the $[1\bar{1}0]$ direction, and 56 nm and 0.5 for the $[110]$ direction. Fits to the *in situ* light scattering data along both $\langle 110 \rangle$ directions, based on these power-law fits to the X-ray data, are shown in Figure 4.8. Here, $\bar{\epsilon}_{\text{eff}}$ in Eq. 4.26 is calculated explicitly using Eq. 4.22, and the approximations of Eq. 4.29 are not used. The results of the simulations are summarized in Table 4.1. Note that apart from the scale factor A , the only fitting parameter for these simulations is the constant ν .

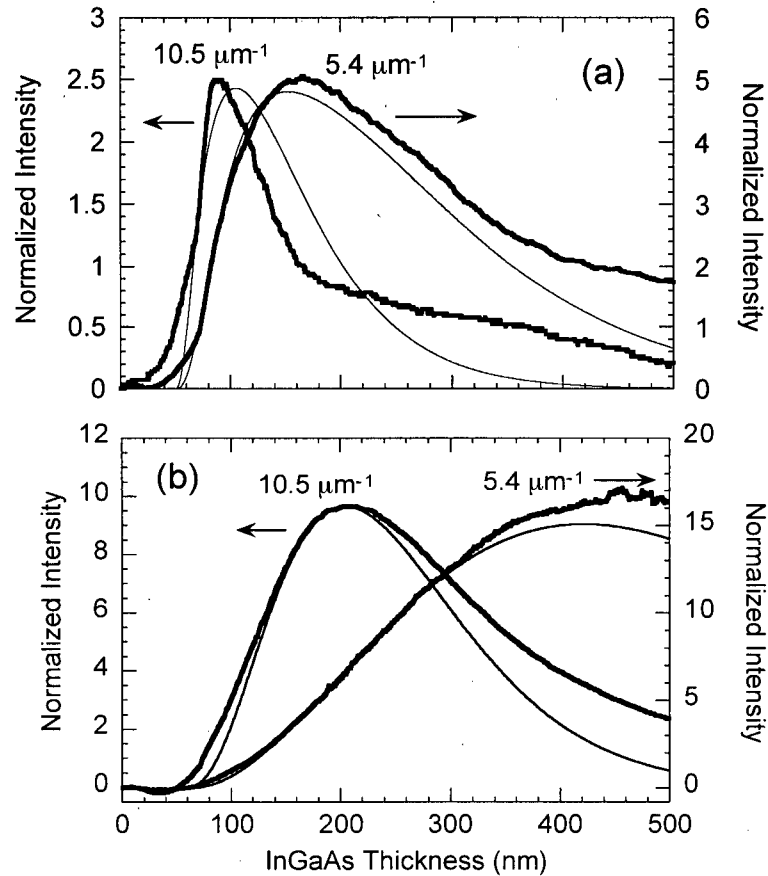


Figure 4.8: Simulations of the roughening along the $[1\bar{1}0]$ direction (a) and the $[110]$ direction (b), obtained using empirical fits to the anisotropic strain relaxation data from X-ray measurements.

The fit in Fig. 4.8(a) along $[1\bar{1}0]$ is similar to that in Fig. 4.5(a) obtained with the $1/z$ law, however the fit along $[110]$ is significantly improved using the experimentally determined strain relaxation. Also the values of R shown in Table 4.1 have been reduced in both cases to within the experimental uncertainty. The values of ν used in the fits have increased by a factor of about 2.5 relative to those obtained with the $1/z$ law, however the anisotropy in ν is essentially unchanged. The values of ν obtained using the $1/z$ law

are smaller since this parameter was adjusted to compensate for the fact that the film relaxation occurs at a slower rate than the assumed $1/z$ dependence. We find that ν is an order of magnitude higher along the $[1\bar{1}0]$ direction compared to the $[110]$ direction. This anisotropy is also observed during homoepitaxy on GaAs [65, 66]. Note that the mounds associated with the GaAs buffer layer growth are elongated along the high ν direction.

The normalized scattering intensity at both spatial frequencies is higher along the $[110]$ direction than the $[1\bar{1}0]$ direction, by a factor of 3.5. Accounting for the anisotropy in the initial scattering signal from the buffer layer, which is expected to be a factor of 3 higher along $[110]$ at these spatial frequencies according to the *ex situ* light scattering results in Section 2.3.4, the actual scattering intensities are estimated to differ by a factor of about 10. This agrees within a factor of 2 with the ratio of the unscaled peak intensities from the model. Thus it is not necessary to rescale the prefactor A in order to account for the anisotropy in the scattering intensities. Allowing for a factor of 5 experimental uncertainty in the relative peak intensities, this implies that the diffusion constant D in the 2 directions differs by no more than a factor of 3. The anisotropy in ν can therefore be attributed mainly to the factor β in Eq. 4.31, associated with the difference in adatom attachment probabilities for up-step and down-steps.

4.5.2 Effect of Growth Temperature and Lattice Mismatch

In Figure 4.9 we show fits to light scattering data obtained during growths of $\text{In}_{0.18}\text{Ga}_{0.82}\text{As}$ on GaAs at different temperatures. The measurements were made at a spatial frequency of $16\ \mu\text{m}^{-1}$ using the scattering configuration where light is incident through an effusion cell port. The signals have been scaled to unity at their peaks in this figure. The unscaled peak intensities $I_{16,\text{norm}}$ (normalized to the buffer layer scattering) are given in Table 4.3. Curves *a* and *c* correspond to signals monitored along the $[110]$ direction during growths at 515°C and 452°C , respectively. Curve *b* was obtained along the $[\bar{1}\bar{1}0]$ direction at 430°C (the gap in the data near the peak intensity is due to saturation of the detection electronics). Because the rate of strain relaxation is not known for these growths, a $1/z$ strain law was used in fitting all three curves. The results of the fits are given in Table 4.3, along with the results from Table 4.1 for the growth at 490°C (obtained using the $1/z$ law). The curves are each scaled to match the experiment in Fig. 4.9. The scale factor for the growth at 452°C is higher by a factor of 2.5 relative to the growth at 515°C monitored in the same direction at the same spatial frequency. This is consistent with a reduction of the prefactor A with temperature.

The fitted critical thickness decreases with increasing temperature. This result is to be expected if the misfit dislocation formation is kinetically limited; as the temperature is increased the elastic strain and misfit density will be closer to the equilibrium values. The parameter ν depends strongly on the growth temperature. Assuming that the temperature dependence arises from a thermally activated process, we find an activation

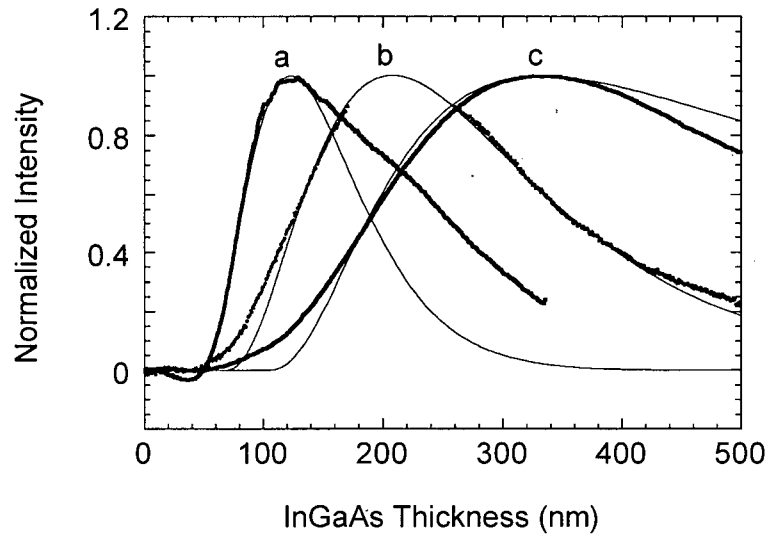


Figure 4.9: Light scattering signal at $16 \mu\text{m}^{-1}$ (thick lines) and simulation (thin lines) for $\text{In}_{0.18}\text{Ga}_{0.82}\text{As}$ growth at different temperatures. Curves *a* (515°C) and *c* (452°C) are taken along the $[110]$ direction and curve *b* (430°C) is along $[1\bar{1}0]$.

	Direction	T ($^\circ\text{C}$)	z_c (nm)	ν ($\times 10^{-12} \text{ cm}^2/\text{s}$)	$I_{16,\text{norm}}$
Fig. 4.9 <i>a</i>	$[110]$	515	45	0.19	5.5
Fig. 4.7		490	55	0.11	(10)
Fig. 4.9 <i>c</i>		452	100	0.008	9.7
Fig. 4.5a	$[1\bar{1}0]$	490	45	1.25	(2.5)
Fig. 4.9 <i>b</i>		430	65	0.04	3.6

Table 4.3: Model parameter values and experimental peak intensities at $16 \mu\text{m}^{-1}$ for InGaAs growths at different temperatures. Peak intensities in parentheses obtained at $10.5 \mu\text{m}^{-1}$.

energy of $2.5 \pm .5$ eV for ν , along both $\langle 110 \rangle$ directions. According to Eq. 4.31, the activation energy of ν will be the sum of the activation energies of β , D , and n_0 , none of which have been measured for this system. It is therefore difficult to interpret the activation energy of ν in terms of any specific physical process. Moreover, it is likely that part of the temperature dependence of ν obtained from the simulations, is in reality due to the temperature dependence of the relaxation rate, as we discuss at the end of this section.

In Figure 4.10 and Figure 4.11, we show experimental and calculated roughness data during growth of three $\text{In}_x\text{Ga}_{1-x}\text{As}$ layers of differing indium content ($x = 0.23, 0.084$, and 0.063), all grown at a temperature of 490°C . The scattering signals correspond to surface roughness at $16 \mu\text{m}^{-1}$ along the $[1\bar{1}0]$ direction. All of the experimental data in Fig. 4.10 were first normalized to the background scattering from the buffer layer at the start of InGaAs growth and then the background scattering was subtracted. In the case of the 6.3% In sample a background of slightly less than unity was subtracted. The thickness for the onset of roughening increases as the In content and lattice mismatch is reduced, as expected.

The model curves in Fig. 4.11 were calculated using $\nu = 0.6 \times 10^{-12} \text{ cm}^2/\text{s}$, which was selected to match the data for the sample with 8.4% In content. The critical thickness z_c was used as a fitting parameter, and values for the initial misfit f corresponded to the experimental In contents in each case ($f = 0.017, 0.0061$, and 0.0046 in order of decreasing In content). The prefactor A is the same for all three curves. The difference

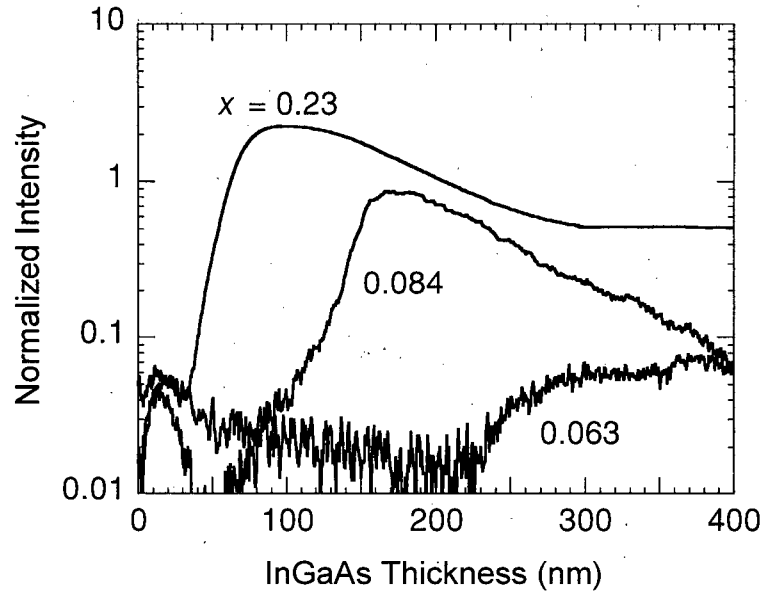


Figure 4.10: Scattered light intensity measured along $[1\bar{1}0]$ at $q = 16 \mu\text{m}^{-1}$ during $\text{In}_x\text{Ga}_{1-x}\text{As}$ growth with three different In concentrations as indicated.

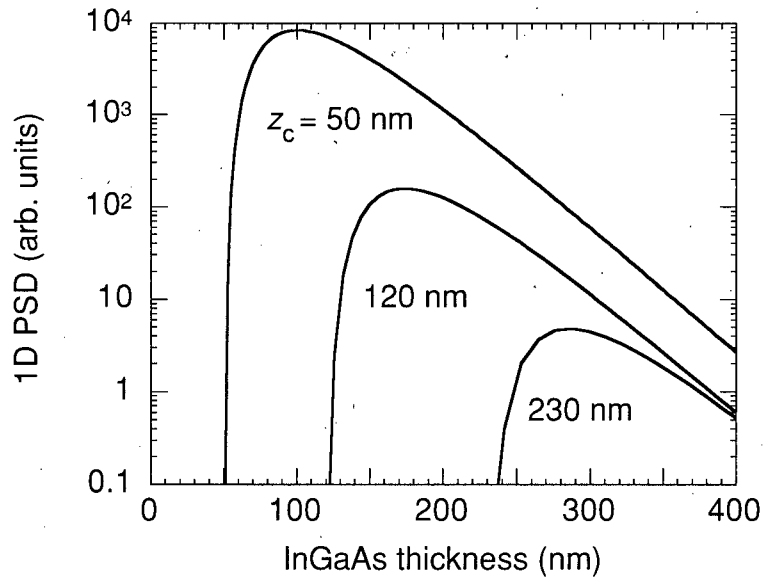


Figure 4.11: Simulated time evolution of the PSD calculated using $\nu = 0.6 \times 10^{-12} \text{ cm}^2/\text{s}$ and three different values of the critical thickness as indicated.

in the relaxation thicknesses for the 6.3% and 8.4% samples is large compared with what one would expect from the difference in the nominal In contents. Although the model can reproduce the general trend of lower scattering at lower In concentrations and larger critical thicknesses, the model predicts a much larger change in the intensity than is observed experimentally. This could be explained by a change in A or ν with In content. Both of these parameters depend on the surface diffusion constant and adatom concentration.

All of the simulations in this section were performed using a simple $1/z$ law to model the thickness dependence of the misfit strain, which is expected to be valid if the film is in equilibrium. In order to account for kinetic limitations to strain relief, the critical thickness was left as a fitting parameter. In reality, the rate of dislocation formation as well as the critical thickness are both affected by kinetics. According to the model of Dodson and Tsao, the rate of strain relief depends nonlinearly on the residual strain in the film, as well as on activation barriers to dislocation motion, and involves several parameters whose values must be determined from experiment [50]. Therefore the rate at which dislocations form during growth will depend both on growth temperature and on indium content, which determines the misfit strain. Deviations from the $1/z$ law resulting from kinetic limitations will have a significant effect on the surface roughening, as shown in Section 4.5.1. In particular the fitted value of ν will be smaller, in order to compensate for the slower rate of strain relief.

4.6 Summary

The development of the surface crosshatch pattern associated with strain relaxation by misfit dislocation formation, has been simulated using a continuum growth model. In this model, strain field gradients arising from the misfit dislocations act as a driving term for surface diffusion. The predictions of the model are compared to *in situ* light scattering measurements of the surface roughening during growth of strained $\text{In}_x\text{Ga}_{1-x}\text{As}$ on GaAs, as well as with more extensive *ex situ* light scattering measurements performed after growth. It is found that the Edwards-Wilkinson form of the model (ie. $K = 0$) is able to account for both the time- and spatial frequency-dependence of the surface morphology.

Using the model, it is possible to extract quantitative information on surface growth parameters from the light scattering signals. For example the parameter ν , which controls the rate at which local surface slopes are reduced during film growth, is found to be an order of magnitude higher along the $[1\bar{1}0]$ direction compared to the $[110]$ direction. By contrast no significant anisotropy in the surface diffusion constant D is observed. The crystallographic anisotropy in ν is attributed to differences in adatom step-attachment probabilities in the two directions.

The values of the model fitting parameters are sensitive to deviations in the film strain from equilibrium, caused by kinetic limitations. In most of the fits in this chapter a $1/z$ -dependence was used to model the thickness dependence of the misfit strain, and the critical thickness was adjusted to account for kinetic effects. In order to treat the strain kinetics more accurately additional fitting parameters would be required. Since

the fits at different spatial frequencies are constrained to the same parameter values, it should be possible to use the model to determine the thickness dependence of the strain, if measurements at several different spatial frequencies were obtained during growth.

Chapter 5

Coherent Islanding, Quantum Dots, and Ostwald Ripening

In Chapter 4 the relaxation of misfit strain through the introduction of interfacial dislocations was discussed. In this chapter we investigate an alternative path to strain relief which is often observed during growth in which the film is subject to a large compressive misfit strain. This process is characterized by the spontaneous formation of coherent three-dimensional islands. In contrast to the one-dimensional ridges that develop as a byproduct of plastic strain relaxation, the coherent islands are themselves responsible for strain relief, which they achieve elastically by virtue of their shape.

Coherent islanding occurs in many heteroepitaxial semiconductor systems, including group-IV [67], III-V [21], II-VI [41] and IV-VI [68] systems. The islands are defect-free and self-limited in size, making them attractive for use in optoelectronic devices. In particular this growth mode has received intense interest as a route to obtaining quantum dot (QD) arrays in a single growth step, without need for wafer patterning.

This is achieved by embedding the islands in a matrix of higher bandgap material, so that quantum confinement of electrons and holes in all three dimensions results [69]. Here we explore the dynamics of island growth in the most technologically promising system, namely InAs islands grown on the (001) GaAs surface. True 3D confinement effects have been demonstrated [70] in the InAs/GaAs system, and have recently been exploited in quantum-dot lasers [27].

The solution to the problem of how to achieve reproducible, high density arrays of uniformly-sized QDs, as required for technological applications, requires a better understanding of the growth process [70, 71]. In particular, a critical processing step occurs during the growth interrupt immediately following deposition of the strained material. For the case of QD growth in the InAs/GaAs system, the indium flux is interrupted after a prescribed amount of InAs has been deposited, and the island distribution evolves in a manner dependent on the InAs coverage, substrate temperature and arsenic overpressure, before being capped with a layer of the wider-bandgap GaAs material to form QDs. In what follows we will refer to the coherent islands as QDs, even in the absence of a GaAs capping layer. Under certain growth conditions a brief interrupt can result in significant narrowing of the island size distribution [70]. More generally a bimodal size distribution develops, consisting of small coherent islands (QDs), and larger islands that contain strain-relieving dislocations, and are not self-limited in size [20, 21, 72]. We will show that during annealing these dislocated islands grow, initially by consuming material from the QDs, and then through a ripening process where larger dislocated islands grow at

the expense of smaller dislocated islands. These processes are sensitively dependent on growth conditions, making it difficult to obtain reliable time-evolution information based on *ex situ* characterization of sequential runs. The problem is compounded by the fact that the island distribution can evolve considerably in a few seconds, so it is generally not possible to controllably freeze-in the surface morphology for *ex situ* analysis.

In this chapter we present *in situ* ultraviolet light scattering (UVLS) measurements performed during annealing of InAs islands grown on (001)-oriented GaAs substrates. The light scattering apparatus is described in Chapter 3. We find that high sensitivity to small length scale roughness as provided by UVLS is crucial in detecting the roughness associated with QD formation, above the background roughness of the substrate. In addition to providing instantaneous time-evolution information, UVLS can be used to obtain information about the effect of growth conditions, during a single MBE run. This is achieved by thermally evaporating the InAs material after each growth experiment, so that another experiment can be performed on the same substrate.

5.1 Stranski-Krastanow Growth in the InAs/GaAs System

The mode by which a film grows is affected both by the lattice mismatch and the interfacial energy between the materials [50]. If the interfacial energy and the lattice mismatch are both low, then two-dimensional (2D) layer-by-layer growth can occur, known as Frank-Van der Merwe growth. This applies to homoepitaxy, and also to the slightly strained InGaAs/GaAs films discussed in Chapter 4. If the interfacial energy is high, the

Volmer-Weber growth mode is favoured, in which three-dimensional islands form and coalesce as deposition continues. A third possibility, which prevails in the case of InAs growth on GaAs where the mismatch is high (7%) but the interfacial energy is low, is the Stranski-Krastanow (S-K) growth mode. This mode is characterized by a transition from 2D layer-by-layer growth to 3D island growth, as we now describe.

Due to its low surface energy relative to that of GaAs, the first monolayer of InAs will form a 2D wetting layer that is coherent with the substrate lattice [73]. This layer is only free to relax in the direction perpendicular to the surface, and is compressively strained in the in-plane directions. Once deposition proceeds beyond a critical thickness, the increasing elastic strain energy in the film drives a morphological transition in which 3D islands form on the wetting layer. Although their formation results in an increase in the total surface area of the film, there is a net reduction in the total strain energy. The free-standing islands can relieve a greater portion of the elastic strain relative to a 2D film, since they are only constrained against in-plane relaxation at their base. Above the critical thickness, the reduction in strain energy associated with the island formation is greater than the surface energy increase. The thickness at which this transition occurs for InAs growth on GaAs, is approximately 1.6 ML [74].

The precise nature of the self-limiting mechanism for QDs is a current issue in the literature. According to theory, the minimum-energy QD shapes are pyramidal and truncated pyramidal islands [73]. Such faceted structures are observed experimentally in the Ge/Si and InAs/GaAs systems. Depending on the interplay between strain reduction

and surface energy increase associated with the island facets, it is possible to have a minimum in the chemical potential for a given island shape, corresponding to an equilibrium island size [75, 67]. As mentioned above, a bimodal size distribution is often obtained in practice. In the Ge/Si system, this has been linked to a discontinuous shape transition with island size [18, 67]. Shape transitions are also observed for InAs dots [43, 72], however the bimodal size distribution in this case is associated with the appearance of dislocated islands as we discuss further below [20, 21, 72]. The fact that the partially-relaxed, dislocated islands ripen during annealing, supports the premise that the QDs are self-limited due to strain.

5.2 Real-Time Monitoring Experiments

InAs quantum dot growth and real-time light scattering experiments were carried out in the MBE deposition chamber using the setup described in Section 3.3, in which roughness at three spatial frequencies could be monitored simultaneously. For consistency, the plane of incidence was aligned approximately with a $\langle 100 \rangle$ direction in the plane of the substrate for each growth experiment, however based on AFM analysis of the samples the scattering signal during dot growth is expected to be isotropic.

5.2.1 Substrate Preparation

The GaAs substrates were prepared for the quantum dot growth experiments by *in situ* desorption of the oxide followed by growth a GaAs buffer layer, as described in Chapter 2.

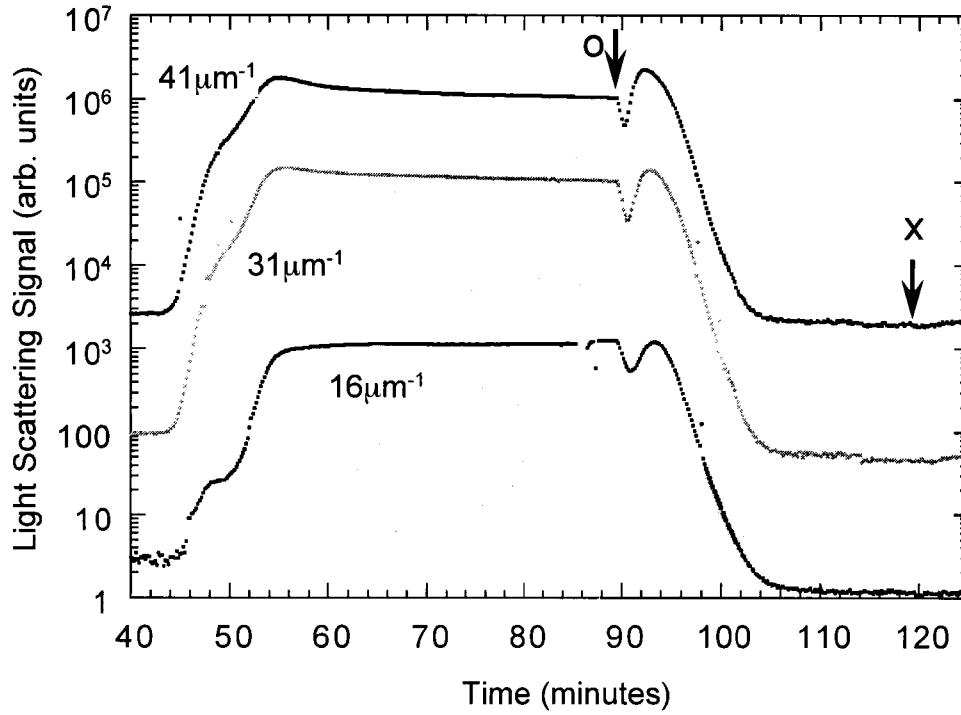


Figure 5.1: Light scattering signals at 16, 31 and 41 μm^{-1} , monitored simultaneously during thermal oxide desorption and GaAs buffer layer growth, both performed at 600 °C. The buffer layer growth begins and ends at the times indicated by the arrows marked “o” and “x” respectively.

The time-evolution of the three scattering signals is shown in Figure 5.1 for a typical oxide desorption and buffer layer growth, performed prior to a quantum dot growth experiment. The signals, which have been spaced apart vertically for clarity, monitor roughness at spatial frequencies q of 41 μm^{-1} , 31 μm^{-1} , and 16 μm^{-1} , corresponding to lateral length scales of 154 nm, 205 nm, and 393 nm respectively. The starting signal at each spatial frequency represents the sum of the scattering from the GaAs substrate, and any stray background light. The initial large increase in scattering intensity corresponds to the thermal desorption of the oxide. As discussed in Section 2.3.3, this is accomplished by

heating the wafer to 600 °C under As₂ overpressure, and results in a pitted surface. The substrate temperature was held fixed throughout the oxide desorption and for the first 20 minutes of the GaAs buffer layer growth. We note that the signals increase by three orders of magnitude during the desorption procedure. During the subsequent annealing of the surface, the two higher q signals drop whereas the $16\text{ }\mu\text{m}^{-1}$ signal remains constant. This behavior indicates that the surface is smoothing on short length scales, by faceting of the pits for example, but that the large length scale structure is not changing. The arrow marked "o" in Fig. 5.1 indicates the time at which the shutter for the Ga effusion cell was opened to commence growth of the buffer layer. The signal at each spatial frequency initially drops and rises before decaying monotonically. This initial oscillatory behavior is not seen in all of our buffer layer growths, and is believed to be associated with the presence of residual contamination on the growth surface following the oxide desorption procedure [34]. We note that the higher q signals are especially sensitive to this effect. A $0.5\text{ }\mu\text{m}$ thick buffer layer was grown at a rate of $1\text{ }\mu\text{m/hr}$, during which the surface roughness dropped to the level of the starting substrate over the spatial frequency range of interest. During the final ten minutes of buffer layer growth the substrate temperature was ramped down to below 500 °C in preparation for the InAs deposition. The Ga shutter was closed at the time indicated by the arrow marked "x".

5.2.2 Quantum Dot Growth

Following termination of the GaAs buffer layer, a 5 to 10 minute growth interrupt was typically required immediately prior to the dot growth to allow the arsenic flux and substrate temperature to stabilize at the desired settings. The As₂ overpressure at the substrate was inferred from the background pressure in the growth chamber measured by an ion gauge, and is estimated to be accurate to a factor of 3. The temperature as monitored by diffuse reflectance spectroscopy (DRS) was held fixed throughout the InAs deposition and subsequent annealing. For the experiments discussed here, nominally 3 monolayers of InAs were deposited at a growth rate of ~ 10 ML/min, under an As₂ overpressure at the substrate of $\sim 5 \times 10^{-7}$ mbar. These values for the growth rate and arsenic pressure are smaller by a factor of about 6 and 10 respectively, compared to those used in the growth of the GaAs buffer layer, and in the In_xGa_{1-x}As growths in Chapter 4. The effect of variations in InAs coverage and arsenic overpressure are explored in Section 5.5.

In addition to the three light scattering signals, RHEED was used to monitor the 2D to 3D transition associated with the quantum dot formation. The onset of quantum dot formation is signaled by the transition from a streaky RHEED pattern associated with a 2D growth front, to a spotty pattern indicative of 3D growth [42].

The time-evolution of the scattering signals during a series of quantum dot growth and annealing experiments is shown in Figure 5.2. These signals were acquired following a 10-minute growth interrupt, during the same MBE run for which the the buffer layer

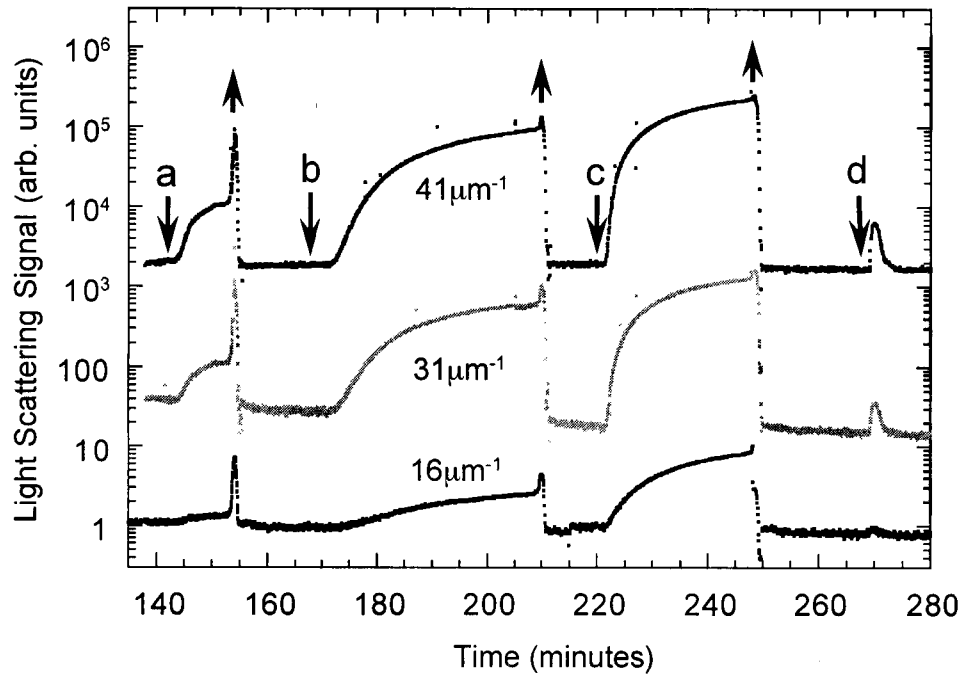


Figure 5.2: Light scattering signals acquired during 4 separate InAs quantum dot growth experiments, during the same run and sharing the same time-axis as Fig. 5.1. The downward-pointing arrows (*a, b, c* and *d*) indicate the times at which 3 ML of InAs was deposited, at different substrate temperatures as discussed in the text. The InAs was evaporated between experiments, at the times indicated by the upward-pointing arrows.

growth was described in Section 5.2.1. The initial intensity at each spatial frequency is the sum of any stray background light that enters the solid angle of each detector, and the scattering signal associated with the buffer layer roughness. The arsenic overpressure was held fixed throughout each experiment as discussed above. The indium shutter was opened for a period of 18 s at each of the times indicated by downward pointing arrows in the Fig. 5.2, so that 3 ML of InAs were deposited in each case. The InAs was evaporated between experiments by heating the substrate to over 500 °C, at the times indicated by upward pointing arrows. Following the InAs evaporation, a 2D RHEED pattern was

recovered and the scattering signals decayed back to their initial values. The arsenic pressure was increased by approximately an order of magnitude during the evaporation step, to ensure that decomposition of the GaAs surface did not occur.

The InAs deposition indicated by the letter *a* in the Fig. 5.2 was performed at a temperature of 440 °C. In this instance the substrate heater power was shut off immediately following the InAs deposition, so that the substrate temperature dropped to below 300 °C within 3 minutes according to DRS. The increase in the light scattering signals indicates that the film morphology changes rapidly as the substrate cools. It is therefore not possible in these experiments to study the initial stages of the quantum dot growth by *ex situ* analysis of quenched samples. Once the signals had stabilised the InAs was evaporated in preparation for the next deposition experiment, using the procedure described above. The following two growths, indicated by *b* and *c* in Fig. 5.2 were performed at 280 °C and 400 °C respectively. In these experiments the substrate temperature was held fixed following the InAs deposition, in order to study the effect of annealing. The initial increase in the scattered light intensity is associated with QD formation and the subsequent appearance of larger islands. The continued increase observed during the late stages of annealing is attributed to Ostwald ripening of the larger islands, as we discuss further below. The signals evolve more rapidly when the annealing temperature is higher, and the increase is larger at the higher spatial frequencies. The increase is even more dramatic during the evaporation step when both the temperature and arsenic overpressure are increased. As shown below, the rate at which the large islands grow and ripen increases with both

arsenic pressure and annealing temperature. It is interesting that the peak scattering intensity reached during the evaporation step following each experiment is nearly the same, despite the difference in the initial signals before the evaporation. This might be expected if the main effect of the change in annealing conditions was to change the rate at which the island distribution evolves. For the experiment indicated by the letter *d*, a growth temperature of 490°C was used. In this case, the signals rise rapidly and decay back to their initial levels, indicating that the temperature was sufficiently high that the InAs evaporated during the deposition and annealing. No subsequent evolution of the signals was observed during the high-temperature evaporation step for this experiment.

Finally we note that although the background signal at $41\ \mu\text{m}^{-1}$ and $16\ \mu\text{m}^{-1}$ is relatively stable, the signal at $31\ \mu\text{m}^{-1}$ decays by a factor of 4 over the course of these experiments (2.4 hours). This is due to window coating at the effusion cell port used to collect this 250 nm wavelength signal, as discussed in Section 3.3. In the analysis that follows the light scattering signals are normalized to their initial values immediately prior to the InAs deposition. The small gradual decrease in background intensity during a single annealing experiment is negligible compared to the increase in signal associated with the island growth processes.

5.3 Results

AFM analysis of a film containing quantum dots and large islands has been presented in Section 2.3.6. Here we discuss the *in situ* light scattering measurements acquired

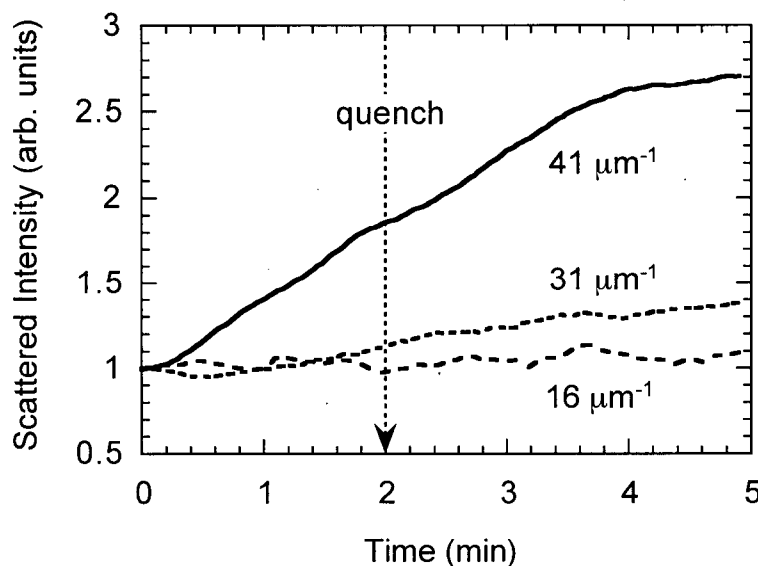


Figure 5.3: Time evolution of the light scattering signals during a quantum dot growth at 490°C, corresponding to the AFM image in Fig. 2.11. The indium deposition was terminated at $t = 0$, and the film was quenched at $t = 2$ minutes (indicated by dashed line in the figure). Each scattering signal is normalized to unity at $t = 0$.

during the growth of this film, and present additional AFM images that show how the dot distribution changes during extended annealing.

5.3.1 Light Scattering

In Figure 5.3 we show the time-evolution of the scattering signals during the growth of the sample shown in the AFM image in Fig 2.11. Based on the AFM structural analysis of this film discussed in Section 2.3.6, the PSD associated with the large islands in this film is an order of magnitude lower than that of the quantum dots, over the q -range accessible to the light scattering measurements. Thus the scattering from the

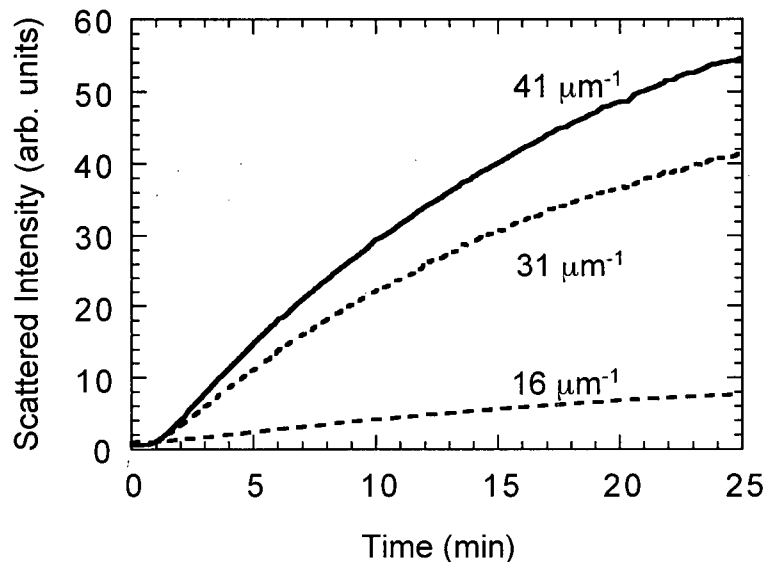


Figure 5.4: Light scattering signals (normalized to the initial scattering) corresponding the experiment in Fig. 5.2 (arrow c) in which the dots were grown and annealed at 400 °C

large islands is expected to make a negligible contribution to the total scattering signal in this case. We can therefore attribute the increase in the scattering signals during this experiment to the evolution of the QD distribution.

The signals in Fig. 5.3 have each been normalized at $t = 0$ to the initial scattering intensity, which is the sum of any stray background light and the signal from the GaAs buffer layer. The dots were grown and annealed for 2 minutes at a substrate temperature of 490 °C. Nominally 3 ML of InAs were deposited in 0.3 min, starting at $t = 0$. The 2D to 3D RHEED transition was observed at $t \sim 0.2$ min, which coincides with the onset of roughening observed in the light scattering at $q = 41 \mu\text{m}^{-1}$. By contrast the signal at $q = 16 \mu\text{m}^{-1}$ did not increase sufficiently throughout the entire anneal to be

discernible above the noise. This is consistent with the result from Section 2.3.6 that the PSD associated with the final dot distribution does not rise above the level of the GaAs buffer layer for spatial frequencies less than $\sim 25 \mu\text{m}^{-1}$. Following termination of the anneal (at $t = 2$ min) the sample was quenched under arsenic overpressure as described above. The continued increase in the light scattering signals indicates that the dots continued to evolve during the first 2 minutes of the quench, by which time the substrate temperature had dropped to 300°C as measured by DRS. It is interesting that InAs evaporation was apparently not significant during this growth, which was performed under nominally the same conditions as experiment *d* in Fig. 5.2, where the dots were seen to evaporate. Presumably this difference in behavior is due to run-to-run variations in growth conditions such as the arsenic overpressure.

For comparison, in Fig. 5.4 we show the normalized scattering signals obtained during the anneal at 400°C , indicated by letter *c* in Fig. 5.2.

5.3.2 AFM

In Figure 5.5 we show $2 \times 2 \mu\text{m}^2$ AFM images of quenched films grown under nominally the same conditions, but with different annealing times. A $20 \times 20 \mu\text{m}^2$ image of the film in Fig. 5.5(b) is shown in Figure 5.6. In the case of the film in Fig. 5.5(a), 3 ML of InAs were deposited and the film was annealed at 440°C for 3 minutes. The density of the QDs in this image is similar to that in Fig. 2.11 for the film annealed at 490°C . However larger-area AFM scans on this film did not reveal any of the large islands visible

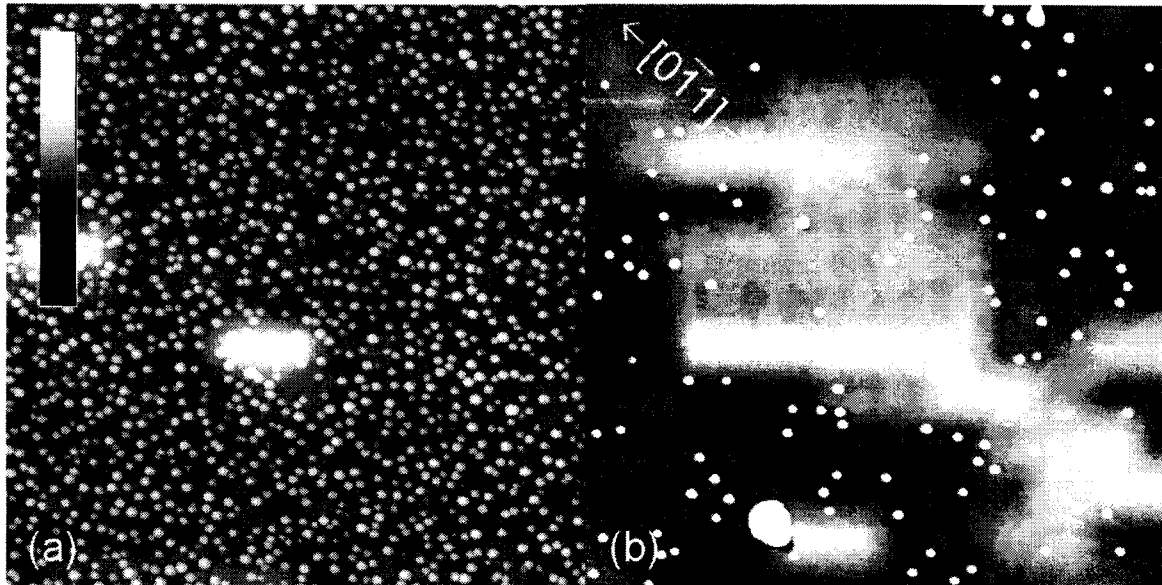


Figure 5.5: AFM images ($2 \times 2 \mu\text{m}^2$) showing the effect of annealing time on the island distribution. In both cases 3 ML of InAs were deposited at 440°C . (a) Quantum dot distribution after a 3 min anneal at 440°C (30 nm gray scale). (b) Image taken after a 25 min anneal at the same temperature, showing QDs and two large islands. The gray scale range in (b) has been reduced to 10 nm in order to reveal the underlying surface steps, so that the islands appear saturated white.

in Fig. 2.11. The dot distributions change considerably during extended annealing, as shown by the AFM image in Fig. 5.5(b). In this case the sample was annealed at 440°C for 25 minutes. The gray scale range in the image has been adjusted to reveal the atomic-height terraces of the substrate, so that the QDs appear saturated white. We note that the dot density has been reduced by approximately an order of magnitude in this film relative to the film annealed for only 3 minutes. The dots have approximately the same average size as those in Fig. 5.5(a), as expected for QDs. By contrast the size of the large islands has increased dramatically (typical height of 50 nm) compared

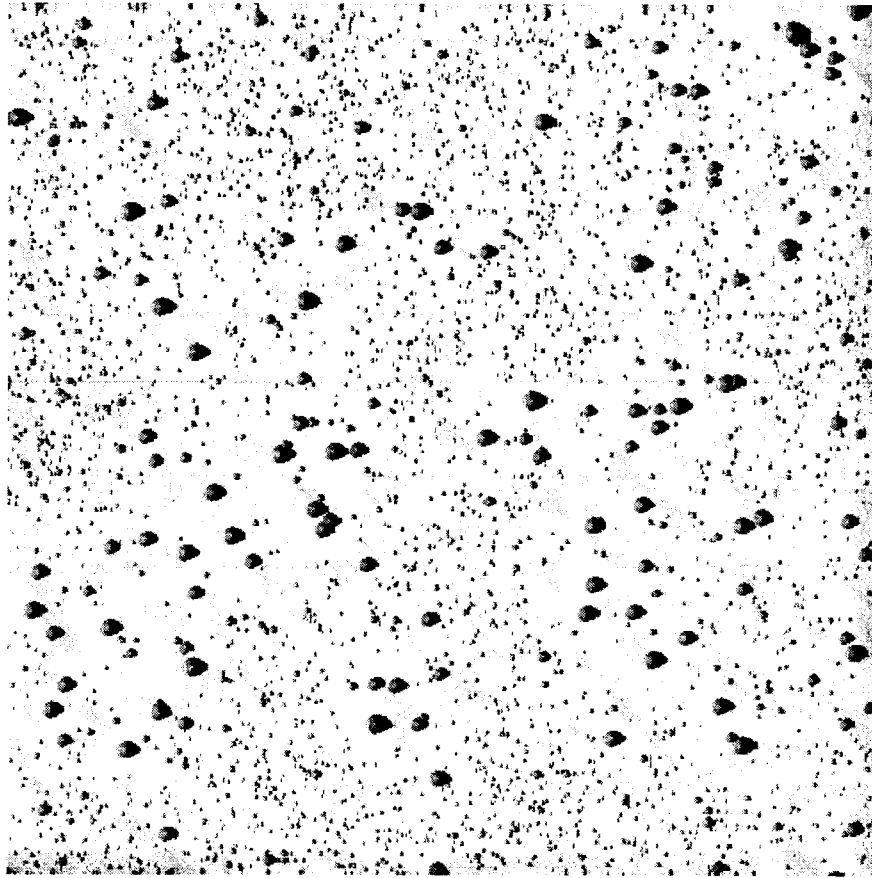


Figure 5.6: Large scale ($20 \times 20 \mu\text{m}^2$) AFM image of the film in Fig. 5.5(b), showing the spatial distribution of the QDs, the large islands, and the background texture of the buffer layer. The image is filtered to appear illuminated from the left. The $[1\bar{1}0]$ direction is oriented as in Fig. 5.5(b).

to those in Fig. 2.11. The large-scale scan in Fig. 5.6 shows that the large islands are inhomogeneously distributed across the substrate. Also apparent from Fig. 5.6 is that the density of the QDs is sharply diminished in regions where the large islands appear, which strongly suggests that the growth of the large islands proceeds at the expense of the QDs.

As discussed above, the increase in the light scattering signals in Fig. 5.3 for the film annealed for 2 minutes can be attributed to the evolution of the QD distribution alone, based on the AFM analysis in Section 2.3.6. We have also performed an analysis of the QDs and large islands for the film annealed for 25 minutes at 440°C. Based on the AFM image of this film (Fig. 5.6) we find that over the range accessible to the *in situ* measurements, the PSD of the large islands is $5 \times 10^4 \text{ nm}^4$. By contrast the contribution to the PSD from the QDs (which are approximately randomly-spaced in this case) is only 50 nm^4 . Thus the PSD associated with the large islands is three orders of magnitude higher than that of the QDs in this case. We conclude that during the late stages of annealing the light scattering signal is dominated by the contribution from the large islands.

5.3.3 Analysis of Light Scattering Data

In order to extract quantitative information from the *in situ* light scattering data, it is necessary to relate the signals to the surface structure of interest, namely the size and density of the islands. In the following discussion we will use the term “islands” as a

generic term for the large islands and the quantum dots together. From visual inspection of AFM images, the distribution of the islands does not appear to be correlated with the underlying surface structure of the GaAs buffer layer. In this case we can subtract the initial scattering signal from the signal during the island growth, in order to obtain the contribution to the PSD from the islands. As discussed in Section 2.3.6 the spatial distribution of the QDs is not perfectly random for the high dot densities considered here. Hence the PSD associated with the QDs will have a q -dependence determined in part by the spatial correlations in the positions of the dots. Once the large (and randomly-spaced) islands appear, they will dominate the signal as they grow in size and consume the dots, so that the signals should become q -independent in accordance with Eq. 2.10.

In Figure 5.7 we show the time dependence on a log-log scale of the three scattering signals from Fig. 5.4 for the anneal at 400 °C. Also shown is the data for a similar annealing experiment at 280 °C. These two data sets were obtained during the same MBE run, and correspond to the two experiments designated by b and c in Fig. 5.2 for the anneals at 280 °C and 400 °C respectively. Although all of the samples discussed here were prepared under nominally the same conditions, the growth conditions for these two experiments that were performed during the same run are likely to be much closer to being identical. Some run-to-run variations in As₂ over-pressure and In flux are inevitable. A time t_o has been subtracted from the time-axis of each curve in this plot, where t_o corresponds in each case to the time at which the 2D to 3D islanding transition was observed by RHEED during growth. The values for t_o are 0.3 min and 1 min for the

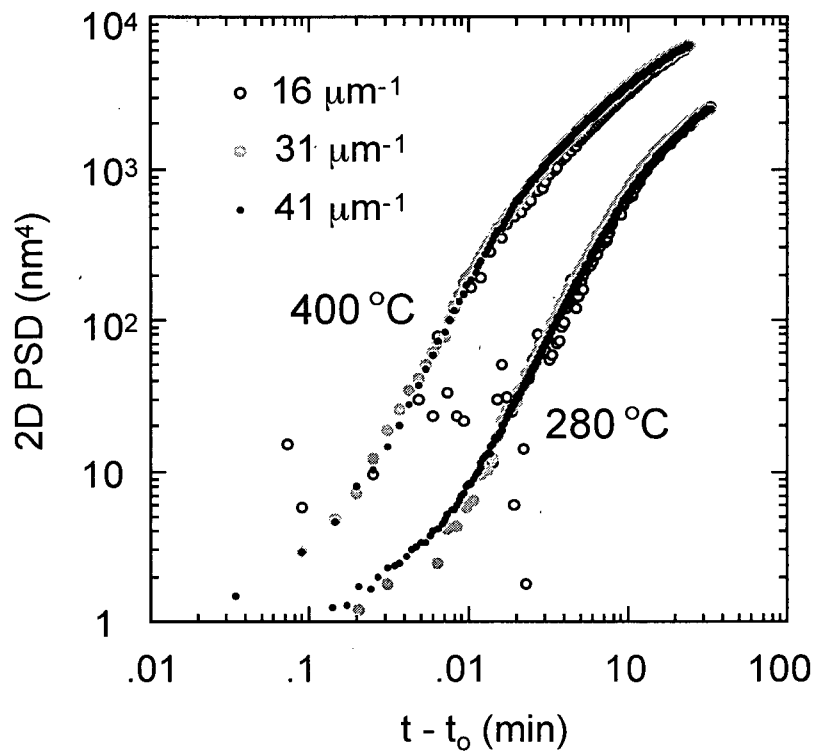


Figure 5.7: Comparison of the q -dependence of the scattering data in Fig. 5.4 for the 400°C growth and annealing experiment, and a similar experiment performed during the same MBE run at 280°C . The initial background scattering has been subtracted from the signals, which are normalized to coincide at the end of the anneal. The PSD has been calculated from the scattered light intensity based on an absolute calibration of the $41\ \mu\text{m}^{-1}$ signal as discussed in the text.

growths at 400 °C and 280 °C respectively. In order to isolate the time evolution of the islands from the total light scattering signal which includes the buffer layer, the initial scattering signal has been subtracted as discussed above. The signals are then normalized so that they coincide at the end of growth.

Based on an absolute calibration of the $41 \mu\text{m}^{-1}$ signal following the procedure discussed in Section 3.3 we have calculated the PSD from the scattered light intensity at this spatial frequency. This calibration, which is believed to be accurate to a factor of about two, could not be performed for the other two signals due to run-to-run variations in optical alignment. However the scale on the vertical axis should be correct for all three signals if the final PSD is q -independent, consistent with our AFM measurements on the large islands. We note that at long times when all three signals at different spatial frequencies are strong, there is no significant difference in the ratios of the three signals at either temperature as a function of time, indicating that the spatial frequency dependence of the PSD is not changing. This would be true if, for example, the spatial distribution of the islands was random and remained random during the annealing. From this and similar results obtained on other growths, we conclude that the signal at any q is proportional to $n\langle V^2 \rangle$ (see Eq. 2.10) throughout the late stages of the anneal, which we associate with the growth and ripening of the large islands. The signal to noise ratio in the data is not good enough to determine the time-dependence at each q during the initial stage, which we associate with the evolution of the quantum dot distribution before the large islands emerge.

We can further simplify the interpretation of the data if the relative size fluctuation of the islands, $\sigma_v/\langle V \rangle$ does not change with average island size [44], where σ_v is the standard deviation of the volume. In this case, Eq. 2.10 may be written,

$$g_{2D} \sim n(\langle V \rangle^2 + \sigma_v^2) \sim n(k + 1)\langle V \rangle^2 \quad (5.1)$$

where $k = (\sigma_v/\langle V \rangle)^2$ and the proportionalities may be replaced by equalities if the positions of the islands are uncorrelated. We have calculated the average dot sizes and variances using the height distributions from AFM discussed in Section 2.3.6, as well as those from a similar analysis of the large islands in Fig. 5.6. A conical dot geometry was assumed in all cases. We find that k is small (< 0.2) for both the QDs and the initial large islands in Fig. 2.11, consistent with a narrow size distribution. However the value of k associated with the large islands appears to increase at the late stages of annealing, to ~ 0.7 according to Fig. 5.6. This broadening of the relative size distribution reflects the inhomogeneity in the ripening process across the film, which is visible in the AFM image. In light of Eq. 5.1, the effect of assuming a constant k is to underestimate the volume during the final stages of ripening by a factor of about $(1.7/1.2)^{1/2} \sim 1.2$, which is negligible for the discussion here. Therefore the time-dependence of the light scattering signal after the large islands have nucleated is well approximated by

$$I(t) - I_o \sim g_{2D}(t) \sim n(t)\{\langle V \rangle(t)\}^2 \quad (5.2)$$

where $I(t)$ is the scattered light intensity, at any spatial frequency, and I_o is the initial scattering intensity.

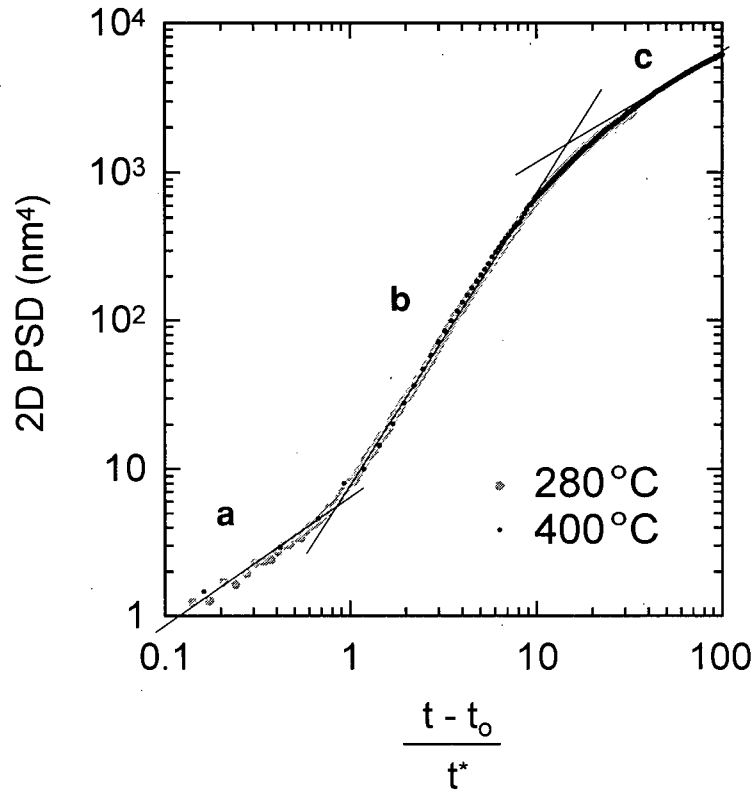


Figure 5.8: Collapse of the two data sets in Fig. 5.7, obtained by rescaling the time axis for each temperature. The times, t^* used to obtain the data collapse were 0.2 min and 1 min respectively for the films annealed at 400 °C and 280 °C. The three linear regions, which correspond to regions of distinct power-law behavior, have slopes of (a) 0.9, (b) 2.0, and (c) 0.75.

5.4 Discussion

The data in Fig. 5.7, acquired during two growths at considerably different temperatures (400 °C and 280 °C), display a time-dependence that is strikingly similar. The simplest interpretation is that the main effect of an increase in temperature is to increase the diffusion rate for atoms on the surface, thus rescaling the time for the island formation and

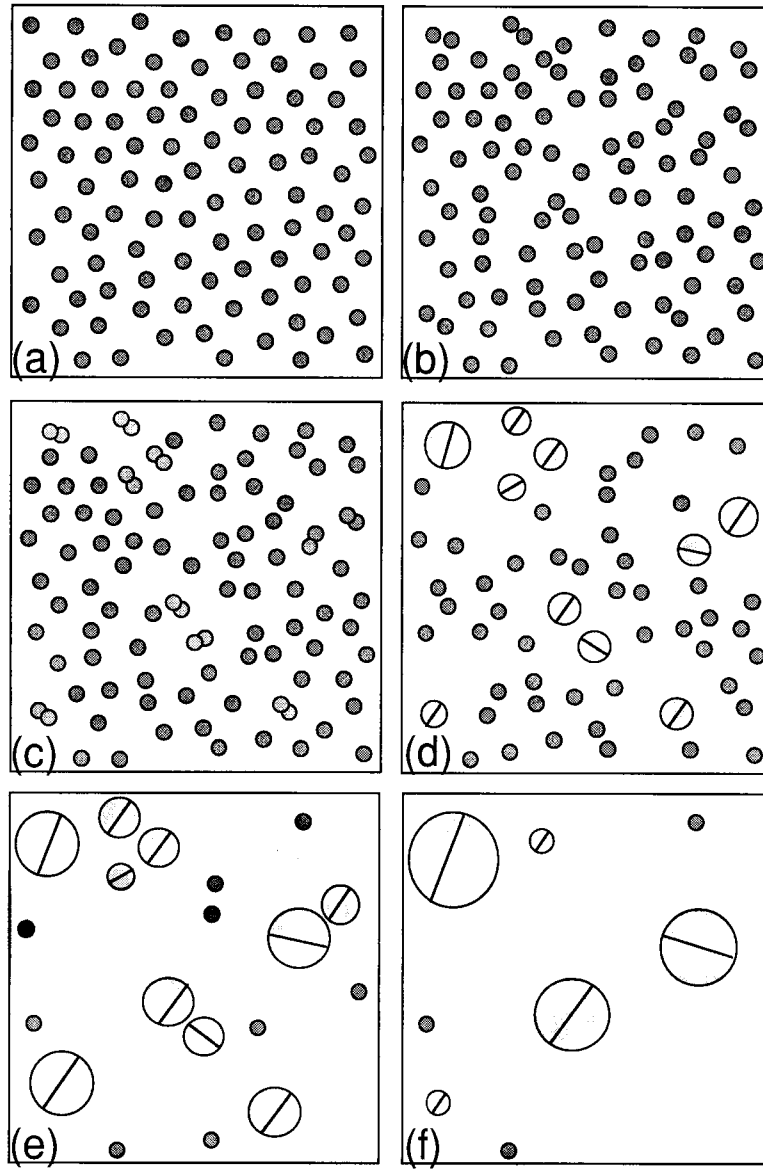


Figure 5.9: Evolution of the quantum dots and large islands during annealing. (a) Quantum dots nucleate on the surface. (b) The QDs diffuse randomly as they exchange atoms with the adatom population. (c) Quantum dots collide, nucleating larger defective islands. (d) The larger islands act as a sink for the constant supply of adatoms provided by the QDs. (e) The QD population is depleted. (f) The islands compete with each other for the remaining supply of adatoms, which diminishes with time as the average island size increases (Ostwald ripening).

growth processes. Accordingly in Figure 5.8 we have replotted the data corresponding to $q = 41 \mu\text{m}^{-1}$, using a normalized time axis. The two curves, obtained using normalization times, t^* of 1 min and 0.2 min for the growths at 280 °C and 400 °C respectively, are seen to coincide almost perfectly during the entire time of the anneal. This result is quite remarkable, given that other than t^* , there are no fitting parameters. We emphasize that in order to reproduce the growth conditions (other than the temperature) as closely as possible, both growths were performed on the same buffer layer during the same MBE run. The striking collapse of these two data sets supports the conclusion that given identical growth conditions, the effect of temperature on the dynamics of the island growth during annealing is simply to rescale the time axis. Three regions of distinct time-dependence emerge in Fig. 5.8, labeled *a*, *b*, and *c*, which exhibit different power-law behavior. We associate each of these regions respectively with the evolution of the initial distribution of QDs (*a*), growth of the large islands at the expense of the QDs (*b*), and Ostwald ripening of the large islands after the QD density has been substantially reduced (*c*). These processes are summarized in Figure 5.9, which we refer to in the following discussion.

5.4.1 Dot Diffusion

The initial time-dependence (region *a* of Fig. 5.8) is sensitive to the value of t_o . It was therefore necessary to adjust t_o in each case so that the initial behavior followed a power law (i.e. constant slope in Fig. 5.8); however as mentioned previously the fitted t_o was

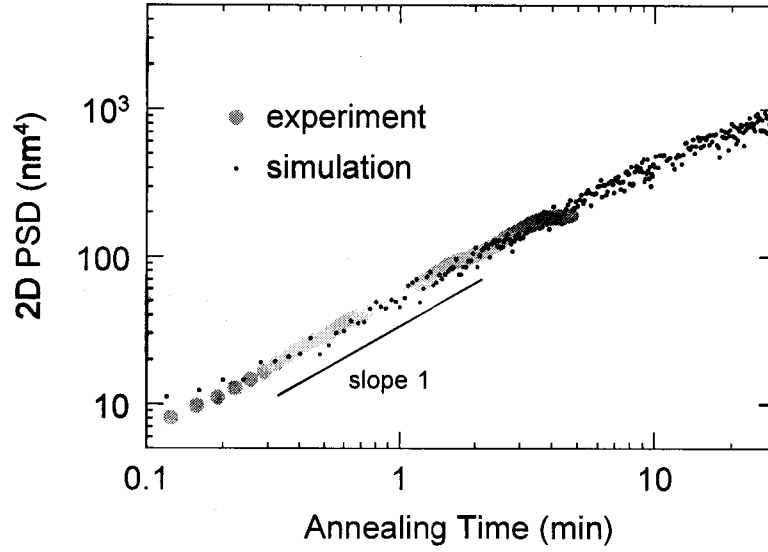


Figure 5.10: Time-evolution of the PSD at $41 \mu\text{m}^{-1}$ during the early stages of QD growth. Gray circles: PSD calculated from the $41 \mu\text{m}^{-1}$ signal in Fig. 5.3 after subtracting the background, plotted on a log-log scale. The time t_o is 0.2 minutes. Black circles: Simulation of the PSD, in which the QDs nucleate on a 58 nm pitch square grid and then diffuse on the surface during annealing as discussed in the text. The solid line has a slope of 1.

found in each case to match the time of the 2D-to-3D transition observed by RHEED. Using this procedure we find that the initial time-dependence is linear (slope 0.9 in Fig. 5.8).

Further evidence of this behavior is shown in the Fig. 5.10. Here we plot the $41 \mu\text{m}^{-1}$ signal from Fig. 5.3 on a log scale, using a t_o of 0.2 minutes in agreement with the RHEED transition. Again, we have subtracted the background scattering signal and calculated the PSD from this signal based on the calibration described previously. Based on this absolute calibration, the final value of the PSD at $41 \mu\text{m}^{-1}$ is 200 nm^4 . This is remarkably close to the value of 190 nm^4 , determined from the AFM analysis on the

quenched sample by summing curves *c* and *d* in Fig. 2.13. The time-dependence of the PSD, which is seen to be approximately linear throughout this experiment, is relatively insensitive to the choice of t_0 for times greater than 0.5 minutes. Furthermore, for this growth, the scattering from the large islands is expected to account for less than 10% of the total signal according to the AFM analysis. Therefore the order-of-magnitude increase in the PSD can only be attributed to the QD distribution. Hence we conclude that the initial increase in the PSD associated with the evolution of the QD distribution is approximately linear with time.

The size of the quantum dots in these growths is expected to saturate within ~ 10 s after nucleation, based for example on photoluminescence measurements [22] on capped dots, in which the duration of the growth interrupt before the capping layer deposition was varied. Since the driving force for the quantum dot nucleation, namely the supersaturation of InAs material, is removed as the dots grow, the quantum dot nucleation process is also expected to end within a time period of seconds. Therefore both the size and density of the QDs is not expected to change significantly during the initial period of annealing immediately following the nucleation of the QDs and before the emergence of the large islands.

In order to explain the initial linear increase in the scattering signal, we consider the possibility that the QDs are diffusing on the substrate. This is illustrated schematically in Figs. 5.9 (a) and (b). As discussed in Section 2.3.6 spatial correlations exist in the QD distribution. Therefore the contribution to the PSD at $41 \mu\text{m}^{-1}$ will change according to

the spatial distribution of the dots. Although no measurements of quantum dot diffusion have been reported previously, we note that island diffusion is known to occur on metal surfaces observed by *in situ* scanning tunneling microscopy, for island sizes exceeding 1000 atoms [76]. By comparison, the average size of a QD is $\sim 60\,000$ atoms, based on the AFM analysis in Section 2.3.6. Island diffusion can occur for example due to the random attachment and detachment of adatoms from the island periphery, in which case the center of mass of the island moves a distance on the order of R/N with each atom exchange event, where R is the island radius and N is the number of atoms in the island. Since the quantum dots are self-limited in size, the rate of atom detachment must precisely cancel the rate of attachment.

We have performed a simulation in order to determine the effect of dot diffusion on the measured scattering signal. The results of this simulation are shown along with the actual light scattering data in Fig. 5.10 obtained during the 490°C anneal. The density and volume of the dots used in the simulation were chosen to correspond to the values determined from the AFM analysis of the QDs in this film. The large islands were not included in the simulation consistent with the discussion above that their contribution to the PSD is negligible.

As mentioned above, the nucleation of a QD will depress the local InAs supersaturation, so that no new dots can nucleate within a diffusion length of the newly nucleated dot. The dot density in this film is such that the average spacing of the dots is only 58 nm, which is comparable to the average dot diameter. For such a high dot density

one would expect that the initial spatial distribution of the QDs upon nucleation will be strongly correlated as indicated in Fig. 5.9(a). For the purposes of the simulation we assumed that the dots all nucleate simultaneously on a square grid with a pitch of 58 nm, and that they grow instantly to their final volume. The initial PSD will therefore consist of a sharp peak at a spatial frequency of $108 \mu\text{m}^{-1}$, corresponding to the average spacing, so that no signal at $41 \mu\text{m}^{-1}$ is detected. In the simulation each dot (taken to be identical) executes a random walk starting at $t = t_o$, so that the spatial distribution becomes increasingly random with time. The signal at $41 \mu\text{m}^{-1}$ therefore increases as the dots diffuse and the peak in the PSD broadens. As confirmed by the simulation results in Fig. 5.10, this increase is initially linear in time. The simulated signal is slightly noisy, since it represents an average of 1000 simulations for an array of only 400 dots. In comparison the number of QDs within the 50 mm^2 illumination area of the light scattering measurement is $\sim 10^{10}$.

The only fitting parameter in the simulation is the diffusion constant D_{QD} of the quantum dots, which controls the rate of the linear increase in the signal. In order to match the light scattering data, we find that D_{QD} is $4.2 \times 10^{-15} \text{ cm}^2/\text{s}$, which corresponds to a dot diffusion length of 5 nm in one minute. In terms of the simple atom attachment/detachment mechanism discussed above, the average time between exchange events at each atomic site along the island periphery would be $\sim 50 \mu\text{s}$, considering that there are ~ 300 atoms on the periphery of a typical dot. We can make a rough self-consistency check by considering that immediately after each QD nucleates, the rate

of adatom detachment from the QD is expected to be small compared to the rate of attachment, until the QD approaches its self-limiting size. As an estimate of the net attachment rate during the QD growth we use a value of $(50 \mu\text{s})^{-1}$, consistent with the adatom exchange time obtained from the fit. Using this value we find that a QD will reach its final size (60 000 atoms) in 3 s, which is consistent with the time scale for dot growth observed in other experiments as mentioned above.

No constraints were placed on the relative positions of the dots in the simulation. Therefore at long times the simulation predicts that the signal will approach a constant value (equal to $n\langle V \rangle^2$) as the spatial distribution becomes perfectly random. For the high dot density considered here, the limit of a random spatial distribution cannot be reached in reality, since the separation of the centers of two distinct QDs must always be at least one dot diameter. In the event that two dots collide, the physical result is the nucleation of a larger island having twice the QD volume, as indicated in Fig. 5.9(c). In this way the emergence of the large islands during annealing follows as a natural consequence of QD diffusion. Note that the interface between the two dots will not be coherent, owing to the deformation of each dot in response to its coherency strain with the substrate (see Fig. 1.1). Presumably a defect will form at the interface, so that dot collisions could bypass the kinetic constraint (to dislocation formation for example) ordinarily responsible for the self-limiting behavior of the QDs.

5.4.2 Island Growth and Ripening

According to the discussion in Section 5.4.1, the linear increase in the scattering signal with time in region *a* of Fig. 5.8 can be attributed to the diffusion of the QDs, some of which presumably collide to nucleate larger, dislocated islands. As discussed above the QDs continuously exchange atoms with the local adatom population. A similar process applies to the large islands, however unlike the QDs, these islands are not self-limited in size. In effect the large islands act as a sink for adatoms and therefore grow at the expense of the QDs, as illustrated in Fig. 5.9(d). The simplest applicable model for this process is that of 2D diffusion-limited growth from a surface adatom population, which has been studied theoretically by Chakraverty [77]. In general it is found that the net current J of adatoms into the island is related to the average adatom concentration n_0 by,

$$J \sim D(n_0 - n_{\text{isl}}) \quad (5.3)$$

where D is the adatom surface diffusion constant and n_{isl} is the adatom concentration at the periphery of the large island. Note that both the surface energy and the strain energy per atom are expected to be much higher for a quantum dot than for a large, strain-relaxed island. The value for n_{isl} , which is associated with the vapor pressure of an island, is therefore small compared with the equilibrium adatom density associated with a quantum dot. In this case n_0 is determined by the vapor pressure of a QD, and is approximately constant in time as the islands grow, as long as a local population of QDs remains. Therefore, the island volume is expected to increase linearly with time at

a rate proportional to the product Dn_0 , in accordance with Eq. 5.3. We further note that the nucleation rate of the large islands is expected to drop off rapidly as the islands grow and reduce the QD density, so that the density n of large islands should remain approximately constant. Therefore, according to Eq. 5.2, we expect the PSD to increase in proportion to the square of the time, which is consistent with the observed slope of 2 in region *b* of Fig. 5.8.

As is apparent in Fig. 5.6, the QD population is depleted in regions where the large island density is high, presumably because the QDs have been consumed by the large islands. In order for the islands in these regions to continue to grow they must compete with each other for material, which is Ostwald ripening [77, 78, 79]. This process is illustrated in Figs. 5.9(e) and (f). In contrast to the case just discussed, where n_0 was fixed by the vapor pressure of a QD, n_0 is now determined by the size distribution of the large islands themselves. In terms of Eq. 5.3, n_{isl} for a given island in this case is comparable to n_0 , which is not constant in time but depends on the evolving size distribution of the islands. Thus we do not expect the islands to continue to grow at a constant rate. In particular, the sign of J determines whether a particular island grows or shrinks, such that islands that are larger than a critical size grow at the expense of smaller islands. This problem has been solved self-consistently by Chakraverty [77] who finds that for the case of ripening limited by 2D surface diffusion, the average island size will increase as $(Dt)^{3/4}$. Note also that the density of islands must decrease as $1/\langle V \rangle$ to conserve material. Hence a $t^{3/4}$ dependence is expected for the PSD at long times, which

is consistent with the data in region *c* as shown in Fig. 5.8.

It is interesting that the signal in the Fig. 5.10 cannot be made to coincide with the curves in Fig. 5.8 with a simple rescaling of the time axis. In particular, the signal in Fig. 5.10 grows linearly with time until the end of growth, by which time the PSD has reached a value of $\sim 200 \text{ nm}^4$. By contrast the signals in Fig. 5.8 switch from a linear time-dependence to a t^2 dependence by the time the PSD has reached a value of only $\sim 10 \text{ nm}^4$. This implies that the emergence of the large islands was delayed in the growth in Fig. 5.10. We attribute this effect to differences in growth conditions, since the growth in Fig. 5.10 was carried out during a different MBE run and on a different substrate than the growths in Fig. 5.8. As we show below, variations in arsenic overpressure for example can have a pronounced effect on the evolution of the island distribution.

5.5 Effect of Growth Conditions on Island Growth

In the previous section it was shown that the evolution of the light scattering signal during the late stages of annealing can be explained in terms of the growth and ripening of the large island distribution. In this section we investigate further the effect of temperature, arsenic overpressure, and InAs coverage on the evolution of the large islands during annealing.

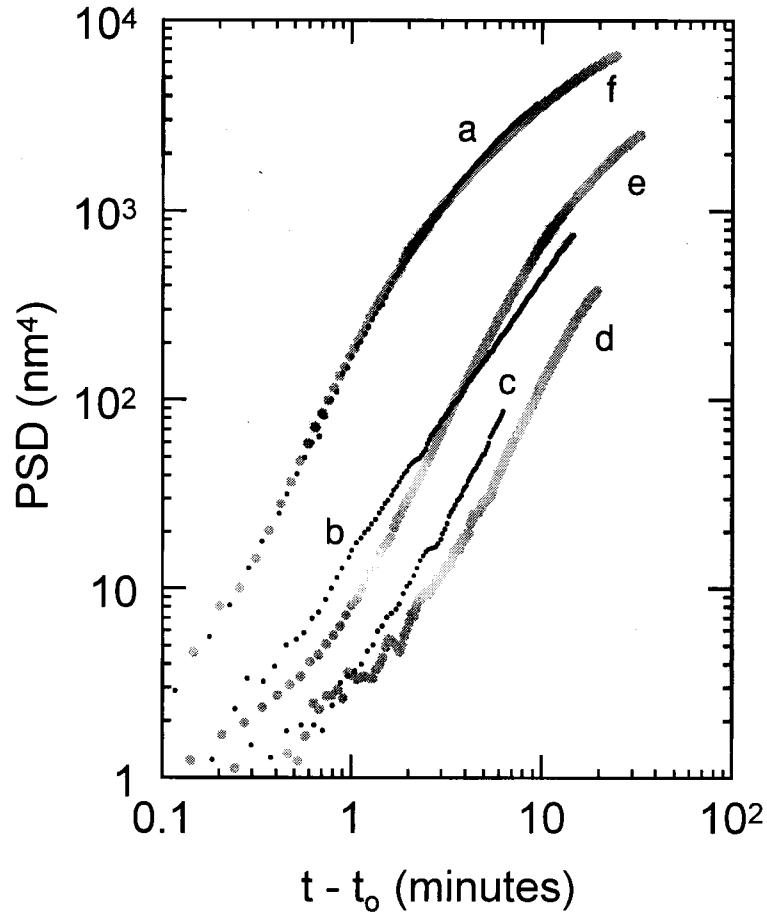


Figure 5.11: Temperature dependence of the PSD during annealing. InAs deposition begins at $t = 0$. For each curve, the annealing temperature and time, t_0 (discussed in the text), are: (a) 410°C , 1.2 min, (b) 360°C , 1.5 min, (c) 300°C , 5 min, (d) 260°C , 11 min, (e) 280°C , 1 min, and (f) 400°C , 0.2 min. Curves *e* and *f* are taken from Fig. 5.7.

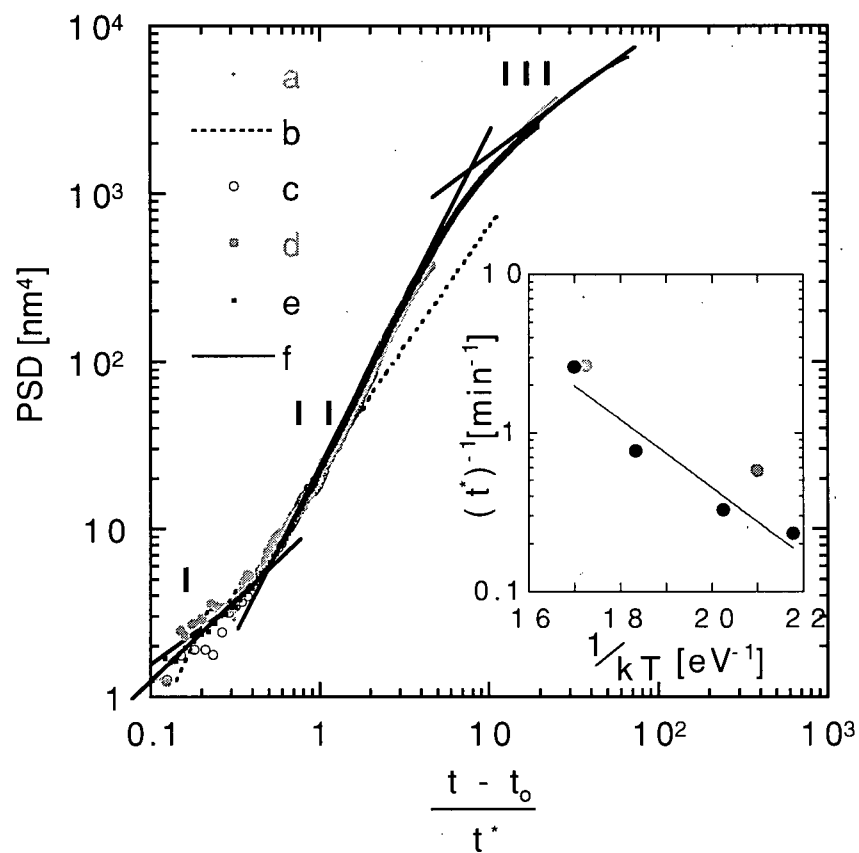


Figure 5.12: Data collapse of the six curves in Fig. 5.11, achieved by rescaling the annealing time in each case by a characteristic time t^* . Regions I, II, and III are fitted with lines of slope 1, 2, and 3/4 respectively. Inset: Temperature dependence of t^* for curves $a - d$ (black circles and solid line fit) and curves e and f (gray circles).

5.5.1 Effect of Annealing Temperature

In Figure 5.11 we display scattering measurements obtained at $41 \mu\text{m}^{-1}$ during six QD growth and annealing experiments at temperatures between 260°C and 410°C . The initial scattering from the buffer layer has been subtracted from each data set. Curves *e* and *f* correspond to the $41 \mu\text{m}^{-1}$ signals shown in Fig. 5.7. Curves *a* – *d* correspond to a series of four similar experiments performed during a second MBE run. For all the experiments conducted during both runs, the As_2 overpressure at the substrate was $\sim 5 \times 10^{-7}$ mbar, and the nominal InAs coverage was 3 ML. However in the second run (*a*–*d*) the InAs was deposited over a time period of 1.5 minutes, compared to 0.3 minutes for the first run (*e* and *f*). As in the case of Fig. 5.7 a time t_o has been subtracted from the annealing time t in each case, where t_o matches the time at which the 2D-to-3D islanding transition is observed by RHEED. For the growths corresponding to curves *c* and *d*, the observed RHEED transition was not abrupt enough to determine t_o precisely. For these curves, the values of t_o are still consistent with the RHEED measurement, however the precise value in each case was selected so that the initial slope of the data matched that of the other curves.

The discussion in Section 5.4.2 suggests that the temperature dependence of the island growth and ripening is controlled by thermally activated surface diffusion, so that the effect of a change in annealing temperature is to rescale the time axis (the island growth rate is a function of the product Dt). Accordingly in Figure 5.12 the time axis for each curve in Fig. 5.11 has been scaled by a factor t^* . With the exception of curve *b*, which has

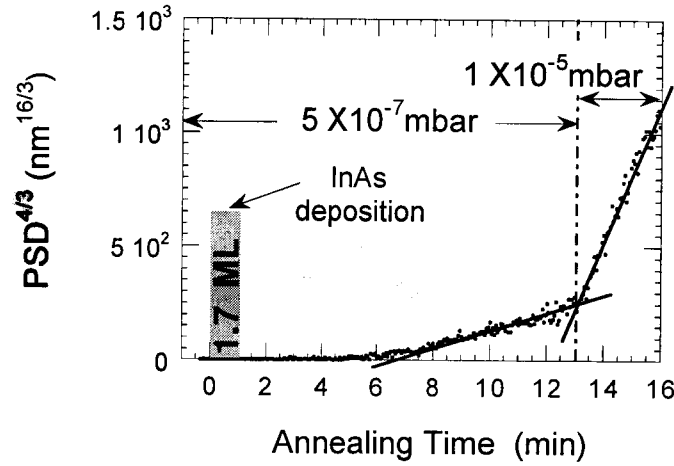


Figure 5.13: Effect of arsenic flux on island growth during annealing at 450°C. Linear fits have been made to the data before and after the switch in arsenic flux at $t = 13$ min.

an anomalous time-dependence at long times, all of the data sets collapse onto a single curve. Again we find three regions of distinct power-law behavior which we label I (slope 1), II (slope 2), and III (slope 3/4) in Fig. 5.12. In the inset of Fig. 5.12 we have plotted the temperature-dependence of t^* from the 6 data sets. The data from the MBE run corresponding to curves $a - d$ yield an activation energy for D of 0.49 ± 0.05 eV. This is close to the value of 0.6 eV, used to model In diffusion on GaAs grown by metal-organic chemical vapor deposition (MOCVD) [62].

5.5.2 Effect of Arsenic Pressure and Indium Coverage

In Figure 5.13 we examine the effect of a change in arsenic overpressure during annealing. Here, and in Fig. 5.5.2, we plot $\text{PSD}^{4/3}$ against time, so that a constant slope is obtained while ripening is occurring. For this experiment, conducted at a substrate temperature of

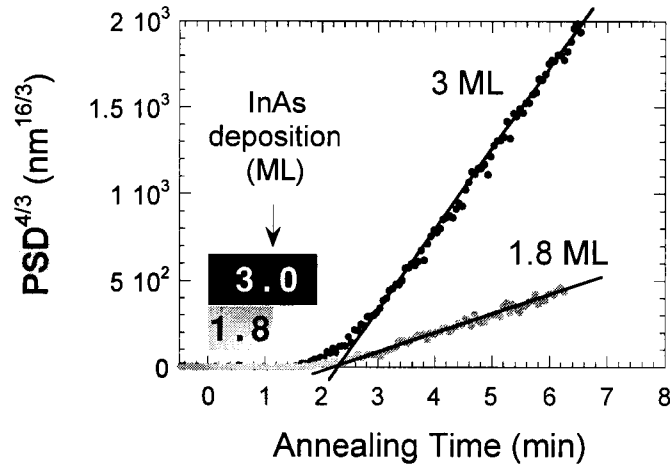


Figure 5.14: Effect of indium coverage on island growth during annealing at 450 °C.

450 °C, 1.7 ML of InAs were deposited during the first minute as indicated by the shaded bar in Fig. 5.13. At $t = 13$ min, the As_2 overpressure was increased from 5×10^{-7} mbar to 1×10^{-5} mbar, resulting in an increase in the slope in Fig. 5.13 which we interpret as evidence of an increase in the rate of ripening. A possible explanation is that indium diffusion becomes more isotropic with increasing arsenic flux, enhancing the overall 2D surface diffusion, as has been proposed for Ga diffusion on GaAs [80]. If the increased ripening rate is due only to increased surface diffusion, Fig. 5.13 implies that the 2D diffusion increases by a factor of 8.5 (the ratio of the slopes [78]) due to the factor of 20 increase in As_2 overpressure.

The effect of a change in the amount of InAs deposited is shown in Figure 5.5.2. The data were acquired during two experiments in the same MBE run, using the evaporation procedure between experiments described above. In the first experiment, 3 ML of InAs

were deposited in 2 min, compared to 1.8 ML in 1.2 min in the second experiment. The temperature (450 °C) and As₂ overpressure (5×10^{-7} mbar) were nominally the same for both runs. The time-intercept of each straight-line fit in Fig. 5.5.2 occurs at $t = 2.2$ min, which we associate with the onset of ripening. Although ripening begins at the same time for both experiments, the slope of the linear fit is larger by a factor of 4 for the higher InAs coverage. These results are consistent with an increase in QD density with increasing InAs coverage, as has been reported by others [81]. One would also expect a higher density of defect-containing islands, and hence an increase in the scattering signal according to Eq. 5.2, consistent with the experimental data.

5.5.3 Effect of Surface Strain Fields

In Chapter 4 it was shown that surface strain fields can affect the diffusion of adatoms on the surface. In order to investigate the effect of strain field gradients on diffusion during quantum dot growth, we performed experiments in which quantum dots were grown on a strain-relaxed InGaAs layer.

AFM images of the resulting island distributions are shown in Figure 5.15, for the case of (a) InAs dots and (b) InP dots, both grown on strain-relaxed In_xGa_{1-x}As layers having a nominal composition of $x = 0.2$. The InGaAs layer in both cases was grown at 500 °C. For the film in Fig. 5.15(a), nominally 6 ML of InAs were deposited over a 4 minute interval at 450 °C, on a 170 nm thick InGaAs film. For the film in Fig. 5.15(b), a 10 nm thick GaAs film was grown on top of a 250 nm thick InGaAs film, and 4 ML of InP were

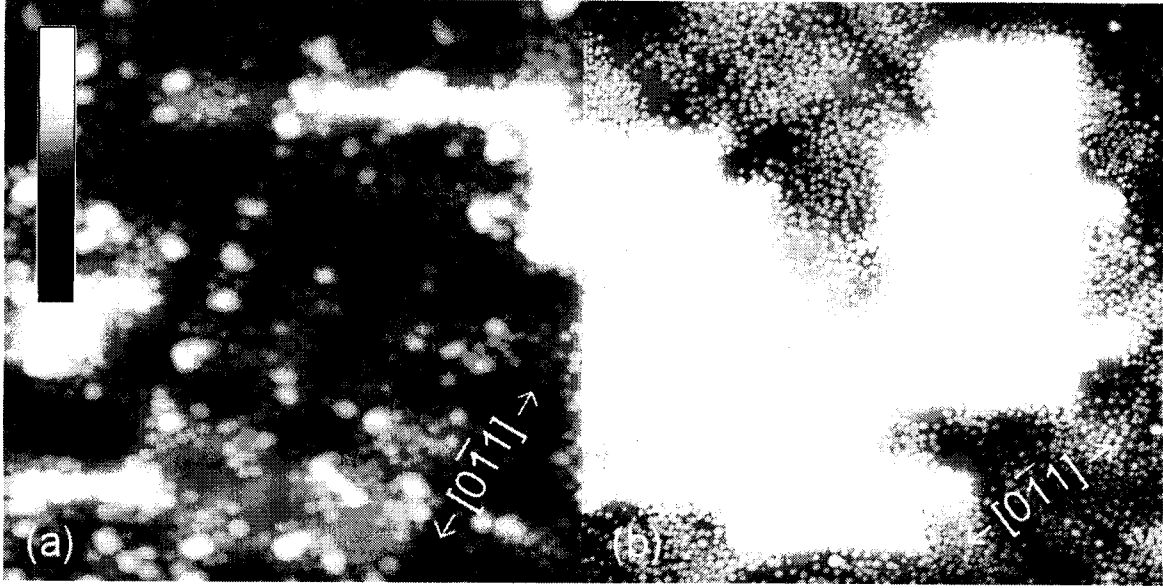


Figure 5.15: AFM images of dots grown on strain-relaxed InGaAs films. (a) 6 ML of InAs deposited on a 170 nm thick InGaAs film ($2.5 \times 2.5 \mu\text{m}^2$). (b) 4 ML of InP grown on a 250 nm thick InGaAs layer ($4 \times 4 \mu\text{m}^2$). The gray scale bar corresponds to 150 nm and 50 nm for (a) and (b) respectively.

deposited at 500°C in 0.3 minutes. In both cases the film was annealed for 1 minute before shutting off the power to the substrate heater. Although X-ray measurements were not performed on these films, the InGaAs films are expected to be more than 50% relaxed, based on measurements performed on similar films.

The images reveal that the presence of the relaxed InGaAs layer has had a pronounced effect on the spatial distributions of the islands. In particular the dot concentration is spatially modulated along the $\langle 110 \rangle$ directions. Consistent with the model in Chapter 4, we expect that the dislocation strain fields will induce spatial variations in the effective growth rates of the strained InAs or InP material across the film. Thus the dots will

nucleate first in those regions where the strain is lowest. Once the dots nucleate, nearby material is consumed so that no new dots can nucleate in adjacent regions. For the InAs growth [Fig 5.15(a)], many large islands are visible in the image, in contrast to the film shown in Fig 5.5(a) of an InAs film grown at the same temperature. This is attributed to the higher density of dots in the present case, resulting both from the higher InAs coverage (6 ML as compared to 3 ML), and the effect of the dislocation strain fields which concentrate the dots into the strain-relieved regions of the film.

5.6 Summary

In conclusion we have shown that ultraviolet light scattering can detect the onset of quantum dot formation in real time, in the InAs/GaAs system. The *in situ* light scattering results are found to be in good agreement with the island size distributions determined from AFM, taking into account the finite radius of the probe tip. We explain the time evolution of the scattering signal during annealing in terms of a three-stage process in which (1) the quantum dots nucleate and diffuse on the substrate, (2) large islands nucleate and consume the quantum dots, and (3) the large islands ripen in a manner consistent with 2D diffusion-limited Ostwald ripening. For growths performed under nominally identical conditions during the same MBE run, the temperature-dependence of these processes is found to be accounted for by a simple rescaling of the time axis. Consistent with these results, it is proposed that the island growth and ripening are limited by surface diffusion, for which we find an activation energy of ~ 0.5 eV. The ripening of the islands occurs

more rapidly with increasing As_2 overpressure, which we attribute to an enhancement of the 2D diffusion of In on GaAs as the arsenic flux is increased.

A mechanism for the nucleation of the large islands is proposed, in which a collision between two diffusing dots produces a defect-containing island. This mechanism bypasses the kinetic barrier that is believed to ordinarily constrain the size of the dots. We note that the conclusion that the dots diffuse during annealing has important implications for quantum dot device fabrication. For example this suggests that the dots should be capped quickly after they form, in order to achieve a high-density, uniformly-spaced array of QDs without defective islands, as required for QD lasers.

For InAs and InP dots grown on strain-relaxed InGaAs films, the dot concentration is found to be strongly modulated along the $\langle 110 \rangle$ directions. This provides additional evidence for the main conclusion of Chapter 4, that the strain fields resulting from misfit dislocations at the film/substrate interface can have a pronounced effect on the diffusion of adatoms at the surface.

Chapter 6

Conclusions

This work demonstrates that light scattering is a quantitative probe of thin film surface morphology that is readily applied to the study of epitaxial crystal growth. Light scattering measurements of the surface power spectral density are compared with AFM data, for a variety of MBE-grown samples exhibiting different kinds of roughness. We find that AFM and light scattering generally agree within a factor of 2, over the 1 to 10 μm^{-1} spatial frequency range. An ultraviolet light scattering apparatus is described, which extends the spatial frequency range of the light scattering technique to 41 μm^{-1} . It is shown that UV light scattering can detect the formation of InAs/GaAs quantum dots in real time during growth. Quantitative agreement between light scattering and AFM is obtained for measurements performed on these small, high aspect ratio structures, once the finite radius of the AFM probe tip is accounted for.

The ultraviolet light scattering technique is used to monitor the time-evolution of the quantum dot distribution during annealing. Combined with AFM measurements on quenched films taken after different annealing times, analysis of the real-time light

scattering data provides a detailed picture of the island growth process, which would be difficult or impossible to obtain from *ex situ* measurements alone. In particular we show that several quantum dot growth experiments can be performed on the same GaAs substrate in a single MBE run, so that the effect of changes in growth conditions can be studied much more quickly and controllably than would be possible in experiments performed during sequential runs on different substrates. The analysis reveals that the dot distribution evolves according to a three-stage process during annealing. A key feature of this process is the emergence of large defective islands, which grow first by consuming material from the quantum dots and then through diffusion-limited Ostwald ripening. The initial increase in the light scattering signal, before the large islands appear, is attributed to diffusion of the quantum dots on the substrate. It is proposed that the large islands nucleate as a result of collisions between the randomly diffusing dots.

A one-dimensional continuum growth model is developed to explain the emergence of the surface crosshatch pattern during growth of strain-relaxed $\text{In}_x\text{Ga}_{1-x}\text{As}$ on GaAs. A strain-field driving term is included, which accounts for the surface diffusion of adatoms in response to strain-related gradients in the chemical potential. These gradients arise from the introduction of interfacial misfit dislocations as the film relaxes. An analytical solution to the growth equation is obtained, which reproduces both the time dependence and the spatial frequency dependence of the surface morphology, as measured by AFM and light scattering. According to the model, the dynamics of the roughening is controlled both by the relaxation rate of the film and the surface diffusion of the adatoms. In cases

where the film relaxation rate is known independently (from X-ray measurements for example), the only remaining parameter to fit the observed dynamics is the constant ν that controls the rate at which surface slopes are reduced by surface diffusion. Based on model fits to *in situ* light scattering data obtained along both $\langle 110 \rangle$ directions during growth, we find that ν is an order of magnitude higher along the $[1\bar{1}0]$ direction compared to the $[110]$ direction. This anisotropy in ν is consistent with the anisotropy observed in the roughness of GaAs buffer layers.

In conclusion, the results presented here demonstrate that by examining the surface morphology of a growing film, detailed information about the physical processes occurring within the film and at the surface can be obtained. Here we have focused on two specific examples of surface roughening, associated with two different strain relaxation mechanisms, however the techniques used in this work are applicable to any growth process in which surface roughness develops and in which optical access to the sample is available to measure this roughness.

Bibliography

- [1] J.A. Dura, J.G. Pellegrino and C.A. Richter, Appl. Phys. Lett. **69**, 1134 (1996).
- [2] D.K. Fork, F. Armani-Leplingard, M. Lui and R.A. McFarlane, J. Lightwave Technology **14**, 611 (1996).
- [3] T. Mishima, M. Kudo, J. Kasai, K. Higuchi and T. Nakamura, J. Cryst. Growth **200/201**, 271 (1999).
- [4] A.-L. Barabási and H.E. Stanley, *Fractal Concepts in Surface Growth* (Cambridge University Press, Cambridge, 1995).
- [5] J. Villain, J. Phys. (France) I **1**, 19 (1991)
- [6] F. Family, Physica A **168A**, 561 (1990).
- [7] L. Vazquez, R.C. Salvarezza, P. Herrasti, P. Ocon, J.M. Vara and A.J. Arvia, Phys. Rev. B **52**, 2032 (1995).
- [8] Chung-Yu Mou and J.W.P. Hsu, Phys. Rev. B **53**, 7610 (1996).
- [9] B.J. Spencer, S.H. Davies and P.W. Voorhees, Phys. Rev. B. **47**, 9760 (1993).
- [10] F. Jonsdottir, L.B. Freund, Mech. Mat. **20**, 337 (1995).

- [11] J. Drucker, *Phys. Rev. B* **48**, 18203 (1993).
- [12] E.A. Fitzgerald, Y.-H. Xie, D. Monroe, P.J. Silverman, J.M. Kuo, A.R. Kortan, F.A. Thiel and B.E. Weir, *J. Vac. Sci. Technol. B* **10**, 1807 (1992).
- [13] M.A. Lutz, R.M. Feenstra, F.K. LeGoues, P.M. Mooney and J.O. Chu, *Appl. Phys. Lett.* **66**, 724 (1995).
- [14] A.G. Cullis, A.J. Pidduck and M.T. Emeny, *J. Cryst. Growth* **158**, 15 (1996).
- [15] A.R. Boyd, T.B. Joyce and R. Beanland, *J. Cryst. Growth* **164**, 51 (1996).
- [16] D.E. Jesson, K.M. Chen, S.J. Pennycook, T. Thundat and R.J. Warmack, *Phys. Rev. Lett.* **77**, 1330 (1996).
- [17] M. Albrecht, S. Christiansen, J. Michler, H.P. Strunk, P.O. Hansson and E. Bauser, *J. Cryst. Growth* **167**, 24 (1996).
- [18] F.M. Ross, J. Tersoff, and R.M. Tromp, *Phys. Rev. Lett.* **80**, 984 (1998).
- [19] J.A. Floro, G.A. Lucadamo, E. Chason, L.B. Freund, M. Sinclair, R.D. Twisten, and R.Q. Hwang, *Phys. Rev. Lett.* **80**, 4717 (1998); E. Chason, M.B. Sinclair, J.A. Floro, J.A. Hunter, and R.Q. Hwang, *Appl. Phys. Lett.* **72**, 3276 (1998).
- [20] R. Leon, C. Lobo, J. Zou, T. Romeo, and D.J.H. Cockayne, *Phys. Rev. Lett.* **81**, 2486 (1998).
- [21] D. Leonard, K. Pond and P.M. Petroff, *Phys. Rev. B* **50**, 11687 (1994).

- [22] S. Fafard, Z.R. Wasilewski, C. Ni Allen, D. Picard, M. Spanner, J.P. McCaffrey and P.G. Piva, Phys. Rev. B **59**, 15368 (1999).
- [23] M.T. Sinn, J.A. del Alamo, B.R. Bennett, K. Haberman and F.G. Celii, J. Electron. Mater. **25**, 313 (1996).
- [24] J.C. Stöver, *Optical Scattering* (SPIE, Bellingham, 1995).
- [25] E.L. Church, H.A. Jenkinson and J.M. Zavada, Opt. Eng. **16**, 360 (1977).
- [26] C. Lavoie, T. Pinnington, E. Nodwell, T. Tiedje, R.S. Goldman, K.L. Kavanagh and J.L. Hutter, Appl. Phys. Lett. **67**, 3744 (1995).
- [27] D.L. Huffaker, G. Park, Z. Zou, O.B. Shchekin and D.G. Deppe, Appl. Phys. Lett. **73**, 2564 (1998).
- [28] K.L. Westra and D.J. Thomson, J. Vac. Sci. Technol. B **13**, 344 (1995).
- [29] J. Aué and J. Th. M. De Hosson, Appl. Phys. Lett. **71**, 1347 (1997).
- [30] C. Lavoie, T. Pinnington, T. Tiedje, J.L. Hutter, G. Soerensen and R. Streater, Can. J. Phys. (Suppl.) **74**, S49 (1996).
- [31] T. Pinnington, C. Lavoie, T. Tiedje, B. Haveman, and E. Nodwell, Phys. Rev. Lett. **79**, 1698 (1997).
- [32] P.R. Spyak and W.L. Wolfe, Opt. Eng. **31**, 1746 (1992).
- [33] S. R. Johnson, Ph.D. Thesis, University of British Columbia, 1996.

- [34] C. Lavoie, Ph.D. Thesis, University of British Columbia, 1994.
- [35] E.H.C. Parker, *The Technology and Physics of Molecular Beam Epitaxy* (Plenum Press, New York, 1985).
- [36] S.R. Johnson, C. Lavoie, T. Tiedje and J.A. MacKenzie, J. Vac. Sci. Technol. B **11**, 1007 (1993).
- [37] T. van Buuren, M.K. Weilmeier, I. Athwal, K.M. Colbow, J.A. Mackenzie, T. Tiedje, P.C. Wong and K.A.R. Mitchell, Appl. Phys. Lett. **59**, 464 (1991).
- [38] M.K. Nissen, C. Lavoie, S. Eisebitt, T. Pinnington, and T. Tiedje, Scanning Microscopy **8**, 935 (1994).
- [39] J.W. Goodman, *Statistical Optics* (John Wiley and Sons, New York, 1985).
- [40] The image processing package used was GCP Works, which was made available by Dr. Woodham at the Department of Computer Science, University of British Columbia.
- [41] H.-C. Ko, D.-C. Park, Y. Kawakami, Shizuo Fujita and Shigeo Fujita, Appl. Phys. Lett. **70**, 3278 (1997).
- [42] H. Lee, R. Lowe-Webb, W. Yang and P.C. Sercel, Appl. Phys. Lett. **72**, 812 (1998).
- [43] H. Saito, K. Nishi and S. Sugou, Appl. Phys. Lett. **74**, 1224 (1999).
- [44] Experimental evidence that k is constant for QD distributions in the InAs/GaAs system is presented in: Y. Ebiko, S. Muto, D. Suzuki, S. Itoh, K. Shiramine, T.

- Haga, Y. Nakata, and N. Yokoyama, *Phys. Rev. Lett.* **80**, 2650 (1998).
- [45] T. Pinnington, C. Lavoie and T. Tiedje, *J. Vac. Sci. Technol. B* **15**, 1265 (1997).
- [46] E.D. Palik, *Handbook of Optical Constants of Solids* (Academic Press, San Diego, 1985).
- [47] Oriel Catalog, 1999.
- [48] A. Wankerl, A.T. Schremer, and J.R. Shealy, *Appl. Phys. Lett.* **72**, 3332 (1998).
- [49] L.D. Landau and E.M. Lifshitz, *Theory of Elasticity* (Addison-Wesley, Reading, Massachusetts, 1970).
- [50] J.Y. Tsao, *Materials Fundamentals of Molecular Beam Epitaxy* (Academic, Boston, 1993).
- [51] J.W. Matthews, S. Mader and T.B. Light, *J. Appl. Phys.* **41**, 3800 (1970).
- [52] J.W. Matthews and A.E. Blakeslee, *J. Cryst. Growth* **27**, 118 (1974).
- [53] R. Beanland and A.R. Boyd in *Microscopy of Semiconducting Materials* 1995, edited by A.G. Cullis and A.E. Staton-Bevan, *Inst. Phys. Conf. Series No. 146* (IOP, Bristol, 1995), p. 153.
- [54] P. Moeck, B.K. Tanner, C.R. Whitehouse et al., in *Proceedings of the 23rd International Conference on Phys. Semiconductors*, edited by M. Scheffler and R. Zimmerman (World Scientific, Singapore, 1996), Vol. 2, p. 927.
- [55] R. Beanland, *J. Appl. Phys.* **72**, 4031 (1992).

- [56] K.L. Kavanagh, R.S. Goldman, C. Lavoie, B. Leduc, T. Pinnington, T. Tiedje, D. Klug and J. Tse, *J. Crystal Growth* **174**, 550 (1997).
- [57] R.I. Cottam and G.A. Saunders, *J. Phys. C* **6**, 2105 (1973).
- [58] S. Adachi, *Physical Properties of III-V Semiconductor Compounds* (John Wiley and Sons, New York, 1992).
- [59] A.W. Adamson, *Physical Chemistry of Surfaces* (John Wiley and Sons, New York, 1982).
- [60] Park Scientific Instruments Scanning Force Microscope, with closed-loop probe positioning. This measurement was performed by George Soerensen.
- [61] M. Kasu and N. Kobayashi, *J. Appl. Phys.* **78**, 3026 (1995).
- [62] R.E. Welser and L.J. Guido, *Appl. Phys. Lett.* **68**, 912 (1996).
- [63] J. Tersoff, M.D. Johnson and B.G. Orr, *Phys. Rev. Lett.* **78**, 282 (1997).
- [64] R.S. Goldman, H.H. Wieder, K.L. Kavanagh, K. Rammohan and D.H. Rich, *Appl. Phys. Lett.* **65**, 1424 (1994).
- [65] M. Adamcyk, T. Pinnington, A. Ballestad and T. Tiedje, *Proc. Chinese Mat. Res. Soc.* (1999).
- [66] C. Orme, M.D. Johnson, J.L. Sudijono, K.-T. Leung and B.G. Orr, *Appl. Phys. Lett.* **64**, 860 (1994).

- [67] G. Medeiros-Ribeiro, A.M. Bratkovski, T.I. Kamins, D.A.A. Ohlberg and R.S. Williams, *Science* **279**, 353 (1998).
- [68] G. Springholz, V. Holy, M. Pinczoltz and G. Bauer, *Science* **282**, 734 (1998).
- [69] C. Weisbuch and B. Vinter, *Quantum Semiconductor Structures* (Academic, San Diego, 1991).
- [70] S. Fafard, Z.R. Wasilewski, C. N. Allen, D. Picard, P.G. Piva, and J.P. McCaffrey, *Superlattices and Microstructures* **25**, 87 (1999).
- [71] I. Mukhametzhanov, R. Heitz, J. Zheng, P. Chen, and A. Madhukar, *Appl. Phys. Lett.* **73**, 1841 (1998).
- [72] T. Pinnington, Y. Levy, J.A. MacKenzie, and T. Tiedje, *Phys. Rev. B* **60**, 15901 (1999).
- [73] N. Moll, M. Scheffler and E. Pehlke, *Phys. Rev. B* **58**, 4566 (1998).
- [74] R. Heitz, T.R. Ramachandran, A. Kalburge, Q. Xie, I. Mukhametzhanov, P. Chen, and A. Madhukar, *Phys. Rev. Lett.* **78**, 4071 (1997).
- [75] V.A. Shchukin, N.N. Ledenstov, P.S. Kop'ev and D. Bimberg, *Phys. Rev. Lett.* **75**, 2968 (1995).
- [76] W.W. Pai, A.K. Swan, Z. Zhang and J.F. Wendelken, *Phys. Rev. Lett.* **79**, 3210 (1997).
- [77] B.K. Chakraverty, *J. Phys. Chem. Solids* **28**, 2401 (1967).

- [78] M. Zinke-Allmang, L.C. Feldman, and S. Nakahara, Appl. Phys. Lett. **51**, 975 (1987).
- [79] B.D. Min, Y. Kim, E.K. Kim, S-K Min, and M.J. Park, Phys. Rev. B **57**, 11879 (1998).
- [80] H. Yang, V.P. LaBella, D.W. Bullock, and P.M. Thibado, J. Vac. Sci. Tech. B (to be published).
- [81] T.R. Ramachandran, R. Heitz, P. Chen, and A. Madhukar, Appl. Phys. Lett. **70**, 640 (1997).

Appendix A

The Polarization Factor

The polarization factor Q which appears in Eqs. 2.5 and 2.8 is discussed in Stover [24] and Church [25]. Here we present the expressions used to calculate each of the four components $Q_{\alpha\beta}$ of Q , where α is the polarization of the source, and β is the polarization to which the receiver is sensitive. The two orthogonal components of the polarization are denoted s and p , where s describes the case where the electric field vector of the transverse electromagnetic wave is parallel to the plane of the surface, and p the case where the electric field vector is parallel to the plane of incidence. For scattering from a reflecting material of complex dielectric constant ϵ , the components of Q may be written [25]:

$$Q_{ss} = \left| \frac{(\epsilon - 1) \cos \phi_s}{(\cos \theta_i + \sqrt{\epsilon - \sin^2 \theta_i})(\cos \theta_s + \sqrt{\epsilon - \sin^2 \theta_s})} \right|^2 \quad (\text{A.1})$$

$$Q_{sp} = \left| \frac{(\epsilon - 1) \sqrt{\epsilon - \sin^2 \theta_s} \sin \phi_s}{(\cos \theta_i + \sqrt{\epsilon - \sin^2 \theta_i})(\epsilon \cos \theta_s + \sqrt{\epsilon - \sin^2 \theta_s})} \right|^2 \quad (\text{A.2})$$

$$Q_{ps} = \left| \frac{(\epsilon - 1) \sqrt{\epsilon - \sin^2 \theta_s} \sin \phi_s}{(\epsilon \cos \theta_i + \sqrt{\epsilon - \sin^2 \theta_i})(\cos \theta_s + \sqrt{\epsilon - \sin^2 \theta_s})} \right|^2 \quad (\text{A.3})$$

$$Q_{pp} = \left| \frac{(\epsilon - 1)(\sqrt{\epsilon - \sin^2 \theta_s} \sqrt{\epsilon - \sin^2 \theta_i} \cos \phi_s - \epsilon \sin \theta_i \sin \theta_s)}{(\epsilon \cos \theta_i + \sqrt{\epsilon - \sin^2 \theta_i})(\epsilon \cos \theta_s + \sqrt{\epsilon - \sin^2 \theta_s})} \right|^2 \quad (\text{A.4})$$

where the angles θ_i , θ_s , and ϕ_s are as shown in Figure 2.3.

For the *ex situ* measurements presented in Chapter 2, *s*-polarized 632-nm light is incident on the sample at $\theta_i = 65^\circ$ and is detected in the plane of incidence. In this case $Q = Q_{ss}$, and $\epsilon = 14.83 + 1.512i$ for GaAs [46]. The dependence of Q_{ss} on scattering angle for this configuration is plotted in Figure A.1 (dotted curve). For reference we also indicate the angular range (θ_s between 62° and -46°) used in the *ex situ* measurements to access spatial frequencies between 0.2 and $16 \mu\text{m}^{-1}$. Over this range Q is approximately 0.5, and varies by only 32%.

For the *in situ* ultraviolet light scattering measurements described in Chapter 5, unpolarized 250-nm light is incident at $\theta_i = 55^\circ$. In this case,

$$Q = \frac{1}{2}(Q_{ss} + Q_{pp} + Q_{sp} + Q_{ps}). \quad (\text{A.5})$$

We plot Q_{ss} and Q_{pp} for the case of detection in the plane of incidence (so that the cross-polarization terms are zero), in Fig. A.1 (solid curves). For this wavelength in GaAs, $\epsilon = -8.05 + 23.4i$ [46]. The relevant components of $Q_{\alpha\beta}$ for the two detection angles corresponding to the two *in situ* signals, are compared in Table A.1. Note that for these backscattering angles, the signal intensity is dominated by the *p*-polarized component of the incident light.

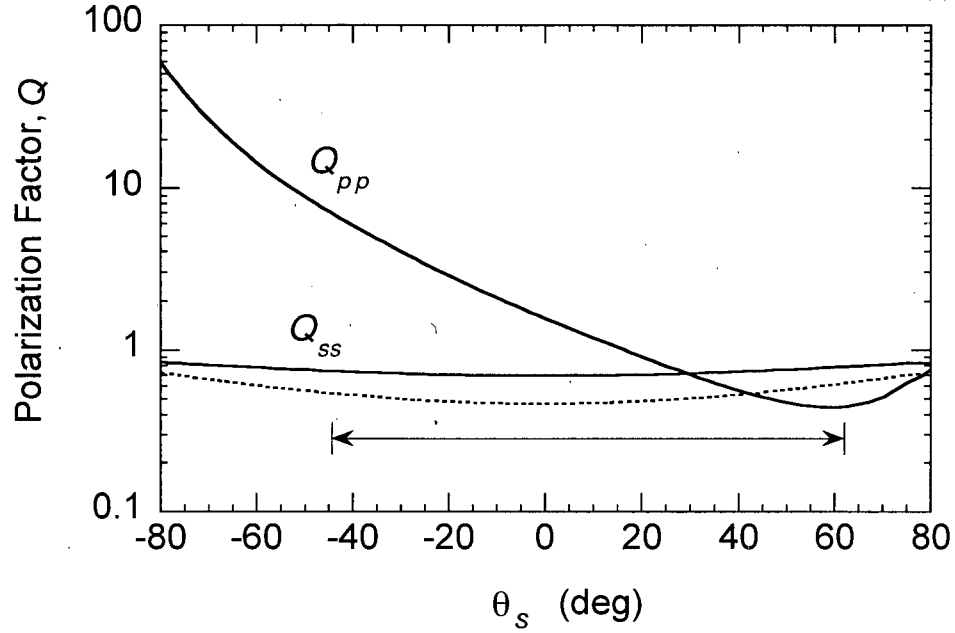


Figure A.1: Polarization factor Q corresponding to two different scattering set-ups, for which $\phi_s = 0$. Dotted curve: Q_{ss} for the case of 632-nm light incident at $\theta_i = 65^\circ$. Solid curves: Q_{ss} and Q_{pp} for 250-nm light incident at 55° . The arrow indicates the angular range used in the *ex situ* light scattering measurement.

$q(\mu\text{m}^{-1})$	$\theta_s(^{\circ})$	$\phi_s(^{\circ})$	Q_{ss}	Q_{pp}	Q_{sp}	Q_{ps}	Q
31	-25	0	0.713	3.39	0	0	2.06
41	-55	22.5	0.688	13.27	0.275	0.346	7.29

Table A.1: Components of Q for unpolarized 250-nm light incident at $\theta_i = 55^\circ$, for the two spatial frequencies, q , accessible in the *in situ* measurement.